12-2019

Oxidative and Adsorbent Impacts on Selenide Based Transition Metal Dichalcogenides

Anna Hoffman
University of Tennessee, ahoffm12@vols.utk.edu

To the Graduate Council:

I am submitting herewith a dissertation written by Anna Hoffman entitled "Oxidative and Adsorbent Impacts on Selenide Based Transition Metal Dichalcogenides." I have examined the final electronic copy of this dissertation for form and content and recommend that it be accepted in partial fulfillment of the requirements for the degree of Doctor of Philosophy, with a major in Materials Science and Engineering.

Philip D. Rack Dr, Major Professor

We have read this dissertation and recommend its acceptance:

Jason D. Fowlkes Dr., David G. Mandrus Dr., Gong Gu Dr.

Accepted for the Council:

Dixie L. Thompson

Vice Provost and Dean of the Graduate School

(Original signatures are on file with official student records.)

Oxidative and Adsorbant impacts on Selenide based Transition Metal Dichalcogenides

A Dissertation Presented for the

Doctor of Philosophy

Degree

The University of Tennessee, Knoxville

Anna N. Hoffman

December 2019

Acknowledgments

I would like to thank my advisor Dr. Philip Rack, my group members past and present. My ever supportive family and friends who have potentially jinxed the whole thing by calling me 'Dr' for the past 4 years. All my collaborators at UT, CNMS, ORNL, Y12, and UVA. My committee members who helped guide my progress. The Special Events Department of the City of Knoxville who provided a creative outlet during my time in graduate school. And my pets, for constantly reminding me nothing is more important than keeping yourself fed and well rested.

Abstract

This paper covers an overview of the transition metal dichalcogenides, TMD, class of materials. Their layered van der Waals chemical structure and unique electrical and optical properties, such as an indirect in the bulk to direct band gap in the monolayer transition, has brought research focus to their potential role in nanoelectronics. This paper goes over general TMD properties then focuses on WSe_2. While TMDs posses useful and promising characteristics in their pristine state, without precise control over electrical behavior real world application will never occur. Defect engineering is discussed as a method to tune TMD properties, specifically the effects of O_2 plasma exposure which oxidized the top most layer of TMD selenides and p-dopes the underlying pristine material.

Table of Contents

List of Figures

List of Tables

Chapter 1

Background

1.1 Transition Metal Dichacogenides

The discovery of atomically thin graphene in 2004 by Novoselov et. all started the 2D materials revolution. Before this advancement, it was not known atomically single and few-layer thick van der Waals (vdW) materials could be produced, processed, and utilized [1] [2]. While graphene does not have a bandgap [1], thus limiting its usefulness in electronic devices, research into other van der Waals materials, such as boron nitride, oxides, hydroxides, oxychlorides, and transition metal dichalcogenides (TMDs) began quickly and extensively [3]. Some of these materials are not electronically useful semiconductors for transistor applications, because their bandgaps are too small and thus at or near room temperature valence band electrons can be thermally excited to the conduction band. Thus TMDs, which have band gaps greater than 1eV, became a main focus of 2D research [3].

1.1.1 Chemical Structure

Initial research reported charge carrier mobilities in TMDs to be quite low [4] and interest dropped, but in 2011 top gated MoS_2 transistors displayed highly favorable mobilities approaching 60-70 cm2/Vs mobility, with a 10^8 on/off ratio, and 74mV/dec subthreshold swing [5]. Many TMDs have a MX_2 chemical makeup, where M is a transition metal element, often Molybdenum and Tungsten, and the X is a chalcogen atom from group 16 on the periodic table, often Sulfur, Selenium, or Tellurium. A single layer consists of three ordered planes arranged as X-M-X [6] [3]. The thickness of a TMD monolayer depends on the specific atoms in the compound but range from 0.6-0.9 nm [7]. The oxidation state of the transition metal is typically +4 and for the chalcogen -2 [8] resulting in an overall neutral MX_2 monolayer. Intralayer bonding is strong covalent in two polytype crystal structures illustrated in Figure 1.1, the most common, trigonal prismatic or 2H, and octahedral 1T [9]. When imaged with a scanning transmission electron mictroscope (STEM) like in Figure 1.2 here is a strong contrast difference between the two coordinations due to the direct stacking of chacogenides in 2H which leaves empty the hexagonal centers while the chacogenide layers in 1T coordination does not have empty sites. Only weak van der Waals forces keep layers bound together [8], thus preparation of single layers is relatively easy via exfoliation.

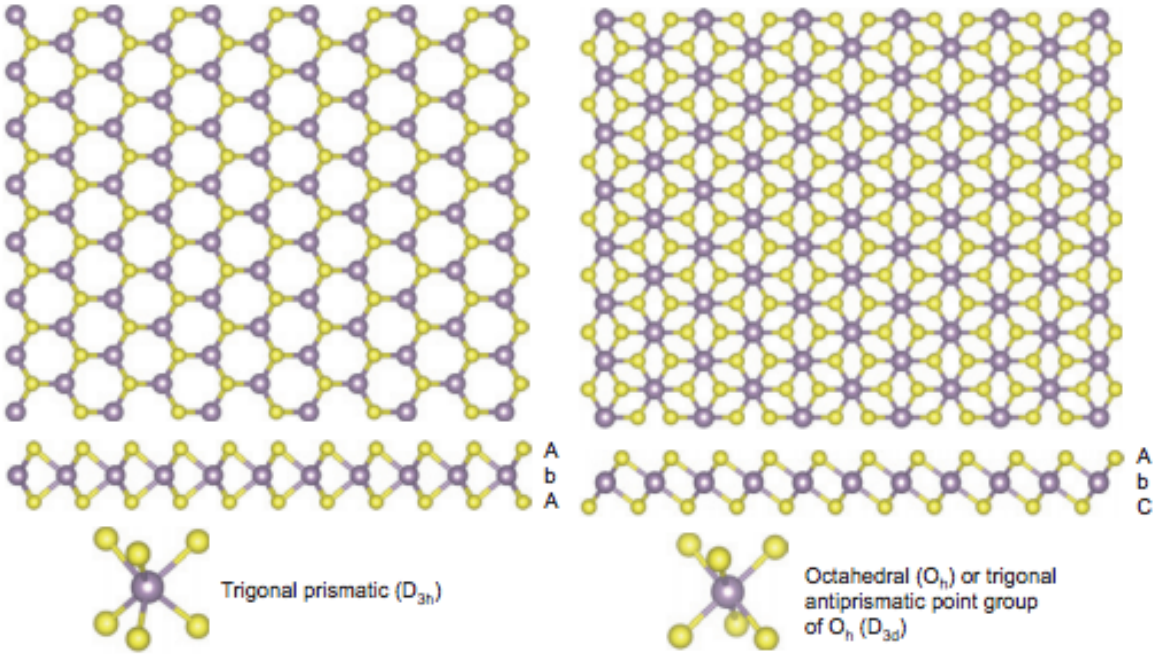

(a) 2H - Trigonal Prismatic coordination **(b)** 1T - Octahedral coordination

Figure 1.1: Chemical structures of TMD layers from source [10].

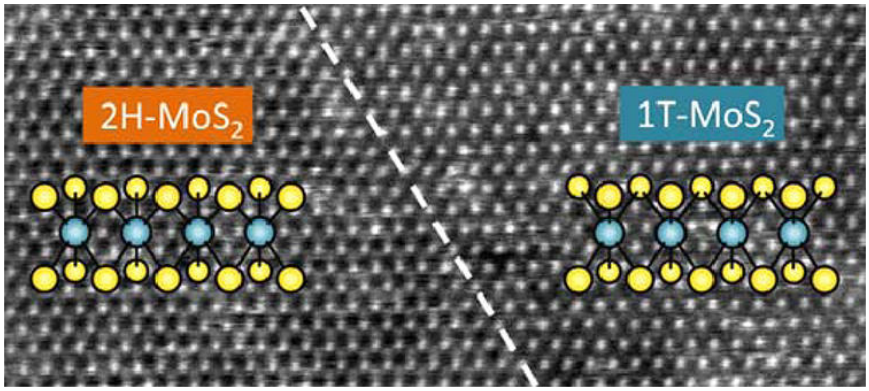

Figure 1.2: STEM image of each coordination from source [11]

Due to the TMD chemical structure, each monolayer has an atomically pristine surface free of dangling bonds and interface traps [12] which is can be a significant issue for silicon and other semiconductor based devices [13]. Clean and neutral surfaces on monolayer TMDs allow for easy vertical scaling in advanced device fabrication and straightforward electrostatics [12].

1.1.2 Layer Thickness Dependence

Structurally, each layer is identical, but there are significant changes in electrical and optical behavior as these layers stack due to changes in symmetry and quantum confinement [3] [12] [14] [15]. There are multiple ways to determine number of layers in a sample, optical identification has been proven reliable by contrast to the substrate [16] evident in Figure 1.3 taken by the author, atomic force microscopy to determine exact height [17], and Raman spectroscopy which will be discussed later [15]. Charge carrier mobility, an important characteristic of electronic devices, is a thickness dependent property [3] [18] [19]. Mobility decreases as thickness decreases [18] [19] [20] [6] [21] and the experimental reduction of mobility at the single layer is even higher than theoretically predicted. The theoretical mobility of single layer MoS_2 at room temperature is about 300 to 400 cm^2/Vs which is 5x higher than what is achieved experimentally [18]. In few layer samples, charge carriers have access to movement in 3 dimensions and the adverse effect of charged impurities present at the top and bottom interfaces is damped [3]. These ideas have been supported by experimental results, where the highest mobility to date has occurred in few layer samples [12] [3]. Charge mobility sensitivity to thin film interfaces has presented a challenge to achieve high electrical sensitivity, flicker noise caused by random surface impurities from the environment can dominate subtle electrical behavior in devices. Research has shown capping layers can reduce this noise, characterized by the Hooge parameter [22]. Capping is also a way to control electrical behavior [3]. Significant electrical behavior changes have been shown in top vs bottom gated thin film devices [23] and in uncovered devices measured in air versus vacuum [24] [22] [25] [26] [27] [28]. Surface absorbents in air cause charge scattering and can change the carrier type (for instance p-type doping in oxidized WSe_2) [24] but this effect can be reversed in vacuum, unlike in organic semiconductors where the effect is permanent [5].

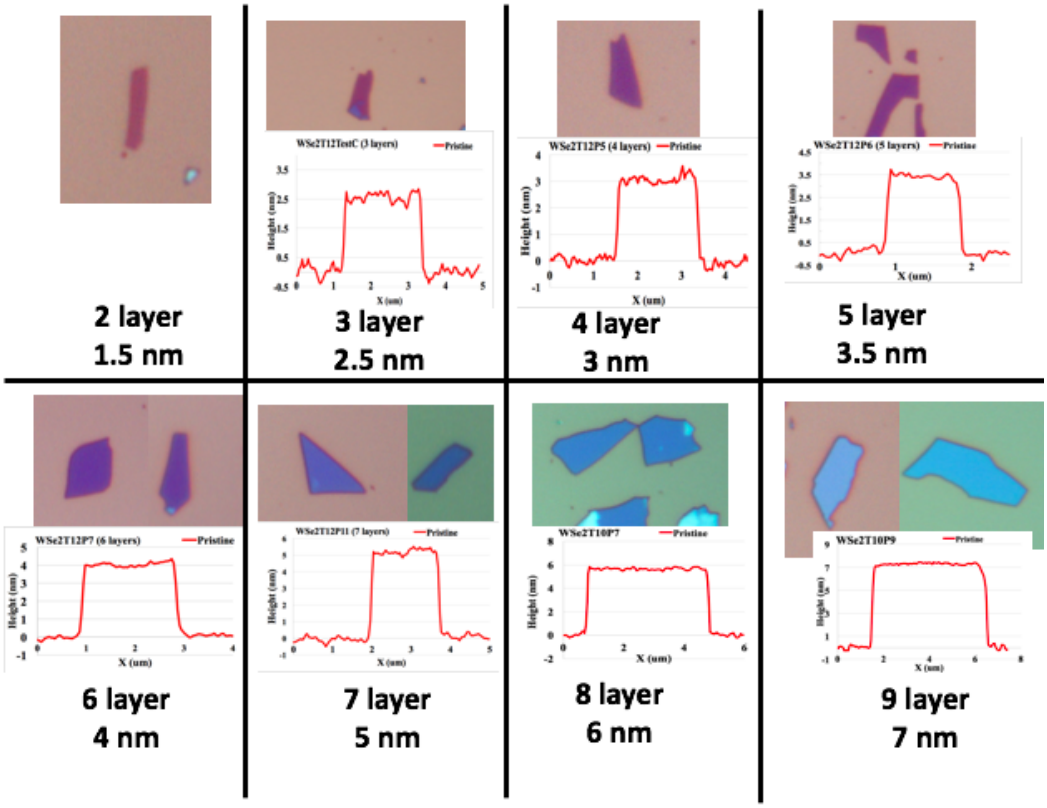

Figure 1.3: Optical images and AFM scans of WSe2 from bi-layer to bulk

Charge mobility has a weak dependence on charge concentration unless in the charged impurity scattering regime when temperatures drop below 10 K [19].

The most notable and studied thickness dependent effect is the transition from an indirect band gap in some bulk TMD materials to a direct band gap in their monolayer counterpart, for example WSe_2 in Figure 1.4 [14] [6] [29] [30]. The indirect band gap occurs at the gamma point while the direct band gap in the monolayer is at the K-point [14] [31] [32] [33] [34] [30]. The presence of energy-degenerate valleys, at the K-point [35] opens up the potential for TMD use in valleytronics. Valleytronic devices, like more well known spintronic devices, store information in addition to the classic Boolean on/off logic [3]. While spintronic devices detect electron spin, valleytronics differentiate degenerate valleys through valley polarization [35]. Application of this technology in monolayer MoS_2 has been shown to be successful through use of circularly polarized light [36]. There has been research into inducing this bang gap transition in few layer WSe_2 samples through strain [37] which could improve direct band gap material carrier mobility as well as their optoelectronic properties.

1.1.3 Band Gap Structure

Molybdenum and tungsten based TMDs have been shown to possess indirect band gaps of about 1.2 eV and direct band gaps at the monolayer reaching 1.9 eV [31]. This indirect-to-direct transition enhances photoluminescence efficiencies by a factor of 4x [14] and places TMD band gaps in the visible light range of electromagnetic radiation energy [3]. This property is important because a photon of energy equal to or greater than than the materials band gap will create free carriers or bound excitons, electron hole pairs. Once exposed to an internal or applied electric field, excitons generate a photocurrent which turns the device on [3]. When a bandgap is in the visible range, exposure to visible light, or any higher energy radiation such as ultra-violet, will promote valence band electrons to the conduction band and thus a conducting state. Conversely, with appropriate contact metals and band off-sets, solid state light emitting diodes or lasers are also possible. This quality can be used to make electronic devices which detect and manipulate light, called optoelectronics [38] [32]. Initial monolayer MoS_2 optoelectronic devices displayed poor photoresponse not much better than graphene, thus a lot of light was needed to produce a small photocurrent [32].

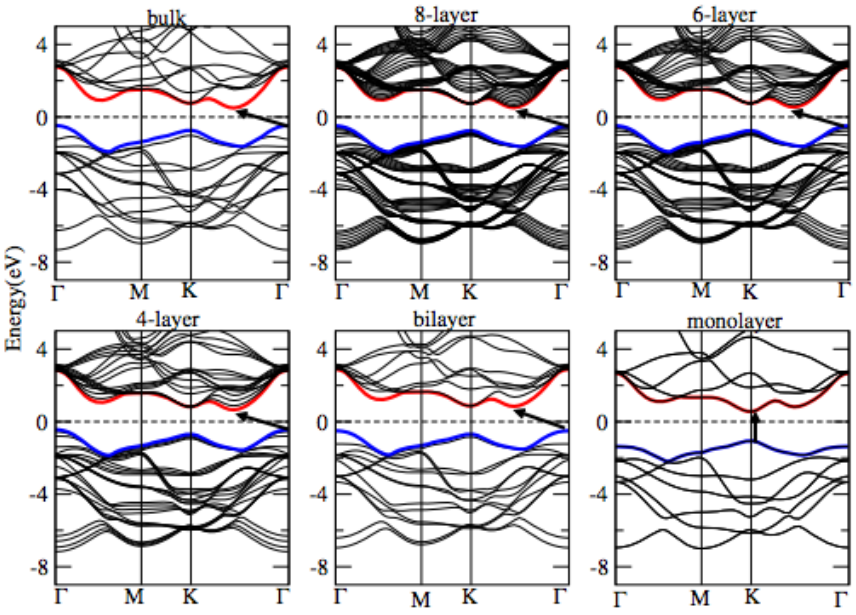

Figure 1.4: Band structure of WSe_2 from bulk, with an indirect band gap from the gamma to K point, to monolayer, with a direct band gap at the K point, calculated by source [39]

But with improved mobility and reduced contact resistance, recent monolayer MoS_2 photodetector response has been improved 100,000x reaching 880 A/W [40].

1.1.4 Simple Circuits

The most basic and common feature of modern electronics is the p-n junction. Illustrated in Figure 1.5 this device allows current to flow when in forward bias, and no current when in reverse bias. There are many ways to make a p-n junction, and once realized, more complex electronics such as logic gates and LEDs can be created. Developing TMD p-n junctions has been, not surprisingly, a main goal in research. Currently, the most common p-n junctions are made from doping, however controlled doping techniques limit doping success in thin film TMDs. Heterojunctions are a common way to make p-n junction, which use two different materials in contact with each other. Vertical heterojunctions have been created from TMD thin films stacked together with other thin film hybrid devices [41] [42].

Since there are such major behavioral changes depending on thickness, lateral homojunctions made by contact between two areas of the same material with different thicknesses are also possible between monolayer and few layer TMDs [43] [44] [8] [45] but a successful device has been presented as of now. Another way to tune device behavior which will be discussed further is through ion irradiation and thus defect introduction. Stanford et. al have shown a homojunction between pristine and He+ irradiated few layer WSe_2 is possible [46] and took this technique a step further in single layer materials and introduced atomic layer circuits including a working inverter by selected area ion irriadiation [47]. Other more complex applications of TMDs that have been created are gas sensors [48] [34], ring oscillators [49], and SRAM cells [49]. While not yet realized, the properties of TMDs and the creation of flexible substrates like H-BN and ion gels show promise for flexible, transparent, and stretchable electronics [3] [41] [50].

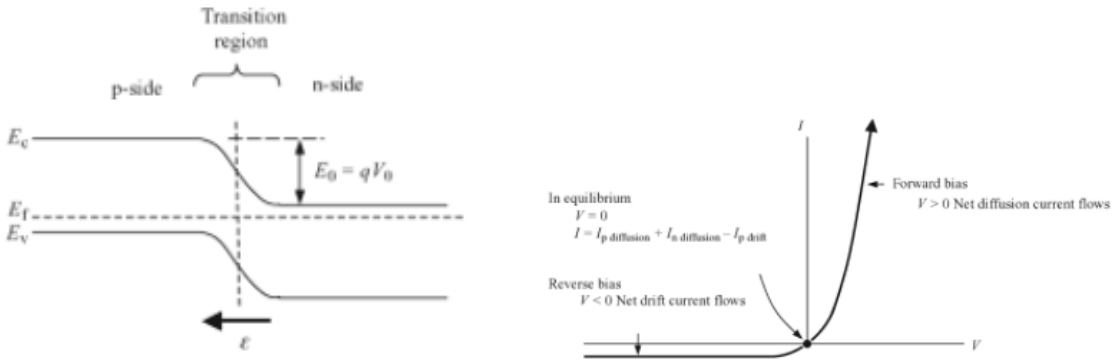

(a) Band diagram of a p-n junction

(b) I-V characteristics of a p-n junction

Figure 1.5: Physical and electrical depiction of a p-n junction from source [51].

1.2 WSe2

1.2.1 Background properties

The most studied TMD up to this point is MoS_2. A significant amount of background work has been done on the properties, growth, and application of this material. However, this work will focus on WSe_2 which has a smaller direct band gap than MoS_2, 1.65eV vs 1.8eV but displayed unique properties which makes it interesting for the development of complex devices [52]. While MoS_2 is mostly n-type, WSe_2 has shown ambipolar, n-type and p-type behavior depending on thickness and contact material [52] [21] [12] [53]. Control over carrier type is highly desirable and this trait shows promise to producing p-n junctions in WSe_2. WSe_2 has also been shown to have higher carrier mobility that MoS_2 [21]. In addition, WSe_2 has a high photoluminescent quantum yield, strong spin-orbital coupling, high adsorption coefficient in the visible range, and the lowest thermal conductivity among dense solids [52] [54] [55]. WSe_2 is a very stable thin film in atmosphere as it is more resistant to oxidation than other sulphides TMDs [12]. These qualities make WSe_2 an exciting and useful material to study. WSe_2 follows the classic layered TMD X-M-X structure described previously [6]. The M-M bond length between selenium atoms is 3.15 A, slightly larger than sulfides since selenium is a larger atom [3]. WSe_2 has been produced in both the more common trigonal prismatic 2H coordination and the octahedral 1T coordination [56].

1.2.2 Raman

The Raman spectrum of WSe_2 is thickness dependent and a quick and useful tool to distinguish mono and bilayer flakes without damaging the sample. The largest peak is the E^2_{g1} peak which shifts from 250 cm^{-1} with increasing flake thickness [6]; this peak represents the in plane vibration, thus the higher in plane order and symmetry, the higher the E^2_{g1} peak [30] [29] [52] [57] [34] [15]. The A_{1g} peak is smaller and, some claim, directly to the high-energy side of the E^2_{g1} peak at about 257 cm^{-1} [58]. There is disagreement on where exactly the A_{1g} peak is as the theoretical and experimental results conflict, some label this peak as 2LA(M) which is a second order mode due to LA phonons at the M point in the

Brillouin zone [59] which is how this peak is reference in Figure 1.6 from Zhao et al. [6]. the A_{1g} peak represents the out of plane vibration, thus if there is significant disorder in the lattice, atom vibrations will be vibrate out of plane and thus the A_{1g} peak will increase. The last peak of interest is at about 308 cm^{-1} and disappears in the monolayer thickness. With layer reduction from bulk to monolayer, peaks exhibit an approximately 1 cm^{-1} shift up in energy. This is a smaller shift than other TMDs possibly due to the larger atomic masses of tungsten and selenium than molybdenum and sulfur [6]. As layers are removed, the $E^2{}_{g1}$ sharpens, in plane vibrations become more uniform, but the A_{1g} mode broadens, out of plane vibrations disperse with decreased lateral stress [6]. At the monolayer thickness both the A_{1g} and $E^2{}_{g1}$ become degenerate which agrees with theoretical findings [6]. While the A_{1g} mode shows peak broadening with electron doping, $E^2{}_{g1}$ is unaffected, suggesting there is stronger electron-phonon coupling with the out of plane vibrational mode than the in plane mode [15]. Photoluminescence (PL) is another important and layer dependent measurement used to characterize TMD thin films. The indirect to direct band gap shift at the monolayer thickness increases PL emissions 100x to 1000x compared to bulk material [30] [29].

1.2.3 Band Gap Structure

The indirect band gap at the gamma point in the valence band exhibited in bulk WSe_2 is the same as MoS_2, 1.2 eV, but the direct band gap between K points at the monolayer thickness is slightly smaller at 1.65 eV. This reaches just into the visible spectrum of red light and so WSe_2 is still useful for optoelectronic applications [29] [6]. In the monolayer form, photoluminescence of WSe_2 is centered at 750mm, emissions are 100x to 1000x stronger than bulk WSe_2 emissions due to the indirect to direct band gap transition. There is a significant thickness dependent shift of the A and B peaks. which suggests strong interlayer coupling [30]. Another way to increase PL emission without thinning the sample to the monolayer is to induce strain. Figure 1.7 from Desai et al shows 35x increased PL intensity in multilayer WSe_2 under 2% uniaxial tensile strain compared to unstrained multilayer WSe_2 [37]. A concomitant shift in the band structure of WSe_2 from indirect gamma K band gap of 1.2 eV in the monolayer to a direct K- K band gap of 1.65 eV in the monolayer has been observed [15].

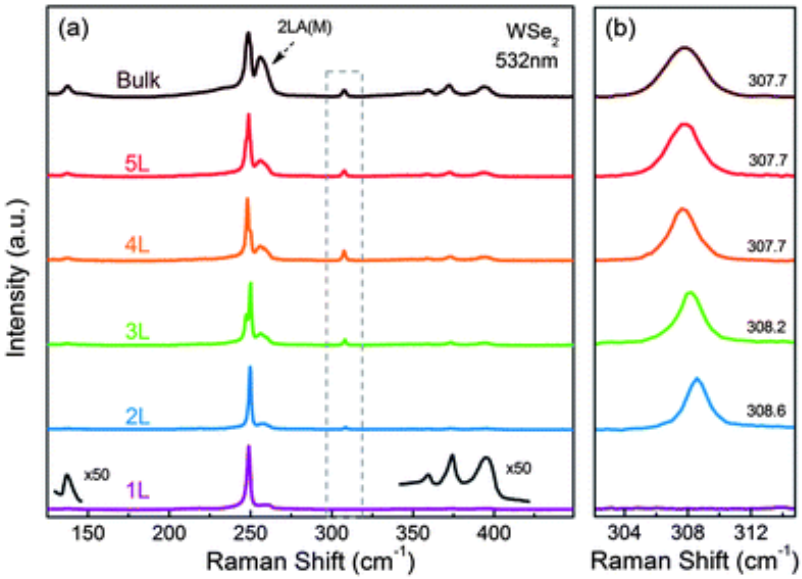

Figure 1.6: Raman spectrum of WSe2 from bulk to monolayer

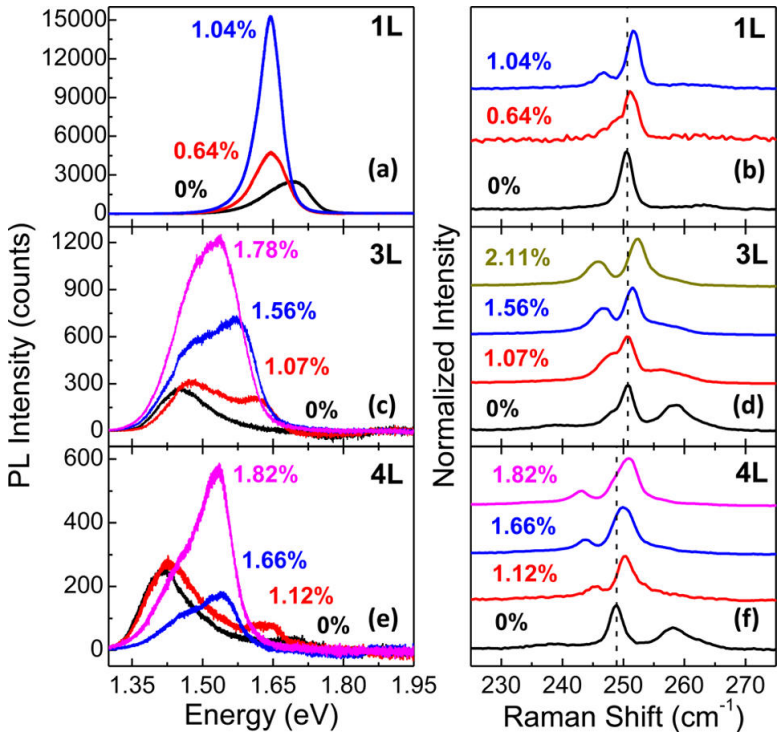

Figure 1.7: PL and raman spectrum of monolayer, trilayer, and 4 layer WSe_2 under increasing uniaxial tensile strain

1.2.4 Charge Carrier Control

One of the characteristics which makes WSe_2 an interesting and promising material is its charge carrier behavior. Depending on WSe_2 thickness, electrode material, and processing, one can make WSe_2 thin film transistors of n-type, p-type, or ambipolar behavior [52] [21] [20] [12] [53]. Work by Pudasaini et al in Figure 1.8 shows the transition of WSe_2 with Cr/Au contacts from p-type at the monolayer to ambipolar to n-type in thick few layer flakes [53]. This quality opens the door for complex circuits on a single WSe_2 crystal. There have been multiple demonstrations of working inverters on single crystal WSe_2 flakes which has been difficult to produce with MoS_2 [57] [53]. WSe_2 is importantly more air stable than other TMDs but surface interfaces still impact electrical performance to a high degree [20]. Like MoS_2, WSe_2 behaves significantly different in atmosphere versus vacuum and is capping layer sensitive. One recent research focus has been the conversion of WSe_2 into WO_x in the presence of oxygen and heat which caps the underlying WSe_2 and switches multilayer devices to strongly p-type [20] [43] [60] [44] [53].

1.2.5 Growth

Growth of WSe_2 was initially achieved by direct heating of pure W and Se, vapor transport growth, and WO3 powder reaction with H_2Se [33] [61] [62]. These samples were small, on the micron scale, and had very low carrier mobility . Recent research on effects of temperature, such as the work by Liu et al in Figure 1.9, growth time, and chemical specie ratios have improved monolayer crystal size, shape, and material performance [52] [57]. Chemical vapor deposition (CVD) grown WSe_2 samples have reached sizes up to $1cm^2$ for a single domain with high carrier mobility up to 100 $cm^2V^{-1}s^{-1}$ in the monolayer and 350 $cm^2V^{-1}s^{-1}$ in few-layer samples [29]. Large area CVD growth has been successful on different substrate materials. Recent work on sapphire for instance was accomplished through the selenization of WO_x powers [57]. Direct vapor phase sublimation of $WSe2_2$ powders has also shown to be an effective growth method, resulting in flakes that display similar optical quality to mechanically exfoliated samples [54]. The growth method, of course effects the material quality and thus has an impact on electrical behavior.

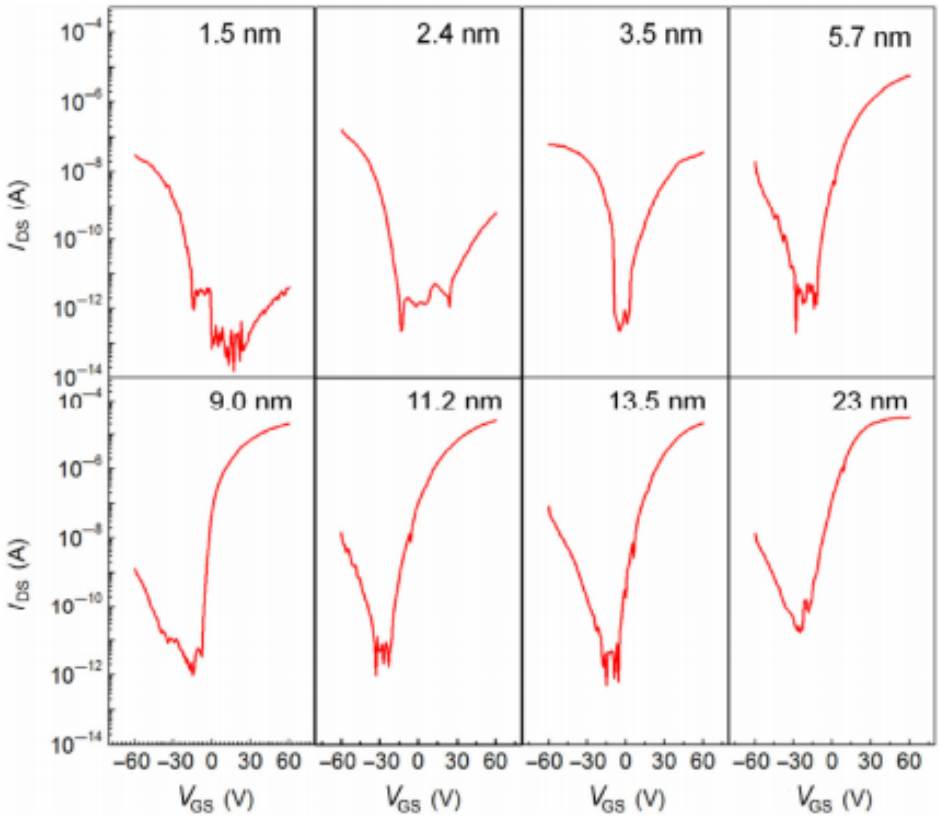

Figure 1.8: Transition of pristine WSe_2 from p-type (1.5-2.4nm) to ambipolar (3.5nm) to n-type (5.7nm+) with Cr/Au contacts from Source [53]

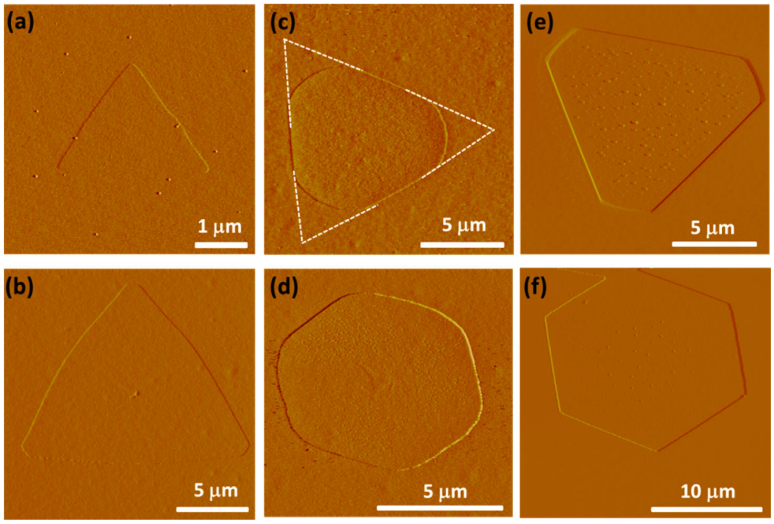

Figure 1.9: WSe_2 grown by CVD at (a) 900 (b) 950 (c and d) 1025 (e and f) 1050 degrees C

For instance, CVD grown WSe_2 has ambipolar behavior while direct vapor phase sublimation samples show p-type behavior [29].

1.2.6 Contact resistance

A challenge that needs to be overcome before large scale WSe_2 thin film transistor production is the high resistance present at the semiconductor and electrode interface [3] [21]. An Ohmic contact,with minimal resistance between the two materials and current can flow at the small applied source drain voltage is desirable; this is evidenced by a transfer curve with a constant linear relationship between voltage and current in Figure 1.10b. When there is high resistance at the junction, a Schottky barrier forms and a certain forward bias is needed to overcome the barrier height which is typically associated with the difference in the alignment of the metal work function and either the conduction band or valence band for n- and p-type materials, respectively [55], this is illustrated in Figure 1.10a. Basic methods to reduce surface resistance is to anneal the sample and ensure surface/interface cleanliness (reduce oxides for instance). The deposition method for the metallization and vacuum at which metallization occurs also have a significant impact on contact resistance [3].The electrode material is a direct way to improve device behavior [12]. Doping the contacts region [21] and depositing a barrier layer between the WSe_2 and the contact, such as MgO or TiO_2 [63], have shown increased carrier density by decreasing barrier height between the semiconductor and contact if a high work function metal is required.

1.2.7 FET fabrication

WSe_2 thin film transistors are fabricated through a series of meticulous steps illustrated in Figure 1.11. The first step is to obtain a thin film sample via the various growth methods described earlier, or through a process called exfoliation which cleaves thin films from bulk crystals. Exfoliation can be either chemical [1] [64] [65] or mechanical [36] [66] by the scotch tape method. While not proven true for mechanical exfoliation, studies have show chemical exfoliation using shear stress produces larger and thinner TMD [67] as well as graphene [68] flakes in a controllable process.

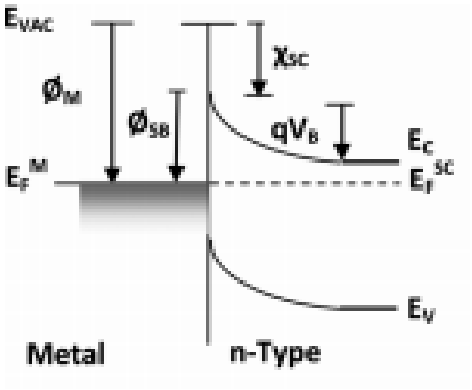

(a) Band diagram of a Schottkey contact

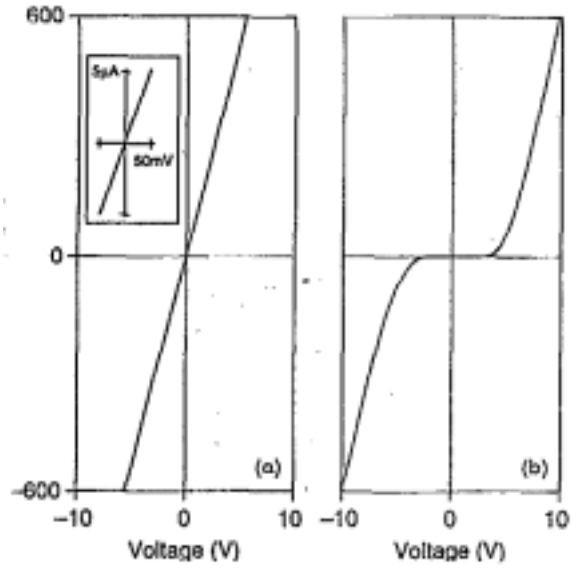

(b) I-V characteristics of an Ohmic and Schottkey contact

Figure 1.10: Diagram of (a) Schottkey contact from Source [69] and (b) electrical behavior of contact type from Source [70].

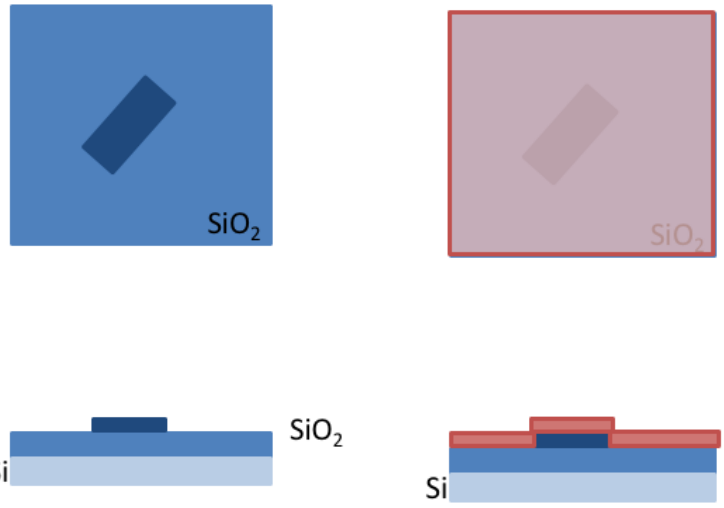

(a) Flake exfoliated onto substrate

(b) Sample is coated in a resist material

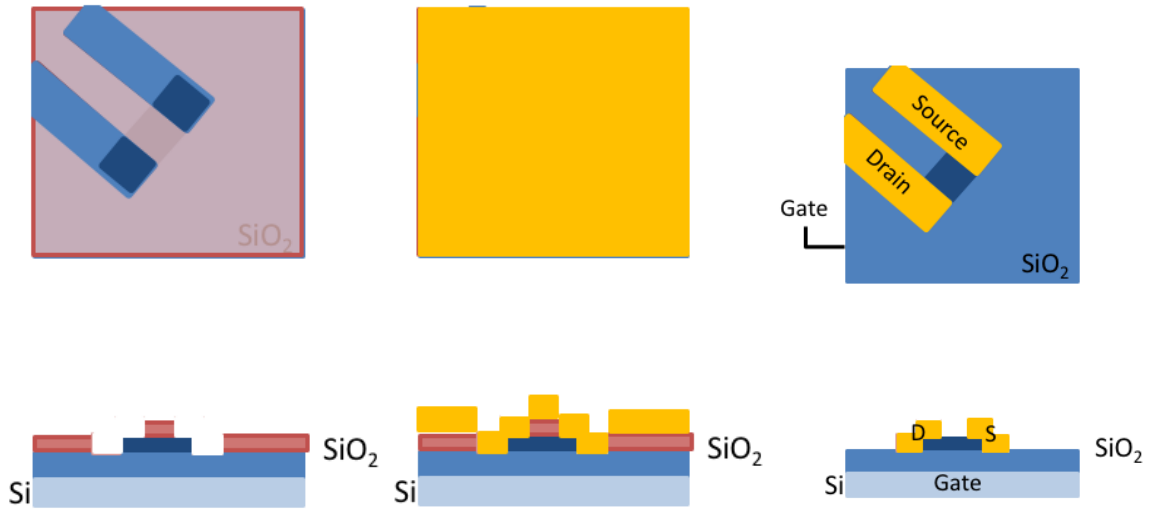

(c) Exposed areas are preferentially dissolved away

(d) Sample is metallized

(e) Resist removed which leaves device contacts

Figure 1.11: Fabrication process of a thin film transistor

Once exfoliated onto a substrate (Fig 1.11a), desired flakes are located and thickness identified. Atomic force microscopy (AFM) is a precise method to determine thickness, however this takes time and optical identification of flake thickness based on color and contrast has been proven a reliable, and much faster method [16]. Devices are designed custom to each flake in AutoCAD®software and written into a resist (for instance PMMA) mask layer (Fig 1.11b) with an electron beam lithography system. Once developed (Fig 1.11c), the samples go through metallization (Fig 1.11d) by either sputtering or electron beam evaporation. When the PMMA mask is lifted off with acetone, just the electrode area which had direct contact between the substrate and the metal are left. These devices then go through subsequent processing (anneal, plasma treatment etc.) to tune electrical and optical properties.

1.3 Defect Engineering

1.3.1 Background

For TMDs to be practical for electrical device applications, tuning of carrier type, mobility, and density must be achieved in a controllable way. In bulk materials, this can be achieved in a variety of ways. Chemical doping is a common and well established method to control properties which introduces foreign atoms or molecules to of a sample. These impurities interact with the original material and alter electrical, optical, and structural characteristics. Doping can occur *in situ*, during material growth, or *ex situ*, after growth. By controlling precursor atom ratios, *in situ* substitutional doping has been achieved in CVD grown bulk TMDs which can then be exfoliated to thin films [71] [72]. To this point, oxygen is the only non-group 6 or transition metal element successfully grown into the matrix [71] and even with simple substitution within group 6 elements, this method increases lattice distortion and decreases carrier mobility [3] [72]. Elements other than group 6 and oxygen, are adsorbed to the surface as adatoms at certain sites above lattice atoms, or at the center of the hexagonal void in the TMD structure. These atoms can be highly mobile, sometimes even at room temperature, and thus are not sable for practical use [71].

1.3.2 Doping

In chemical doping through ion implantation, a mask layer allows for extremely high levels of precision. Ions are accelerated towards the sample in an electric field and bombard any exposed regions [72]. This method requires ions to have high enough energy to eject lattice atoms and break bonds. In bulk material this can be fixed with a simple anneal, however in thin films the damage is more significant and etching which is negligible in bulk samples can obliterate mono and few-layer materials [72]. Surface charge transfer doping is a non-destructive method which shows promise for TMDs with extremely high surface to bulk ratios [72]. DFT modeling has shown that even low levels of adsorbed molecules is effective in carrier tuning [73] however in practice the effect degrades over time [3].

1.4 Energized Beams

Doping methods have been successful in bulk semiconductors for decades, however the unique properties of TMD thin films requires a different solution for behavior manipulation. Defect engineering is the conscious introduction of defects to a lattice and is typically performed with an energized beam. Direct focused beam methods are convenient for prototyping as they have nanoscale precision which is limited by beam size, currently about a couple of nm but is constantly being improved and reduced [74] . The process is extremely controllable through beam current and power and with computer programming could be scaled up [Zhao, Doping].

1.4.1 Defect Classes

0D

There are two classes of defects of importance in defect engineering, vacancies and lattice distortions. In 2H TMDs there are 6 specific vacancy point defects which can arise from vacancies, examples of these defects in 2H-MoS_2 are shown in Figure 1.12.

O2/VacancyDefects.png Aging/VacancyDefects.png

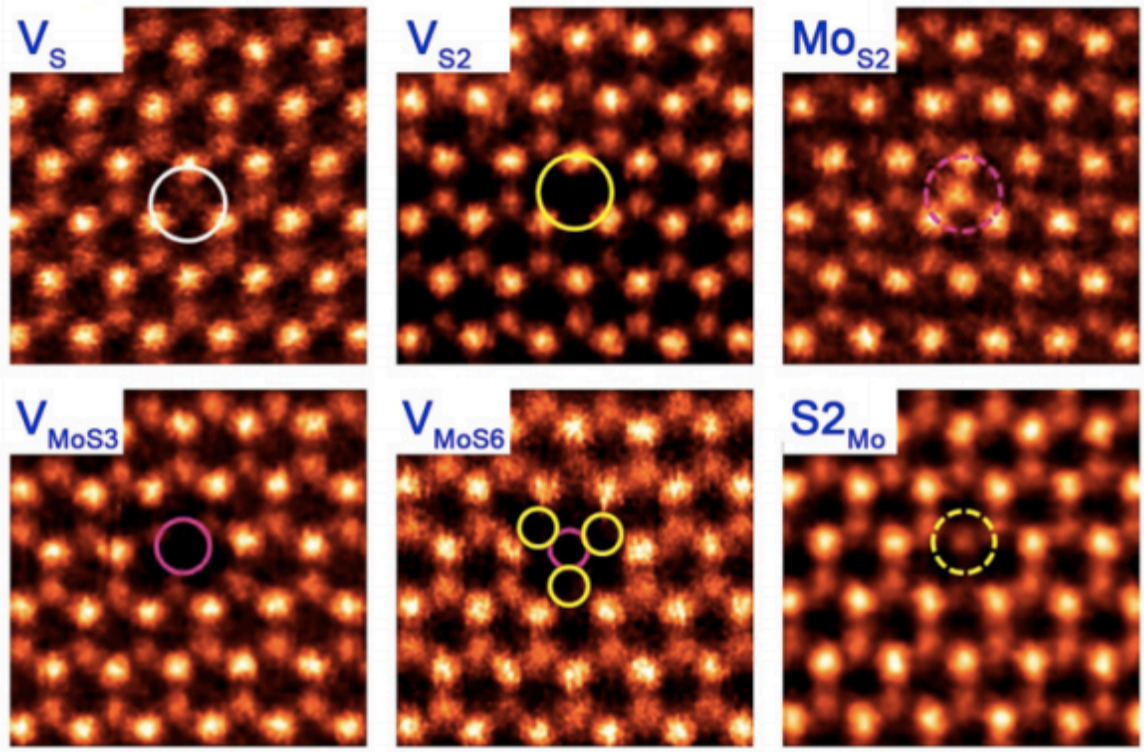

Figure 1.12: TMD vacancy point defect types from Source [71]

The vacancy of one chalcogenide on one side of the X-M-X sandwich, V_x, a pair of chalcogenide vacancies on either side, V_{x2}, a vacancy group of one center layer transition metal and three corresponding chalcogenides from one side, V_{mx3}, a vacancy group of one center layer transition metal and six corresponding chalcogenides, three from each side, V_{mx6}, and antisites when a transition metal occupies a chalcogen pair vacancy, M_{x2}, and when a chalcogen pair occupied a transition metal vacancy, X_{sm} [71]. Besides M_{x2}, these vacancy point defects maintain trigonal prismatic symmetry which reduces lattice stress [71]. The lowest formation energy, and most common, vacancy defect is V_x. The specific value depends on the TMD chemical makeup, for WSe_2 it is 2.81eV [75]. These single chalcogen vacancies releases an unpaired electron into the lattice to act as a hole trap or an additional n-type carrier [76] [77]. These defect sites are essential dopants and provide a site within the TMD bandgap, so when carrier concentration is low electrons transport via hopping between defect sites [78]. Stanford et al performed DFT calculations, in Figure 1.13 on the effect of various defects on the band structure of WSe_2.

1D

When there are sufficient chalcogen vacancies which line up, line vacancies can form, usually in a zig-zag pattern across the surface of a TMD layer [71]. Calculations on these line vacancies show increased conduction in the direction parallel to the line which can reach metallic levels [47] [79]. It has been experimentally proven that strain can be used to determine directionality of these lines increasing control over damage effects [79]. Grain boundaries occur in TMD just as in all crystalline materials, however bulk growth has been optimized so most mechanically exfoliated samples are from single crystals. Grain boundaries could be useful in property manipulation as its been found that at a 60 degrees rotation , grain boundaries can result in triangular inversion domains with metallic edges [80] [Vacancy-induced formation]. This can be achieved through precise growth. Edges are another lattice distortion determined by growth, CVD grown monolayers are generally triangular however depending on precursor ratios hexagonal flake are also possible [71].

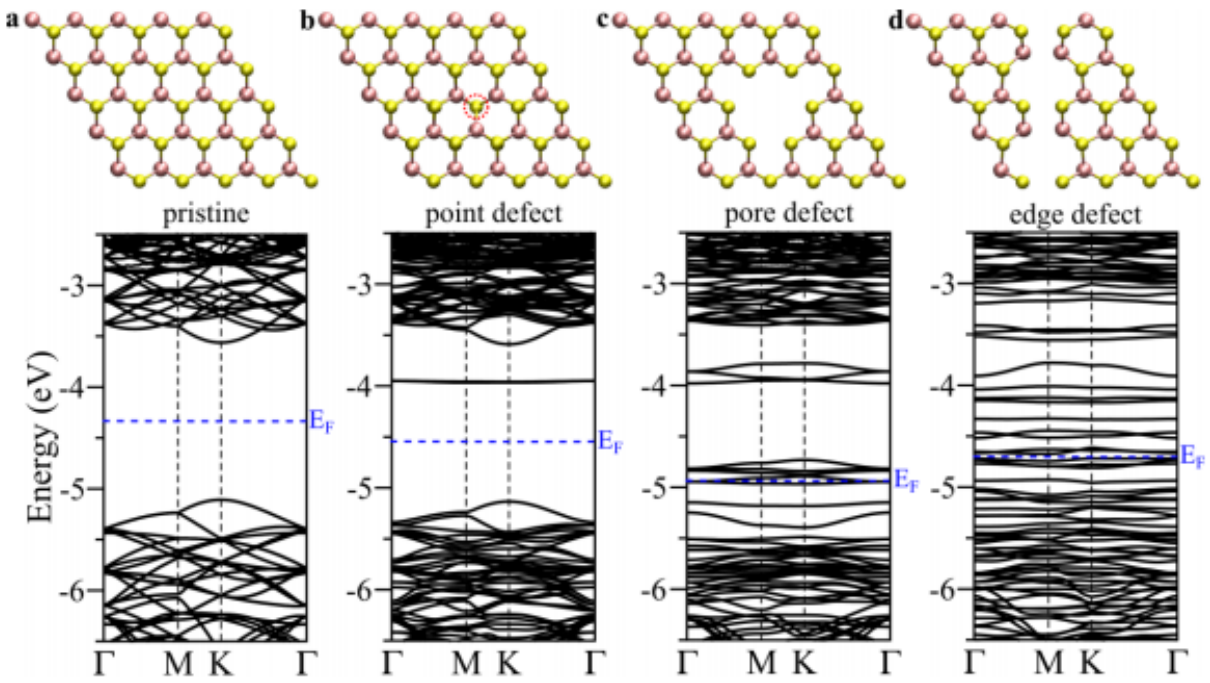

Figure 1.13: Interband states created by defects in monolayer WSe_2. A hole doping effect occurs with point vacancies such as V_x and $_{mx6}$ but with line vacancies there are enough interband states for metallic conduction along the line

3D

Rippling of TMD layers is an example of 3D defects which can occur in 2D materials. This effect can be generated deliberately with a laser beam or might occur if monolayers are exfoliated onto dirty or rough substrates and introduces anisotropic strain in the material [71].

1.4.2 Examples

Specific defects can improve device behavior in beneficial ways, defect engineering aims to control behavior by controlling defects. With the combination of theoretical and experimental studies, the energy required to produce specific defects is well established. Manipulation of irradiation dose and annealing time can control the density of defects induced in a sample [76] [47]. Heavy irradiation will destroy a TMD device, but finely tuned beam current, dose, and energy has been shown to improve device performance by producing the right amount of damage to maintain material integrity [76] [81] [82]. MoS2 irradiated with swift heavy ions (SHI) of U^{28+} showed structural and electrical changes which at low doses improved behavior but at heavy doses destroyed the transistor [83]. Graphene is typically more radiation hard than TMD materials due to graphenes ability to dissipate electronic energy. TMDs are unable to transfer electric energy as efficiently thus the energy density is greater which causes more damage at lower doses [28]. The transition through various stages of damage is illustrated in Figure 1.14 while damage at first limits conduction, upon further damage chalcogenide vacancies merge to form vacancy lines parallel to the channel and increase conduction to metallic levels [84] [47]. Through proton irradiation, magnetism has been induced in MoS_2 [85]. In n-type MoS_2, proton irradiation has been shown to increase the positive gate threshold voltage of a thin film transistor. This effect is due to the irradiation induced hole traps at chalcogen vacancies [81]. The irradiation induced changes were not stable, as recovery of pristine behavior occurred after a few days; while not elaborated it is assumed that isoelectronic oxygen reacted and filled the chalcogen vacancies [81].

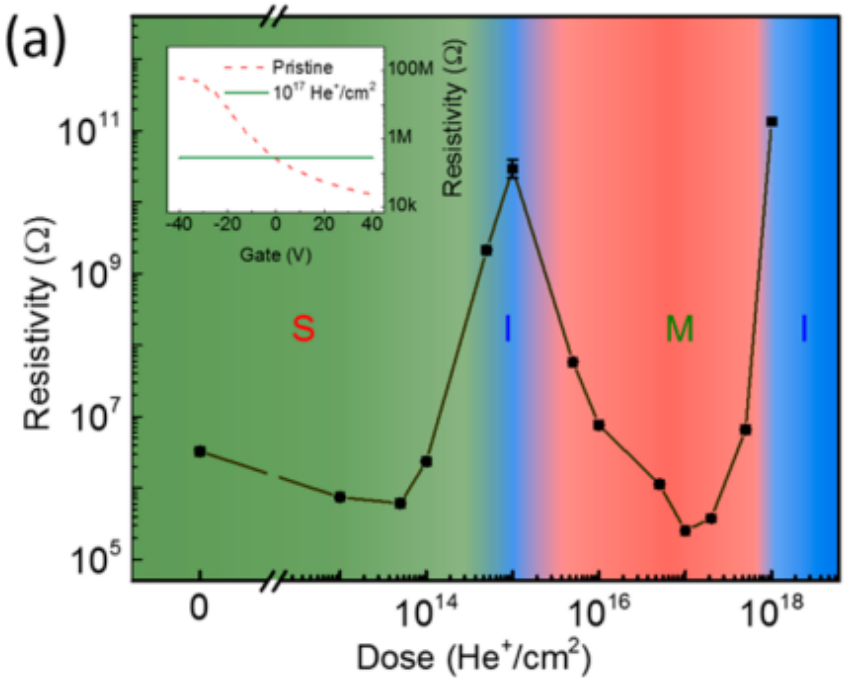

Figure 1.14: Effect of increasing irradiation dose on MoS_2 resistivity from source [84]

Another study found increased and novel photoluminescence in WSe_2, MoS_2, and $MoSe_2$ after irradiation with alpha particles [76]. Damage was shown to introduce a new emission peak about 0.15 to 0.25 eV below the free-excitation PL peak which is within the bandgap. In addition to the new PL peak, overall PL intensity increased with damage however these effects disappeared when measured in vacuum indicating effects must be due to interactions between defects and ambient gas molecules such as N_2 or O_2, however O_2 is more likely due to a higher binding energy [76].

1.4.3 Oxygen Plasma

The interaction between oxygen and thin film TMDs has become a focus of research as a means of manipulating behavior. One way this has been studied is through remote oxygen plasma exposure [44] [8] [86]. Oxygen atoms are ionized and radicals diffuse through the chamber to the sample located at a distance from the plasma source. In classic plasma cleaners, plasma species are accelerated towards and bombard the sample which causes a sputtering effect and will damage thin films. The oxygen is chemically adsorbed by the top most layer and forms bonds with tungsten, or the present transition metal, to grow an amorphous oxide layer [44] [8] [71] [82]. O_3 exposure, such as in Figure 1.15, and thermal annealing in ambient atmosphere has shown similar oxidation effects [20] [43] [60], however due to the lateral growth of tungsten oxide across the sample surface, a quick plasma treatment increases control over the process and does not cause as much damage to the underlying pristine sample [8] [44]. The existence of a single top oxidized layer is difficult to prove as it is amorphous, and will not appear on a raman spectrum, and a single layer on top of bulk crystal is too thin to see in most electron microscopes. X-ray photoelectron spectroscopy, (XPS), such as Figure 1.16 has been used to detect the presence of oxygen in O_2 plasma exposed samples.

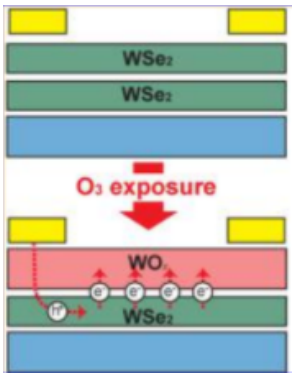

Figure 1.15: Top layer oxidation of WSe_2 by ozone exposure from Source [60]

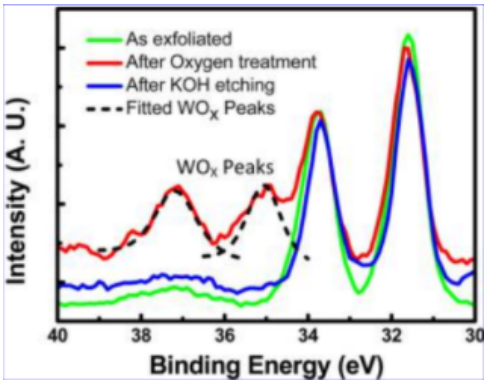

Figure 1.16: Detection of amorphous single layer WO_x by XPS from Source [44]

Self-limiting

Oxidation is self-limiting, oxygen does not diffuse through the amorphous WO_x or MoO_x layer even when exposed to extended periods of plasma [44] [8]. Proof that the underlying TMD layers remain pristine has been presented through raman and PL studies in Figure 1.17 by Li et al. Triple layer samples display distinct pristine bi-layer behavior after oxygen plasma exposure, bi-layer samples display pristine monolayer behavior and monolayer samples show no TMD behavior after exposure [44] [8]. Electrically, the amorphous oxide capping layer p-dopes the underlying material. WO_x and MoO_x have a higher electron affinity than their selenide TMD material and draw electrons from the pristine material into the top oxide layer [82] [20] [60] [8] [53]. Transition metal oxides have also been shown to be good hole injection layers when used as a barrier between the TMD and electrode, increasing p-type behavior of the device [77] [87]. Theoretically, this effect could be used to create homojunctions between n-type WSe_2 and p-type WO_x capped WSe_2 but experimentally this has not been accomplished yet.

Thinning

There have been attempts to thin TMD samples layer by layer by removing the amorphous oxidation layer through a KOH bath [44], argon ion cluster etching [43], and high temperature annealing under ultra high vacuum [8]. XPS and AFM studies of these sample show chemical and physical success, however no electrical data has been presented that proves samples retain conductivity and carrier mobility. Layer dependent electrical behavior has been reported in WSe_2 with Cr/Au contacts [53] so successful layer by layer thinning could result in a lateral WSe_2 p-n homojunction through thickness modulation. With the improvement of CVD grown WSe_2, this technology could produce complex circuits made entirely of WSe_2 on large area grown flakes.

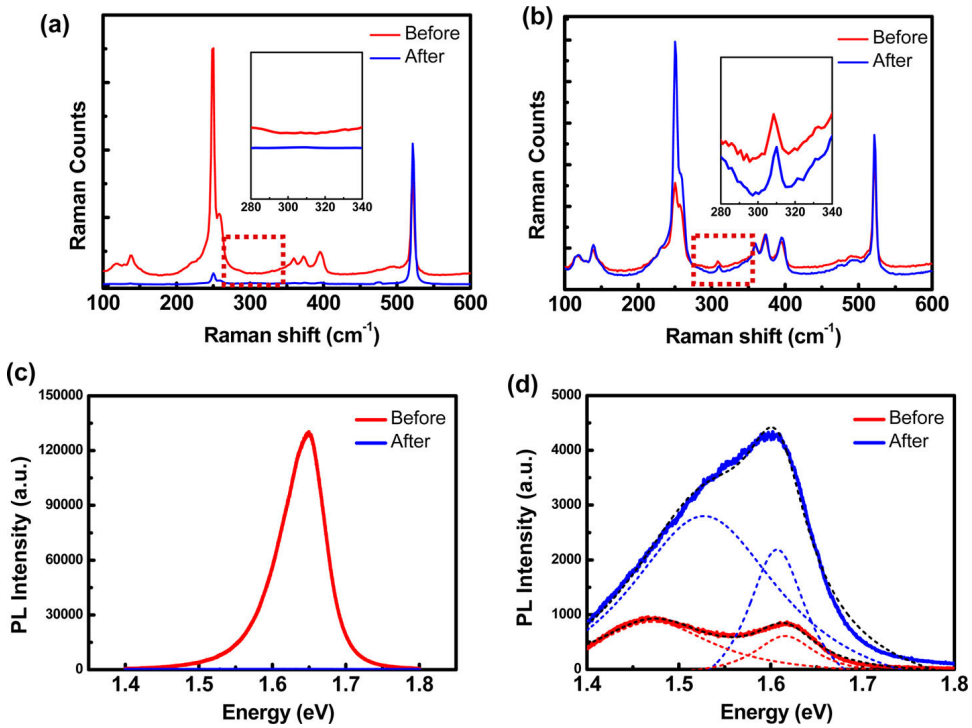

Figure 1.17: Monolayer WSe_2 raman (a) and PL (c) spectrum before and after O_2 plasma exposure. No evidence of WSe_2 remains after exposure. Trilayer WSe_2 raman (b) and PL (d) spectrum before and after O_2 Plasma exposure. PL intensity after exposure increases significantly and matches expected levels from bi-layer WSe_2

1.5 Outlook

Moving forward, TMDs are a promising material which require more research before widespread application in consumer products. These materials have high potential for numerous nanoelectronic applications due to successful growth, monolayer direct band gaps, and optoelectronic function, and are worth investing in. There are still hurdles to master, like high contact resistance and monolayer processing without destruction, but with increased demands on data processing speed and storage minimization researchers will develop novel solutions to these problems.

[88] [89] [90] [91] [92] [70] [51] [39] [11] [10] [46] [53] [47] [71] [84] [5] [37] [12] [6] [60] [44] [3]

Chapter 2

WSe2 Ambient Effects

A version of this chapter was originally published by Anna N. Hoffman, Michael G. Stanford, Cheng Zhang, Ilia N. Ivanov, Akinola D. Oyedele, Maria Gabriela Sales, Stephen J. McDonnell, Michael R. Koehler, David G. Mandrus, Liangbo Liang, Bobby G. Sumpter, Kai Xiao, and Philip D. Rack: Hoffman, A. N.; Stanford, M. G.; Zhang, C.; Ivanov, I. N.; Oyedele, A. D.; Sales, M. G.; McDonnell, S. J.; Koehler, M. R.; Mandrus, D. G.; Liang, L.; et al. Atmospheric and Long-Term Aging Effects on the Electrical Properties of Variable Thickness WSe2 Transistors. ACS Appl. Mater. Interfaces 2018, 36540-36548 Anna N. Hoffman conducted the device fabrication, electrical, and optical characterization, analysis and wrote the manuscript. Michael G. Stanford, Cheng Zhang, Ilia N. Ivanov, Akinola D. Oyedele, and Kai Xiao facilitated device fabrication training and helped with the electrical and Raman measurements; Maria Gabriela Sales and Stephen J. McDonnell performed XPS characterization. Liangbo Liang and Bobby G. Sumpter performed DTF calculations. Michael R. Koehler and David G. Mandrus grew the WSe2 bulk crystals. The manuscript was written through contributions of all authors. The manuscript has been slightly modified to include the supplemental material.

2.1 Background

Since the demonstration of graphenes remarkable properties in 2004 [1], layered 2D materials have been the focus of intense research. For many electronic applications graphene is not ideal due to the absence of a bandgap, however this challenge has inspired the investigation of other layered materials. Transition metal dichalcogenides (TMDs) such as MoS_2, WS_2, $MoSe_2$, and WSe_2 have gained interest due to their unique properties applicable in 2D electronics. [3] [93] [94] Like graphene, these layered materials stack in clean, dangling bond-free surfaces, which allows for easy thin film device fabrication [12]. Unlike graphene, many TMDs have thickness-dependent bandgaps which make them attractive for electrical and optoelectronic applications. For instance, several TMDs possess a direct bandgap at the monolayer while at bilayer and thicker there is a transition to a smaller, indirect bandgap.[15] Layer dependence also impacts carrier concentration and mobility.[18] [19] These layer-dependent properties can be leveraged to tune the behavior of TMDs in optoelectronic devices. Previous work

on the layer dependent electrical characteristics of the Cr/Au contact scheme used in this study has shown a systematic shift in the carrier type with increasing layer thickness[93]; namely thinner flakes are p-type and as layer thickness increases, n-type conduction increases, which was rationalized based on the shifts in the conduction and valence band positions and subsequently the barrier height for each carrier. Interestingly, scanning tunneling microscopy (STM) of various metal contacts to MoS_2 have revealed that intrinsic defects can dominate the contact resistance and provide low n- and p-type Schottky barriers for carrier injection.[77] Regarding the Cr-WSe_2 contact region, the energy band diagram has recently been studied via XPS for bulk crystals.[95] The band gap (1.3 eV) and Fermi level position (0.34 eV from conduction band edge) of the pristine WSe_2 was initially determined and found to shift 0.34 eV towards the mid-gap after chromium was deposited in ultra-high vacuum, suggesting a larger than expected effective chromium work function (4.92 eV versus 4.5-4.6 eV). The larger effective work function could be due to $CrSe_x$ formation, which is thermodynamically favorable. The picture is more complicated for high-vacuum contact deposition in which XPS reveals CrO_x and WSe_xO_y was detected. Challenges to the realization of widespread TMD applications include controlled large area materials growth with consistent material properties.[57][29][96][97][98][99][100] Furthermore, the effects of routine semiconductor processing chemistries and environments need to be understood. While many TMDs are touted as air-stable, elucidating the effect of atmosphere is necessary as adsorption and oxidation can deleteriously affect the device properties.[101][102] Surface layers without dangling bonds are, in general, chemically inert but surface defects and flake edges are still vulnerable to physisorption of polar molecules. [18][19] Studies have shown various encapsulation methods can mitigate the atmospheric impact on thin films. However, the various encapsulation methods themselves can alter the properties of the functional thin film, which in what is studied here is the semiconducting channel region. Polymer spin-coated encapsulation has shown reduced structural degradation in TMD FETs[18], however, another report suggests that the TMDs transform from semiconducting to metallic and the electrical properties degrade after extended time in ambient.[19] Molecular doping can passivate surface defects, however this process obviously modifies intrinsic conduction and has been shown to degrade over time in atmosphere.[103][104] Encapsulation graphene or

hexagonal boron nitrate (h-BN) is a common method, which preserves device performance over extended exposure to atmosphere, but the stacking fabrication process is complex with high probability of cracks and is not practical for large scale fabrication.[105][106] Even as encapsulation methods improve, it is vital to understand of atmospheric and aging effects on these materials as inevitably the materials are exposed to ambient conditions during device processing. The effect of physisorbed species and oxidation on electrical properties of MoS_2 has been studied[102][107][108][109][110][8][82][111][112], but limited information is available for WSe_2. WSe_2 can be ambipolar[57] which provides the unique opportunity to observe the effects of ambient environment on n-type and p-type charge carriers. Additionally, it was shown that adsorbed atmospheric species and oxidation effects on selenides are more significant than on sulfides.[113] Here we demonstrate the reversible effect of physisorbed atmospheric gas on n- and p-type transport as a function of WSe_2 layers, by measuring the transfer characteristics of field-effect transistors (FET) in air and vacuum. The reversible characteristics are attributed to H_2O/O_2 physical adsorption, which preferentially depletes electron carriers.[114] Subsequently, we study the effects of long term exposure to atmosphere on the electrical properties of WSe_2. With prolonged exposure to atmosphere, n-type on-current decreases and p-type on-current increases. Density functional theory (DFT) calculations suggest that the observed changes can be attributed to chemisorption of molecular O_2 at selenium vacancies and isoelectronic O chemisorption of Se vacancies.

2.2 Methods

2.2.1 Fabrication

Bulk single crystal WSe_2 was synthesized via the vapor transport method. A heavily p-doped silicon substrate with a thermally grown 290 nm SiO_2 insulating layer was used for all field effect transistor (FET) devices. WSe_2 was mechanically exfoliated onto the substrates, which were previously cleaned via sonication in an acetone bath. Images of flakes were taken on an optical microscope equipped with a Nikon camera to record shape, thickness, and location of flakes. Poly(methyl methacrylate) (PMMA) resist was spin coated and source-drain contacts

were patterned via electron beam lithography on an FEI 600 Nova equipped with a Raith lithography package. Source and drain contacts of Cr (5nm) and Au (30nm) were electron beam evaporated at a rate of 1 Å/s at 2x10^{-6} torr and lifted-off in acetone.

2.2.2 Characterization

Raman spectroscopy was performed on a Renishaw inVia micro-Raman system using a 532nm excitation laser and a 100X objective. Electrical characterization was performed in a cryogenic vacuum probe system with a 4200 Keithley semiconductor device analyzer. After initializing venting or pumping, it takes approximately 2 minutes for the stage vibration to damp sufficiently to place the probe tips on the surface of the substrate, after which, transfer measurements were taken approximately every 20 seconds for 5 minutes, then each minute for at least another 5 minutes until the transfer characteristics stabilized. To gather a full transfer curve from -70V to 70V quickly, the precision of the measurement was reduced to about 0.1 nA. Thus all negative current values were eliminated and only positive values >0.1 nA are plotted. Devices were measured initially in air and vacuum immediately after fabrication, then aged in atmosphere and periodically measured in air and vacuum (and in one instance in an N_2 ambient) over a period of 900 hours. One device in the set was measured in air and vacuum after 3600 hours of ambient exposure to observe extended aging. X-ray photoelectron spectroscopy (XPS) data was collected using monochromatic Al Kα X-rays (1486.7 eV) at a pass energy of 26 eV in a PHI VersaProbe III UHV system, equipped with an auto dual-charge neutralizer. A spot size of 9 um was used. Spectral analysis was carried out using kolXPD software [115] to fit the features present in the W 4f and Se 3d spectra, and accurately determine peak positions. All peaks were fit with Voigt lineshapes.

2.2.3 Electronic Structure Calculation

Plane-wave DFT calculations were carried out via the VASP package [116] equipped with the projector augmented-wave (PAW) pseudopotentials. The exchange-correlation interactions were considered in the generalized gradient approximation (GGA) using the Perdew-Burke-Ernzerhof (PBE) functional.[117] Single-layer WSe_2 was modeled by a periodic slab geometry

with 18 Å vacuum separation in the out-of-plane direction to avoid spurious interactions with periodic images. For the hexagonal unit cell of pristine WSe_2, its optimized in-plane lattice constant is 3.32 Å and 24241 k-point samplings were used. A 55 supercell was then constructed to introduce a point Se vacancy to study the chemisorption of an O_2 molecule near the vacancy site. For the supercell, 661 k-point samplings were used. For all studied systems, all atoms were relaxed until the residual forces below 0.01 eV/Å, and the cut-off energy was set at 400 eV.

2.3 Atmospheric Effects

To elucidate the atmospheric and aging effects on WSe_2 multilayer devices, we performed a series of electrical tests in air and vacuum as a function of atmosphere exposure time. Five bottom gate devices were fabricated with a Cr/Au contact scheme on 10 layer (L), 9L, 7L, 4L, and 3L flakes. To distinguish the relative activation energy of adsorbed species, both short-term (20 minute) and long-term (48 hours) vacuum hold electrical measurements were performed. In what follows, we will first show atmospheric effects on as-fabricated devices. Subsequently, by distinguishing the electrical characteristics of the short-term and long-term vacuum pumping at specific aging times, we assign various physisorbed and chemisorbed species to the observed changes in the electrical characteristics. Figure 2.1a shows a set of transfer curves for a 7-layer FET measured in air, then held in vacuum for two-days and re-measured in vacuum, as a function of atmospheric exposure time. The device was measured the day it was fabricated (as-fab) then aged for 300 hours, about 13 days, and re-measured in air, vacuum, and additionally an N_2 environment. The device was then aged for an additional 600 hours, about 25 days, and re-measured in air and vacuum. The representative curves for other WSe_2 thicknesses can be found in 2.2. As will be described throughout this work, Figure 2.1b and 2.1c depict the schematic of as-fabricated devices in air and vacuum, respectively; changes in the electrical properties of the as-fabricated sample in atmosphere and after a short vacuum pump-down is attributed to H_2O physisorption on pristine WSe_2.

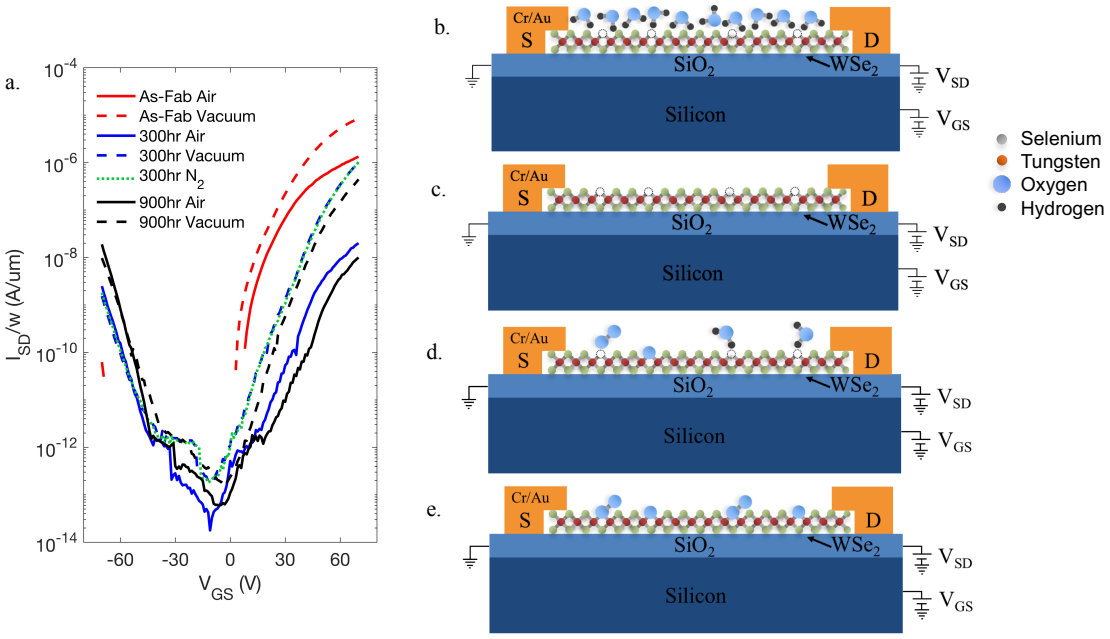

Figure 2.1: a. Transfer curves through aging in ambient (solid line) and vacuum (dashed line) environments. Schematics of devices in b. ambient as a new device c. vacuum as a new device d. vacuum as a mid-aged device and e. vacuum as a long term aged device

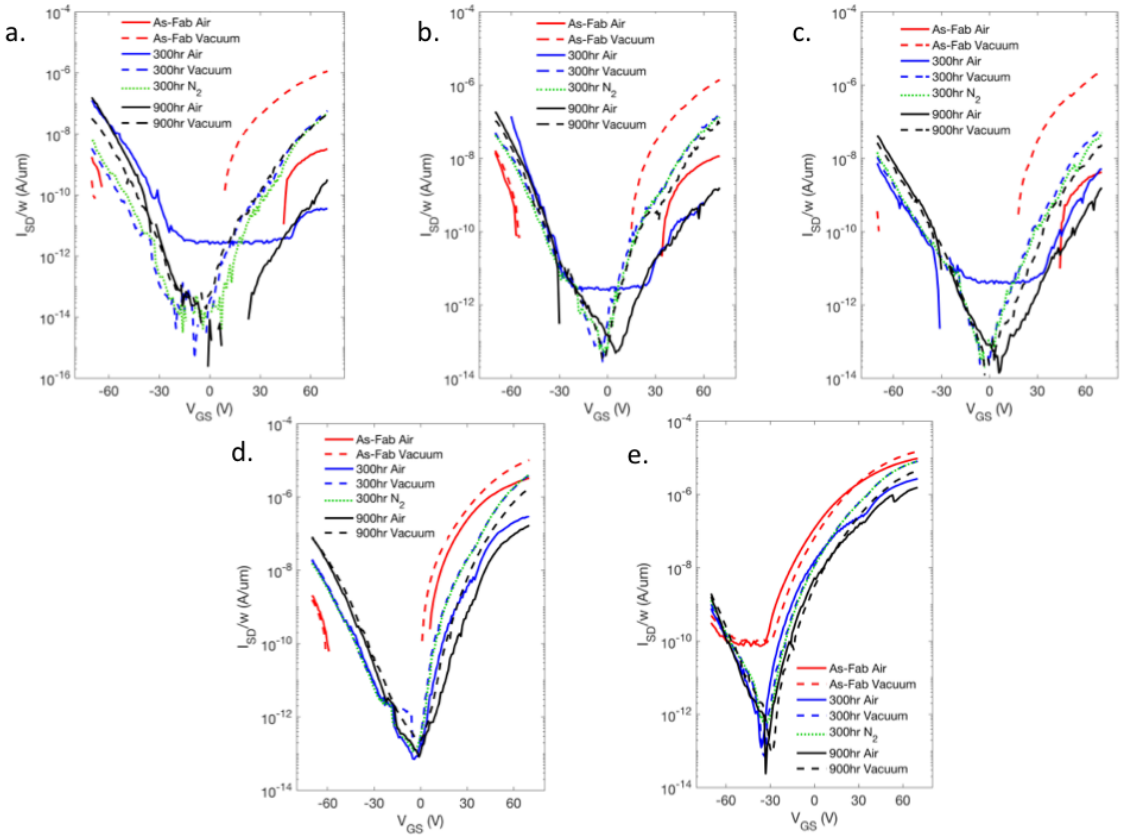

Figure 2.2: WSe2 transfer characteristics sensitive to ambient and aging times. I_{DS}-V_{GS} curves from (a) 3 layer (L) (b) secondary 3L (c) 4L (d) 9L and (e) 10L WSe2 FET in measured in air and vacuum for as-fabricated, 300 hours and 900 hours of atmospheric aging times. Additional measurement in inert N_2 environment for 300-hour aging time.

Figure 2.1d and 2.1e depict schematically the devices in vacuum after 900hr and 3600hr of atmospheric aging, respectively, illustrating how H_2O/O_2 physisorption on selenium vacancies dominates initially and chemisorbed molecular O_2 and atomic O at selenium vacancies dominate at longer aging times. The data shows that for all thicknesses and aging times, there is an increase in n-type conduction in vacuum compared to atmosphere. Furthermore, for the devices tested after 300 hours of aging, there is no significant change in the transfer characteristics when the pumped vacuum chamber is flushed with N_2 gas indicating this n-type conduction increase is not pressure dependent and not affected by N_2 adsorption. To observe the short-term conduction shift associated with physisorbed atmospheric gases, transfer measurements were taken on a pristine as-fabricated 3-layer device during a 20-minute pump-down cycle (2.3a) and venting cycle (2.3b) after the device was held in vacuum for two-days (see Methods for details and comprehensive electrical data set for additional flake thicknesses can be found in SI). The n-type conduction increases >200x during the 20-minute pump-down and reaches a stable value, which remains unchanged after a two-day exposure to vacuum. The n-type current reversibly decreases toward the original value when subsequently exposed to air for 20-minutes. The largest change occurs in the first 2 minutes of both cycles during which we were unable to collect data due to system vibrations, hence the large gap between the first and second curves in both Fig. 2.3a and Fig. 2.3b. The p-type conduction modestly decreases during pump-down and reversibly increases during venting. A plot of the ratio of on-current (at +/-70V gate voltage) measured after the two-day vacuum exposure, to the atmosphere measurement for n-type and p-type conduction, respectively, is plotted as a function of layer thickness in Figure 2.3c. It is clear that the environmental impact on n-type conduction has a strong thickness dependent while p-type conduction is minimally affected. The reversible, increase of n-type conduction upon exposure to vacuum suggests adsorbed molecules are modulating electron transport. Adsorbed surface molecules intuitively affect thinner materials more strongly due to their higher surface to volume ratio which is consistent with our observed layer dependence. DFT calculations by Wang *et al.* estimated that water molecules have the highest binding energy of atmospheric gases of about 45 meV on pristine WSe_2 and that physisorbed H_2O molecules act as an electron trap with a charge transfer of 0.0186 e^- per

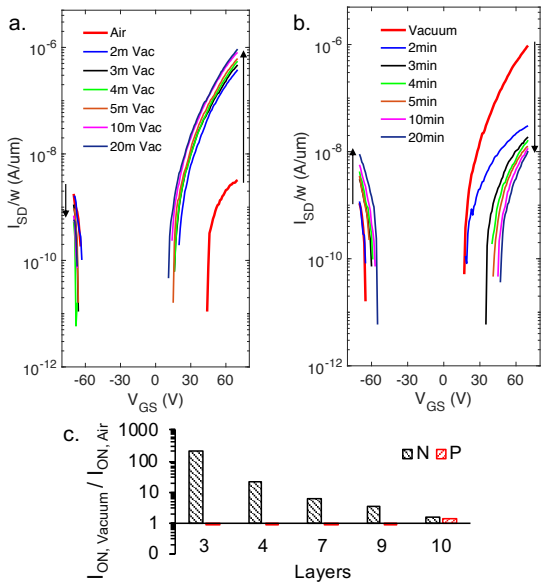

Figure 2.3: Transfer curves through aging in ambient (solid line) and vacuum (dashed line) environments. Schematics of devices in b. ambient as a new device c. vacuum as a new device d. vacuum as a mid-aged device and e. vacuum as a long term aged device

adsorbed H_2O molecule.[118] Thus, the observed n-type pressure dependent conduction is attributed to electron transfer from WSe_2 to physisorbed water molecules. Importantly, the binding energy of H_2O-WSe_2 is much lower than H_2O-stainless steel chamber ($\sim$ 1 eV)[119]; thus the coverage on the WSe_2 is dictated by the residual H_2O partial pressure, which after the initial volume of gas is pumped is limited by the desorption from the chamber walls. Similarly, Qiu *et al.* showed that the n-type conduction of bilayer MoS_2 increased by a factor of $\sim$ 10 in 10^{-6} Torr vacuum and increased another factor of 5 upon vacuum annealing at 350K. The vacuum annealing reduced the O1s XPS peak by approximately 43% and the observed increase in n-type conduction were attributed to either or both H_2O and O_2 adsorption.[107] More recently, Shimazu *et al.* studied the hysteresis behavior of MoS_2 devices under different atmospheres and noted that H_2O generated the largest hysteresis; though hole trapping was attributed to the approximately +28 V threshold voltage shift during the reverse sweep.[120] Finally, H_2O and O_2 adsorption has been shown to reversibly act as a photoluminescence gate modulator in n-type TMD materials; the photoluminescence modulation was attributed to the adsorbed species depleting the n-type carriers, which weakens electrostatic screening that would otherwise destabilize excitons.[121]

2.4 Aging Effects

In addition to the impact of adsorbed atmospheric molecules, various aging phenomena were observed. Figure 2.4a and 2.4b show the n-type and p-type on-currents at +/-70V gate bias, respectively, measured in air after over 900hrs of aging time in atmosphere (1200hrs for the 10L device). The conduction changes for both n-type and p-type over time are consistent with the effects of the adsorbed molecules, namely: with increasing aging time the n-type conduction decreases while p-type conduction increases. While adsorbed H_2O additionally affects the transport of aged devices, The ratio of aged to as-fab on-currents measured in atmosphere are plotted in Figure 2.4c, which shows the expected general trend that the long-term aging effects thinner flakes more, note exceptions to the data trends exist for instance the 3 layer n-type ratio and 4 layer p-type ratio.

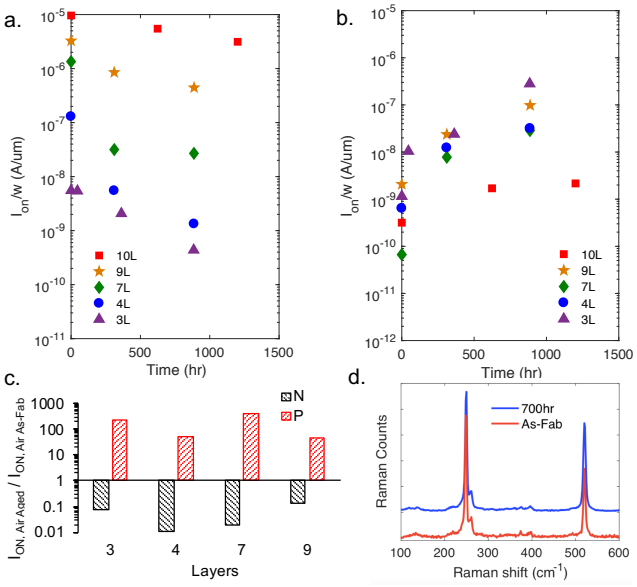

Figure 2.4: Long-term ambient aging effects. I_{ON} (I_{SD} @ +/-70 VGS) of (a) n-type and (b) p-type conduction in air for various-layered WSe_2 FETs as a function of atmospheric aging time. (c) Ratio of I_{ON} aged to as-fabricated for various layer thickness devices in air after 900 h of atmospheric aging. (d) Raman spectra of monolayer WSe_2 flake as-fabricated compared to the same monolayer flake after 700 h of atmospheric aging.

Furthermore, hole conduction increases more than electron conduction is suppressed. Figure 2.4d shows the normalized Raman spectrum of an exfoliated monolayer flake, which was measured immediately after exfoliation and after 700 hours of ambient aging. Figure 2.5 shows the raman spectra for 4, 7, 8, and 10 layer flakes. Significant degradation and disorder in TMDs can cause the Raman peaks to broaden, shift in position, and quench. [122][123] 40,41 Monolayers are particularly susceptible to these effects.In this study, there is no discernable shift in the Raman spectra for the monolayer or multilayer WSe_2 after aging, and there is no evidence of oxidation-induced changes. This is due to the thermodynamic mechanisms of aging in ambient, as described below, in which rather than crystalline tungsten oxide formation, H_2O/O_2 physisorption, and molecular O_2 and atomic O chemisorption, occur at chalcogen vacancies and therefore we did not observe WO_x in the Raman spectra.

2.4.1 Density Fictional Theory

To further elucidate the long-term aging effects on electrical properties of WSe_2, DFT simulations were performed similar to previous reports.[120][122] Figure 2.6 illustrates the electronic band structure of (a) single layer WSe_2 and (b) WSe_2 with a Se vacancy. Consistent with previous DFT calculations the Se vacancy introduces two almost degenerate gap states approximately 0.37 eV from the conduction band. A high concentration of Se vacancies will shift the Fermi level towards the conduction band rendering it n-type, which is common for many TMDs. Figure 2.6c shows the band structure of an O_2 molecule chemically adsorbed to the Se vacancy, which reflects that the dangling bonds are saturated; 1.37 e^- are transferred from the WSe_2 to the O_2 molecule and the adsorption energy has been calculated to be 2.36 eV.[124] The O_2 molecule can also be physically adsorbed above the Se vacancy with the adsorption energy of $\sim$0.24 eV (where about 0.26 e^- transferred from the WSe_2 to the O_2 molecule), and the barrier energy to be chemically adsorbed at the vacancy site has been calculated to be between 0.45-0.91 eV depending on calculation methods.[124] This energy barrier implies that the oxidation of the vacancy site is possible after long-term aging. In contrast, for the H_2O molecule, DFT simulations suggested that it can only be physically adsorbed above the Se vacancy site: only 0.05 e^- are transferred from the WSe_2 to the H_2O and the adsorption energy is about 0.3 eV.[125]

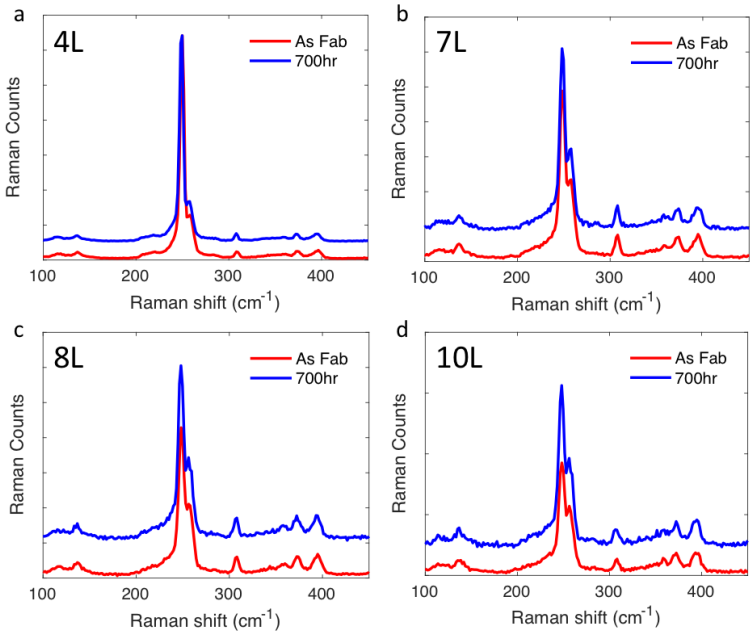

Figure 2.5: Raman spectra of (a) 4L (b) 7L (c) 8L and (d) 10L WSe_2 flake as-fabricated compared to the same monolayer flake after 700 hours of atmospheric aging. All flakes showed no significant shift in peak position.

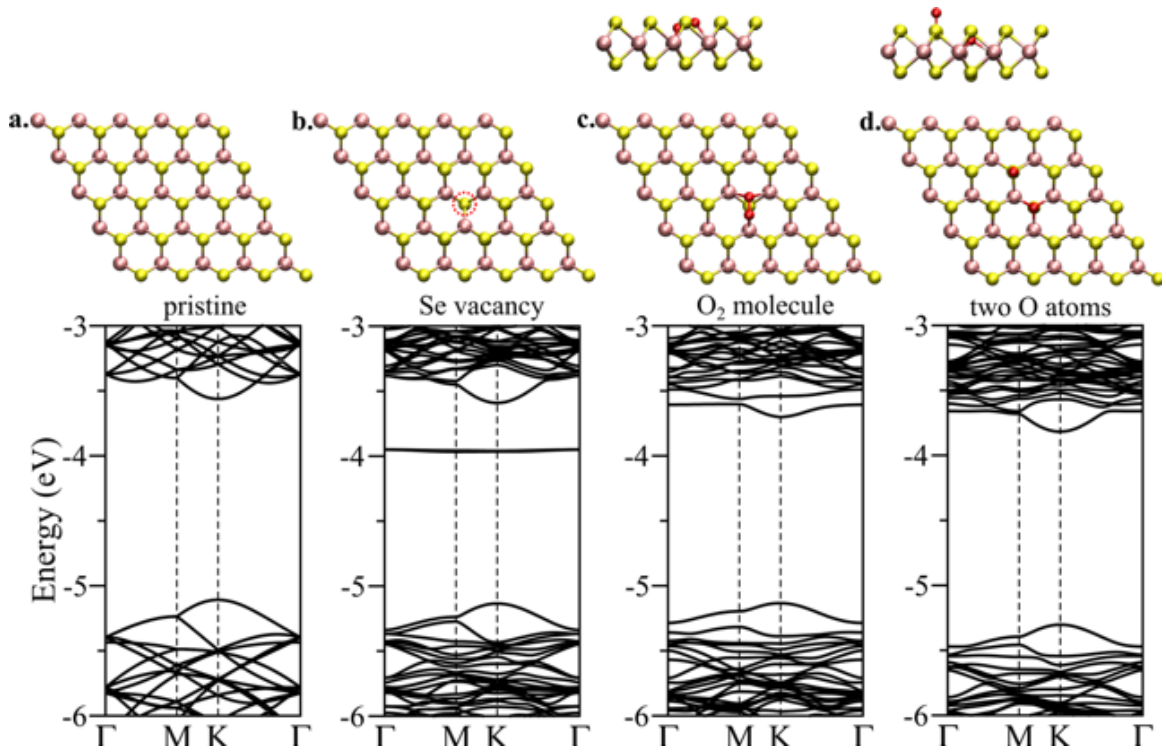

Figure 2.6: DFT calculated electronic band structures of the 55 supercell of WSe_2 monolayer with (a) no defect, (b) a single selenium vacancy, (c) molecular chemisorption of an O_2 molecule at the vacancy site, and (d) dissociative chemisorption of the O_2 molecule around the vacancy site. All band energies are aligned to the vacuum potential for direct comparison. The corresponding atomic structure (top and/or side view) is on top of the band structure.

Similar results for O_2 and H_2O adsorption were calculated for the S vacancy in defective MoS_2.[126][127] Finally, Figure 2.6d illustrates the band structure for a dissociated O_2 molecule where one O atom chemisorbs or isoelectronically fills the Se vacancy, and the other O atom adsorbs on a neighboring Se. This process has an about ∼0.58 eV activation barrier,[128] but when overcome, 1.99 e^- are transferred from WSe_2 and again the gap state is eliminated. Both the chemically adsorbed molecular O_2 and atomic O at the Se vacancy effectively eliminate the donor level associated with the Se vacancy and thus for both mechanisms in an extended material one would expect a progressive shift in the Fermi level towards mid-gap. Interestingly, our calculations also show a downshift in both the conduction band and valence band energy for the isoelectronic O substitution relative to the pristine WSe_2. Thus for this mechanism, a further increase in the work function is realized. Both mechanisms are difficult to confirm because doping level concentrations (<1%) of selenium vacancies is below the sensitivity limits of standard surface science techniques. Experimental studies of TMD surfaces and defects have helped elucidate the defect pictures that emerge for pristine and oxidized TMDs. However, doped WSe_2 materials studied with various surface science techniques, have revealed both p-type and n-type material associated with excess selenium[129][130][131] and selenium vacancies, respectively, and thus different materials preparation techniques and even variations on the same exfoliated flake can result in varying Fermi energy positions.[115]

2.4.2 Mid-Term Aging

Figure 2.7a and 2.7b are transfer characteristics for a vacuum pump-down and venting cycle for the 3L 300hr aged device,Figure 2.8a and 2.8b are transfer characteristics for a vacuum pump-down and venting cycle for the 3L 900hr aged device, which is the same device in Figure 2.3a and 2.3b. As described above, the aged device dominant carrier type in air has progressed from n-type to p-type. During an initial 20-minute pump-down, similar to the pristine device, the electron conduction increases significantly (30x), while the hole conduction is modestly decreased (2.5x). Thus it appears that the short-term H_2O adsorption on pristine WSe_2 with 45 meV binding energy affects the aged devices in a similar way as the pristine device with a characteristically short time constant (20-minute pump-down)

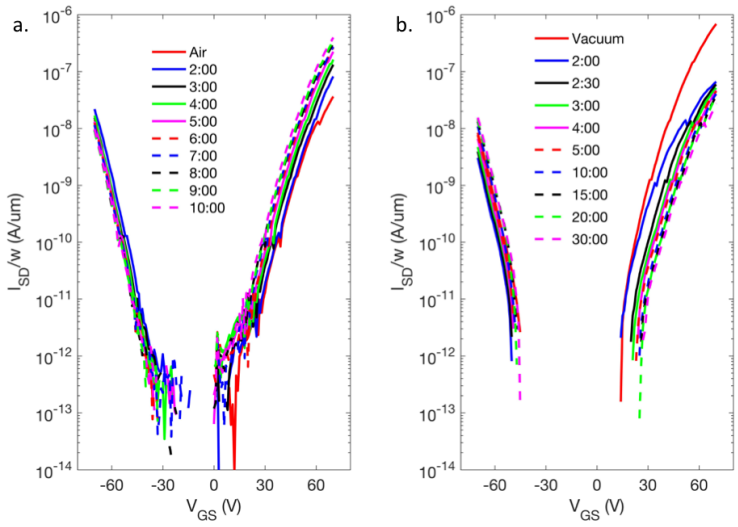

Figure 2.7: FET conduction shifts during pump down to vacuum and venting to air in a 300hr ambient aged device. (a) I_{SD}-V_{GS} curves for 7-layer WSe_2 FET during pump down through the first 10-minutes of pump-down. (b) I_{SD}-V_{GS} curves for 7 layer WSe_2 FET during venting through the first 30 minutes of venting.

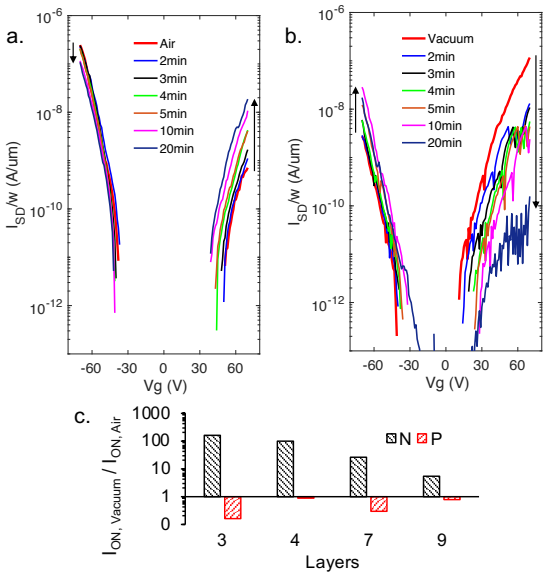

Figure 2.8: FET conduction shifts during pump down to vacuum and venting to air in 900 h aged device. (a) $I_{SD}V_{GS}$ curves for three- layered 900 h aged WSe_2 FET during pump down. (b) $I_{SD}V_{GS}$ curves for three-layered 900 h aged WSe_2 FET during venting after 2 days vacuum hold. (c) Ratio for various thicknesses 900 h aged devices of I_{ON} in vacuum after 2 days hold to I_{ON} in ambient.

associated with the physisorbed H_2O adsorption on the WSe_2 surface. Interestingly, after pumping for two-days, (Figure 2.8b, red), the electron current continues to increase and eventually exceeds the hole conduction as the cumulative electron on-current increases a factor of ∼150x, and the cumulative hole conduction decreases a factor of ∼100x. The 3L device measured as a function of air exposure time after a two-day pump-down reveals that the p-type conduction is only ∼5x higher and the n-type conduction is an order of magnitude lower compared to the as-fabricated device measured after a two-day pump-down. Thus the aging mechanism appears to have both a residual/permanent contribution as well as a reversible contribution, which diminishes over a longer pumping time. We attribute the long time constant reversible mechanism to physisorbed O_2 and H_2O at the selenium vacancies, which is consistent with the larger adsorption energies (0.24 and 0.30 eV, respectively) calculated by DFT.[125] We attribute the permanent aging component to the molecular O_2 or isoelectronic atomic O chemisorption at selenium vacancies, since chemisorbed O_2 molecules or O atoms are strongly bound (adsorption energies 2.36 eV). As can be seen in Figure 2.8c, the effect of the two-day pump-down decreases with increasing thickness, largely because both the short term and long-term aging have a progressively smaller effect with increasing thickness. The ratio of vacuum to air including the 10L device, which was aged for a different amount of time, can be found in 2.9a, additionally 2.9b shows the aging of each device at 900hr compared to the as-fabricated state. Field effect mobility calculated from V_{GS} [+/-] 65-70 for the 3L and 9L devices are listed in Table 1. The comparison between an as-fabricated device in air and an as-fabricated device in vacuum illustrates the effect of a physisorbed layer has on carrier mobility, while the comparison between an as-fabricated device in vacuum and an aged device in vacuum illustrates the effect of aging. Consistent with the transfer characteristics, the physisorbed layer does not have a large effect on p-type carriers, while n-type carrier mobility is significantly reduced. For the as-fabricated devices, the change in mobility, as expected, is thickness dependent: namely the 3L electron mobility increased a factor of ∼500 in vacuum, whereas the 9L only increased a factor of ∼4. Comparing the as-fabricated 3L versus aged 3L sample both measured in vacuum, the aged electron mobility decreased a factor of 20, whereas the hole mobility increased a factor of 16.

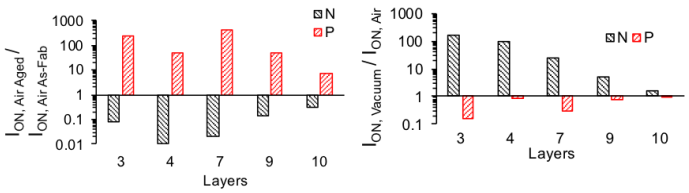

Figure 2.9: Ratio plot including the 10L device which was aged different than the 3-9L devices due to device fabrication occurring the week prior. (a) Ratio of Ion aged to as-fabricated for various layer thickness devices in air after 900 hours (3-9L) and 1200hr (10L) of atmospheric aging. (b) Ratio for various thickness 900-hour aged devices (3-9L) and 1200hr (10L) of ION in vacuum after two-day hold to ION in ambient. The addition of the 10L device illustrates continuation of the layer dependent trends.

2.4.3 Long-Term Aging

To investigate the long-term aging mechanisms more thoroughly we re-measured the 3-layer sample after 3600hrs of aging. Figure 2.10a illustrates the air and 20-minute pump-down transfer characteristics and 2.10b shows the two-day vacuum hold and subsequent 20-minute venting cycle. Relative to the 900-hour aged measurements, as expected, the air measurements reveal that the n-type on-current decreases another factor of 17x and the p-type conduction increases a factor of 2x. As illustrated in figure 2.10c, the short-term adsorption effects on the n-type (increase) and p-type (decrease) conduction are similar to the as-fabricated and 900-hour measurements. As shown in Figure 2.10d the ratio of the 20-minute to two-day n-type and p-type on-currents reveal an interesting trend. As discussed earlier, for the as-fabricated sample there is virtually no change in on-currents after the two-day pump-down; this is consistent with the fact that no long-term aging has occurred.

For both the 300hr and 900hr sample, the n-type and p-type currents both change significantly comparing the 20-minute and the two-day pump-down as can be seen in 2.11. This suggests that most of the aging at this point is due to H_2O/O_2-selenium vacancy physical adsorption, which decreases over the two-day pump-down and reveals a small residual/permanent contribution attributed to the atomic O or molecular O_2 chemisorption at selenium vacancies. At 3600hrs, the long-time constant contribution (H_2O/O_2-selenium vacancy physisorption) decreases, and the permanent high-binding energy chemisorption contribution not impacted by vacuum pump-down (isoelectronic O or molecular O_2 chemisorption of selenium vacancies) increases. Thus the picture emerges that physical adsorption initially dominates the aging, but at longer aging times these adsorption complexes either dissociatively react and O fills the Se vacancies or O_2 molecularly chemisorbs at the selenium vacancies.

Combined

The two effects talked about in this paper can be summarized by the on-currents in air versus vacuum over time as shown in 2.12. 2.12a shows that over time there is a consistent

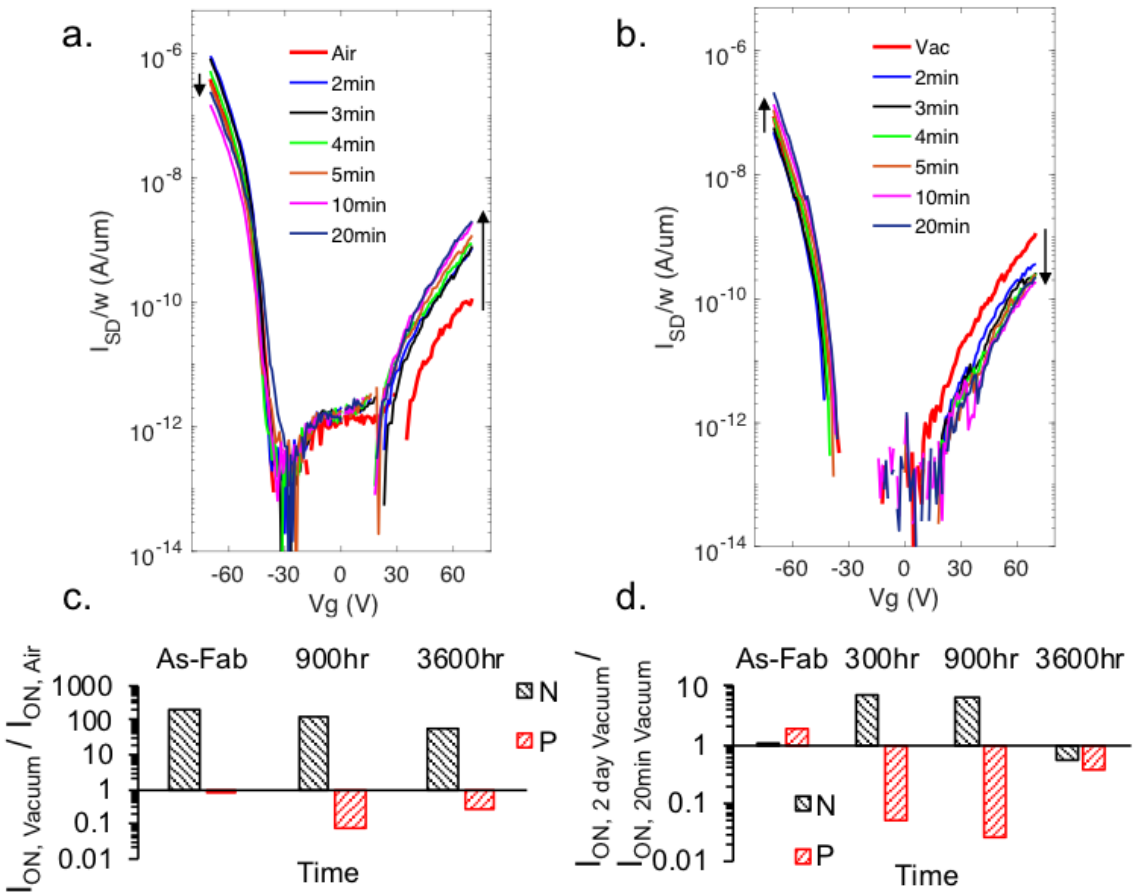

Figure 2.10: FET conduction shifts during pump down to vacuum and venting to air in 3600-hour aged device. (a) I_{SD}-V_{GS} curves for 3-layer 3600-hour aged WSe_2 FET during pump down. (b) I_{SD}-V_{GS} curves for 3-layer 3600-hour aged sample WSe_2 FET during venting after two-day vacuum hold. Ratio of (c) I_{ON} in vacuum after two-day hold to I_{ON} in air and (d) I_{ON} in vacuum after two-day hold to after 20-minute hold for 3L WSe_2 FET device at as-fabricated, 300hr atmospheric aged, 900-hour atmospheric aged, and 3600-hour atmospheric aging time.

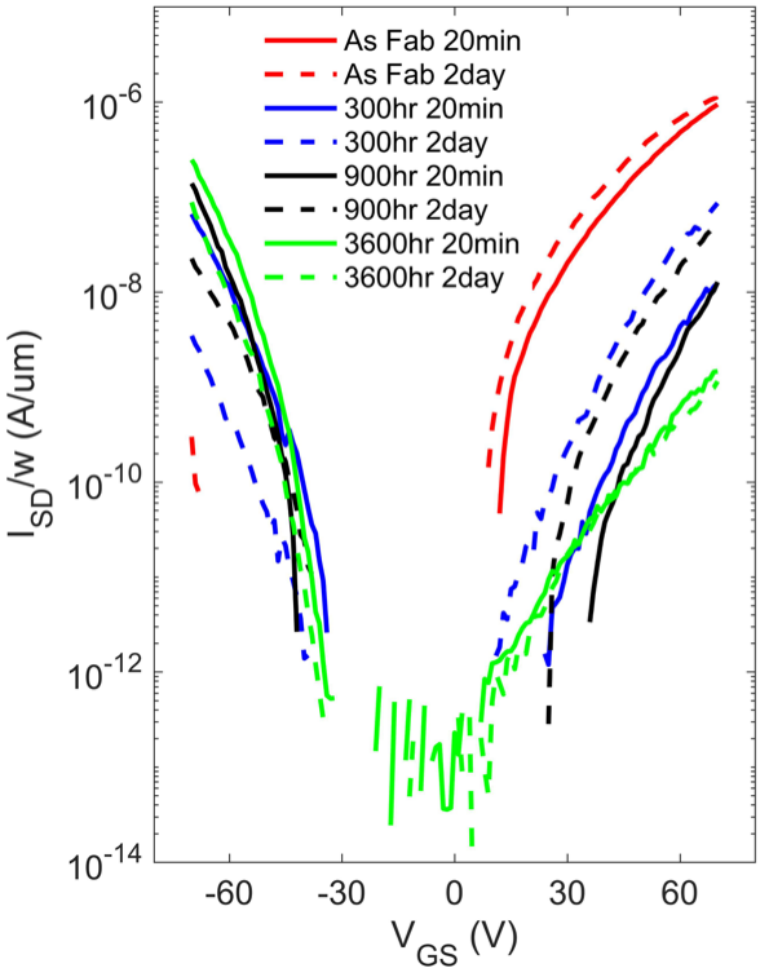

Figure 2.11: Conduction shift over the course of a 2-day vacuum hold. I_{SD}-V_{GS} curves for a 3L WSe_2 FET after 20 minutes in vacuum, then after 2 days in vacuum without venting at an as-fabricated, 300-hour ambient aged, 900-hour ambient aged, and 3600-hour ambient aged state. There is no shift in conduction in the as-fabricated state because only the weak physiosorbed molecules were affecting conduction. At 300-hour and 900-hour, there is a large shift over time due to adsorbents at selenium vacancies where they have a higher adsorption energy than on a pristine surface. At 3600-hour, conduction shift over time has reduced to minimal due to the vacancy adsorbents becoming chemisorbed at the vacancy and is thus permanent in vacuum.

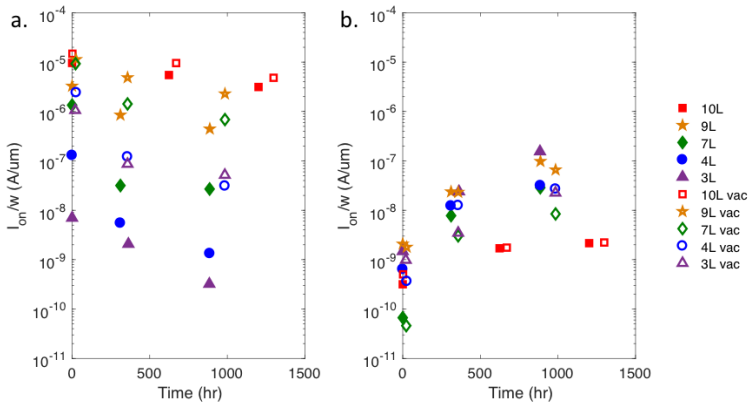

Figure 2.12: Long-term ambient aging effects. I_{ON} (I_{SD} @ +/- 70V_{GS}) of (a) n-type and (b) p-type conduction in air (solid markers) and vacuum (hollow markers) for various layer WSe2 FETs as a function of atmospheric aging time. The plot shows how n-type conduction increases in vacuum compared to air while p-type conduction decreases in vacuum compared to air.

increase in n-type conduction in vacuum as compared to air due to adsorbents with layer dependency indicating electron depletion from a set number of layers. The aging effect from isoelectronic oxygen is present in both air and vacuum n-type conduction with layer dependency since these defects are irreversible in vacuum and a surface effect. 2.12b shows there is a non significant change in p-type conduction in air versus vacuum and over time there is a layer independent increase in p-type conduction due to uniform p-type carrier doping.

2.4.4 X-ray Photoelectron Spectroscopy

To complement the electrical characterization results (albeit at different aging times), Figure 2.13 shows normalized XPS spectra of an exfoliated flake taken immediately after exfoliation, and after 500 hours and 2900 hours of atmospheric aging; for the 2900 hr aged sample we also re-measured the spectra after an overnight pump down. Note that the initial measurements for each sample was initiated on the order of 20 minutes to an hour after being introduced into the vacuum so the results are similar to the short vacuum pump down electrical results (20 minute). It can be seen from the W 4f core-level that there is no evidence of oxidation, which is consistent with the Raman analysis. We note that dopant level physisorption of H_2O/O_2 species would be below the level of detection of XPS. However, there was an observed 0.85 eV and 1.09 eV shift to lower binding energies for the 500 and 2900 hr aged samples, respectively. The W 4f7/2 peak shifted from 31.60 eV in the pristine sample to 30.75 eV and 30.51 eV in the aged samples, and the Se 3d5/2 peak shifted from 53.96 eV to 53.11 and 52.87 eV after aging. This identical shifts in both core-levels to lower binding energies is indicative of the Fermi level shifting closer to the valence band maximum, which is consistent with the decrease in n-type and an increase in p-type doping progressing from the pristine to 500 to 2900 hrs of atmospheric aging. Furthermore, the 2900 hr aged sample was pumped in ultra-high vacuum overnight and re-measured to confirm that the proposed high-binding energy O and O2 chemisorption is operative and the Fermi energy shift is stable as expected.

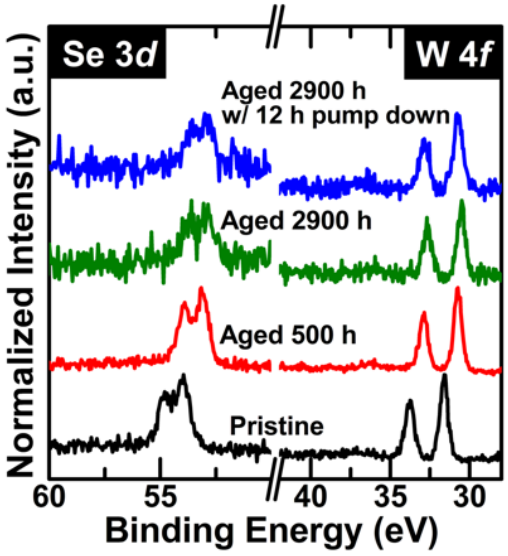

Figure 2.13: Se 3d and W 4f spectra of WSe_2 flakes on SiO_2 after mechanical exfoliation (pristine) and after atmospheric aging for approximately 500 and 2900 h. The 2900 h aged sample was also pumped overnight at 10^{-7} Pa and remeasured. Note that the 0.85 and 1.09 eV shift in the Fermi level toward the valence band for the 500 and 2900 h aged sample, respectively, consistent to the electrical results.

2.5 Conclusion

First, we demonstrate the impact that atmospheric physisorbed species have on the electrical properties of WSe_2 n-type and p-type conduction. Vacuum electrical measurements demonstrate a reversible change consistent with H_2O physisorption on the pristine WSe_2 (0.045 eV binding energy), which decreases the n-type conduction. Thinner devices have a larger change in the n-type conduction than thicker devices. Additionally, we demonstrate two atmospheric aging mechanisms associated with the selenium vacancies, namely: 1) H_2O/O_2 physisorption, and 2) molecular O_2 and isoelectronic O chemisorption. The H_2O/O_2 physical adsorption (0.3/0.24 eV binding energy, respectively) at selenium vacancies dominates at short aging times (900hrs) and is reversible at long pump-down times (two-days) and the molecular O_2 and isoelectronic O chemisorption dominates at longer aging times (3600hrs) and is permanent (2.36 eV binding energies). The latter chemisorption mechanisms passivate the selenium vacancies and cumulatively shift the Fermi energy toward mid gap and thus decreases the n-type conduction and increases p-type conduction. As expected the observed atmospheric and aging effects have a more pronounced effect on thinner flakes. This work illustrates the importance of understanding the electrical testing environment and the impact of atmospheric aging on TMD materials.

Chapter 3

O2 Plasma processed WSe2

A version of this chapter was originally published by Anna N. Hoffman, Michael G. Stanford, Maria Gabriela Sales, Cheng Zhang, Ilia N. Ivanov, Stephen J. McDonnell, David G. Mandrus, and Philip D. Rack: Hoffman, A. N., Stanford, M. G., Sales, M. G., Zhang, C., Ivanov, I. N., McDonnell, S. J., Mandrus, D.G., Rack, P.D. (2019). Tuning the electrical properties of WSe2 via O2 plasma oxidation: towards lateral homojunctions. 2D Materials, 6(4), 045024. Anna N. Hoffman conducted the device fabrication, electrical, and optical characterization, analysis and wrote the manuscript. Michael G. Stanford, Cheng Zhang, and Ilia N. Ivanov facilitated device fabrication training and helped with the electrical and Raman measurements; Maria Gabriela Sales and Stephen J. McDonnell performed XPS characterization. David G. Mandrus grew the WSe2 bulk crystals. The manuscript was written through contributions of all authors. The manuscript has been slightly modified to include the supplemental material.

3.1 Background

WSe_2 belongs to a class of materials called transition metal dichalcogenides (TMDs), which grow as layers bound together by weak forces with individual layer thickness less than a nanometer. Research on layered compounds, such as TMDs, boron nitride (BN), certain oxides, hydroxides and MXenes have become popular research materials after the demonstration of layered graphene in 2004. [1] Unlike graphene, many TMDs are semiconductors which possess a bandgap, which make them favorable for many electronic and optoelectronic applications. Many TMDs, such as WSe_2 have thickness dependent properties, which can be utilized to engineer electrical devices such as field-effect transistors (FETs) with specific properties; the most notable perhaps is the transition from an indirect band gap in the bulk to a direct band gap at the monolayer.[15] Carrier concentration and mobility are also layer dependent, which results in slight shifts in electrical behavior depending on the flake thickness.[18][132] Thus, when studying TMD properties it is important to study the behavior over a range of thicknesses; fortunately there are multiple characterization techniques that can reveal the specific layer number.

At room temperature, the photoluminescence (PL) spectra of monolayer WSe_2 has a dominant sharp peak centered around 1.65eV from the direct band gap A exciton transition. [89] [133] A peak at $\sim$ 400 meV higher in energy but much lower peak intensity (100x) is also observed associated with the B exciton originating from the spin-orbit split valence band. The A exciton PL peak intensity decreases $\sim$ 100x, broadens, and shifts $\sim$ 50 meV to lower energy as WSe_2 thickness varies from the monolayer to 3 layers. The higher energy B exciton also shifts concomitantly with the A exciton, which maintains the approximately 400 meV difference between these exciton energies. A second peak from the indirect band gap transition is evident in 2 layer flakes and has a peak at $\sim$ 1.5 eV; while the specific intensity can vary, its energy shifts to $\sim$ 1.4 eV at 3 layers. The Raman spectrum of a monolayer WSe_2 flake does not have the $B^{12}{}_g$ peak at 308 cm^{-1}, which is present in multilayer samples.[17] The $E^{12}{}_g$ peak at 250 cm^{-1} is a maximum in 2 layer flakes. Various TMD oxidation routes have been explored, mostly on MoS_2, including annealing in atmosphere, [122][134][135] ozone exposure,[43][60][111] and more recently by oxygen plasma treatments. [8][110][136] Depending on the process, TMD oxidation has been shown to be self-limiting to the top layer when performed at low temperatures ($\sim$ <100C).[43][60] Oxidation of a bi-layer WSe_2 revealed that the resultant WO_{3-x} layer is amorphous (a-WO_{3-x}) and that the a-WO_{3-x} layer hole-dopes the underlying WSe_2 layer.[43] XPS studies of a thin sputtered amorphous WO_3 layer on WSe_2 revealed the layer was n-type due to oxygen vacancies and has a high work function ($\sim$ 6.9 eV); thus a-WO_{3-x} is expected to be a good hole injection layer for WSe_2. Due to the amorphous structure of the oxide, it does not have a distinct Raman signature. Thus, the layer dependent indicators of WSe_2 described above have been utilized to determine progressive WSe_2 layer oxidation. WSe_2 flakes have a clear thickness dependent color shift from purple at the mono and few layers to blue and then highly reflective at bulk thickness.[66][132] Example photos with corresponding AFM scans can be found in Figure 1.3. A tungsten oxide monolayer is mostly transparent so optically, a pristine n-layer WSe_2 layer flake after single layer oxidation appears like a (n-1)-layer WSe_2 layer flake. However, Yamamoto *et al.* reported the overall flake thickness increased on the order of $\sim$2 nm after single layer oxidation due to ozone exposure.[43] This growth is due to transformation of the top single WSe_2 layer to amorphous WO_3, where the WO_3, layer is less dense and

thus thicker than a WSe_2 monolayer.[43][110][126] Thorough characterization of the WSe_2 oxidation has been previously performed via x-ray photoelectron spectroscopy, which can detect the reduction of W-Se bonding and the addition of W-O bonds via demonstrative W 4f peak shifts.[43][95]

3.2 Methods

3.2.1 Fabrication

WSe_2 flakes were mechanically exfoliated with tape onto Si/290 nm SiO_2 substrates, which acts as the back gate dielectric with the silicon wafer acting as the common back gate electrode. Flakes were identified and optically imaged with an optical microscope equipped with a Nikon digital camera. Devices were fabricated via electron beam lithography on samples spin-coated with Poly(methyl methacrylate) (PMMA) on an FEI 600 Nova equipped with a Raith lithography package. Source drain electrodes of 5 nm Cr, 25 nm Au were metalized in an electron beam evaporation tool at a rate of 1 Å/s at $2x10^{-6}$ Torr and lifted-off in acetone. Oxygen plasma exposures were performed in an RF oxygen plasma in an Oxford Atomic Layer Deposition tool. All flakes were exposed at 150° C, set to 150 W, 100 mTorr, 60 sccm and the exposure time varied from 5-60 s as specified in the main text. As illustrated in several figure inserts, the plasma treatments were exposed to a variety of WSe_2 geometries, namely: a) after metalization where only the channel region was exposed (Figure 3.1,3.10); b) prior to contact patterning, where the full flake was exposed prior to metalization (Figure 3.12); c) in the contact regions only where the channel layer was patterned with PMMA to protect the channel during exposure (Figure 3.12); d) p-n junctions were fabricated by patterning one electrode prior to an O_2 plasma exposure to the channel and other electrode region, with the subsequent electrode patterning step occurring after the plasma treatment (Figure 3.14).

3.2.2 Characterization

To characterize our plasma oxidation process initially 1, 2 and 3 layer flakes were exposed to a series of plasma exposure times and subsequently characterized via optical microscope, Raman spectroscopy and PL to determine oxidation rate. Raman and photoluminescence spectroscopy was performed on a Renishaw inVia micro-Raman system using a 532 nm excitation laser and a 100X objective. Atomic force microscopy (AFM) using an Asylum AFM was performed on a 3-layer WSe_2 flake as received and after a 15 s and 60 s plasma exposure. X-ray photoelectron spectroscopy (XPS) was measured on a molecular beam epitaxy (MBE) grown WSe_2 on highly oriented pyrolytic graphite (HOPG) samples in the as-grown, and after a 5 s (single layer oxidation) and 15 s (2-layer oxidation) O_2 plasma treatment; exfoliated flakes were attempted, however the flake density was not adequate for the XPS measurements. XPS data was collected using monochromatic Al K x-rays (1486.7 eV) at a pass energy of 26 eV in a PHI VersaProbe III UHV system, equipped with an auto dual-charge neutralizer. A spot size of $\sim$ 9 m was used. Spectral analysis was carried out using kolXPD software[115] to fit the features present in the W 4f and Se 3d spectra, and accurately determine peak positions. All peaks were fit with Voigt line shapes.

3.2.3 Exposure

FETs were fabricated from 6-15 layer WSe_2 flakes and exposed to an O_2 plasma in 5 second intervals up to 20 s, where only the WSe_2 channel region is exposed. Another set of devices on various chips were exposed to continuous plasma exposure times of 5, 15, or 25 seconds prior to lithography so the entire flake was exposed to the plasma. A third set of devices were exfoliated where the contact region was plasma exposed for 15 seconds prior to the metal contact deposition (channel region protected during a contact area plasma exposure). For the final set of devices, the first contact lithographically patterned, and the uncovered of the flake was exposed to a 15 seconds plasma exposure, then the final electrode was fabricated. Electrical characterization was performed in a cryogenic vacuum probe system with a 4200 Keithley semiconductor device analyzer and all the data presented here was pumped for a minimum of 20 minutes prior to measurement to minimize H2O adsorption effects.[137]

3.3 Discussion

3.3.1 Processing

Figure 3.1 illustrates the transfer characteristic progression of a 7 layer WSe_2 flake field effect transistor (FET) as a function of the cumulative O_2 plasma time exposed to the full channel region. O_2 plasma exposures on devices of additional thicknesses can be seen in Figure 3.2. Devices in this set exhibited uncharacteristically high as-fabricated p-type conduction. [137][93][12] This may be due to insufficient time in the vacuum as H2O adsorption will decrease the n-type conduction and increase the p-type conduction. [137] As illustrated in Figure 3.1c, with increased exposure, the n-type current systematically decreases >6 orders of magnitude with a cumulative exposure time of 20 s. Conversely, the p-type conduction increases a factor of 10. Both n-type and p-type threshold voltages also shift as noted in Figure 3.1b. Both n-type and p-type threshold voltages also shift as noted in Figure 3.1b.

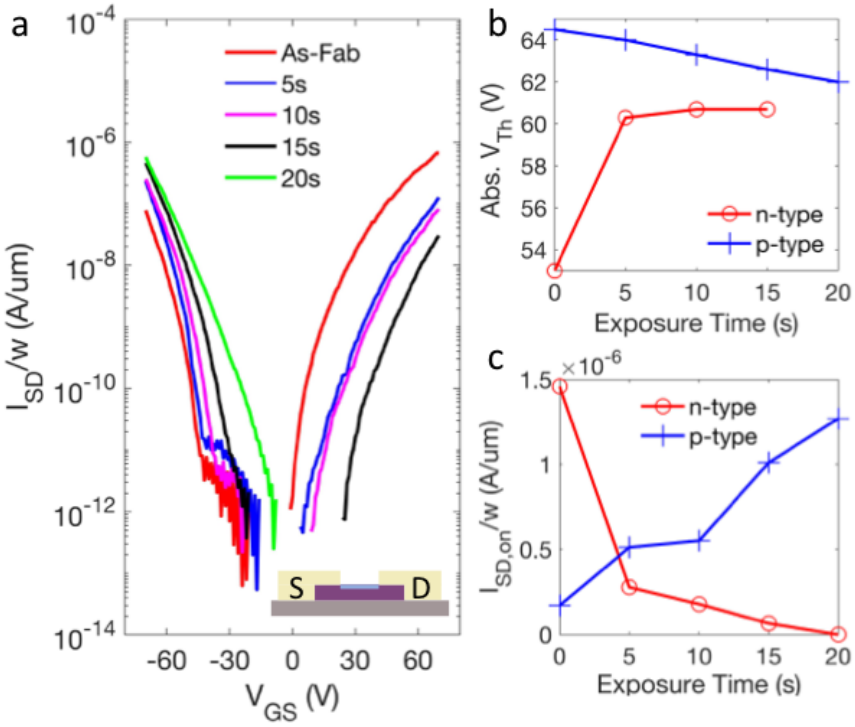

Figure 3.1: Transfer characteristics of a 7 layer device exposed to 5 s intervals of O_2 plasma (cumulative time denoted in the legend); (b) absolute value of threshold voltage as a function of O_2 plasma exposure time and (c) normalized source-drain current at +/-60 V as a function of O_2 plasma exposure

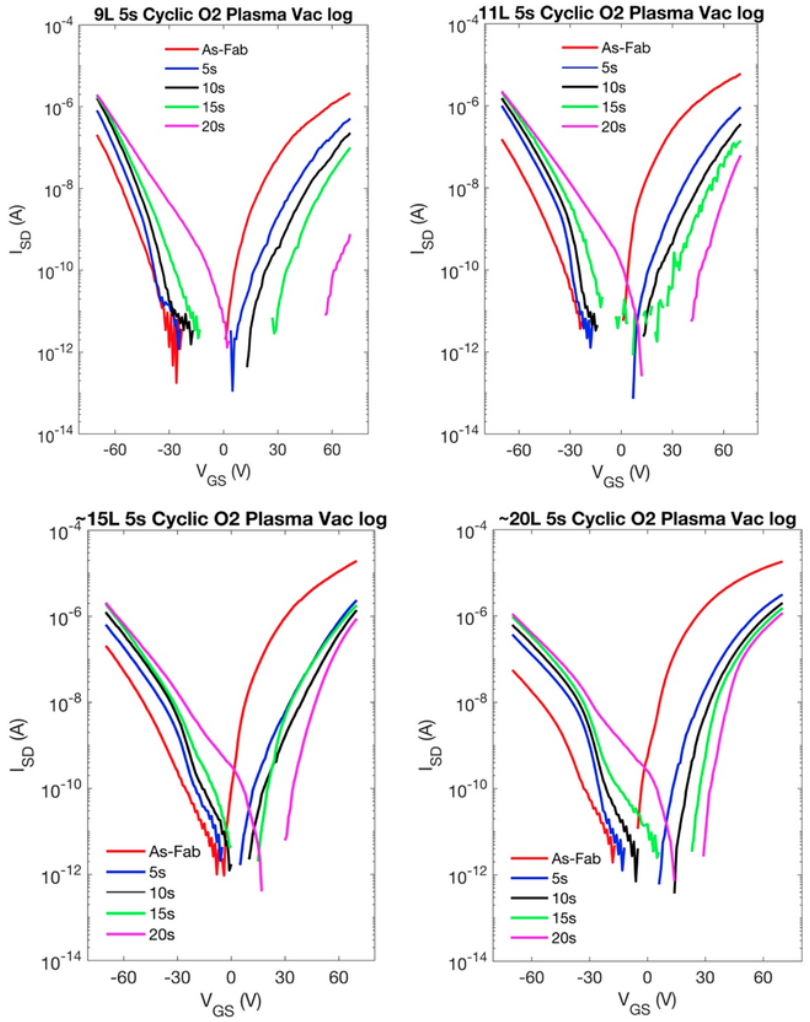

Figure 3.2: WSe_2 transfer characteristics of ∼20L, ∼15L, 11L, and 9L devices exposed to 5s cyclic periods of O_2 plasma to the full channel region after fabrication of contacts. Electrical impact of progressive oxidation is thickness dependent. Initial oxidation of the second layer is clear in devices 9 layers and thinner (7 layer device in main text) at 20s while devices 11 layers and thicker do not exhibit the same significant change in electrical behavior after 20s of exposure due to shielding.

These trends, are consistent with previous preliminary data done on channel layer plasma oxidation associated with plasma atomic layer deposition.[23] We hypothesize the effect of the oxidized single layer WO_{3-x} layer is the addition of a floating top gate, where fixed charge is accumulated in the WO_{3-x}. This is consistent with previous reports suggesting that WO_x is electrophyllic[60] and thus traps charge and induces a negative top gate.

3.3.2 Rate Study

To correlate the observed electrical changes, the rate of oxidation was determined through Raman and photoluminescence (PL) spectroscopy by tracking WSe_2 layer specific identifiers discussed in above. Optical imaging of the 3-layer flake, before and after successive plasma exposures, are presented in Figure 3.3a-e which show a slight color change suggesting the progressive oxidation of 1 and 2 layers of WSe_2. The Raman maps and spectra show very clear transition to 2 layers after just 5 seconds of O_2 plasma exposure by the increase in the E^1_{2g} peak while the B^1_{2g} peak is approximately unchanged. 2 layers of WSe_2 remain after a total of 10 seconds of exposure, while the oxidation of the second WSe_2 layer begins after a combined exposure time of 30 seconds of O_2 plasma as evidenced by the reduction of both the E^1_{2g} and B^1_{2g} peak. Due to the amorphous structure of the oxide, the resultant WO_3layer does not have a distinct Raman signature, which is consistent with. [138] Expanded Raman spectra illustrated in the Figure 3.4 and Figure 3.5, for a 2 layer and 3 layer exposed flake respectively, do not have the representative peaks of WO_3at $\sim$ 712 and 802 cm^{-1}. [17] [139] At 60 seconds of total plasma exposure the B^1_{2g} peak is gone indicating only a single layer of WSe_2 remains. The PL spectra for the 1 layer, 2 layer and 3 layer as a function of oxidation time in Figure 3.3q also confirms the progressive oxidation of 1 layer after 15 s and 2 layers after 60 s. Consistent with what was described above, the 3 layer as-grown spectrum consists of an $\sim$10x lower direct band gap peak that is slightly shifted to lower energy (1.6 eV) and also has the indirect bandgap peak at $\sim$ 1.42 eV. The peak at $\sim$1.5 eV is consistent with the 2 layer indirect bandgap position, thus this exfoliated flake could have regions of 2 layer WSe_2. After the 60 s exposure, the PL peak shifts to $\sim$1.62 eV, which is consistent with the A exciton direct band gap transition; the peak is broader and the presence of the oxide layers on top causes a slight redshift of this peak which is typically at 1.65 eV.

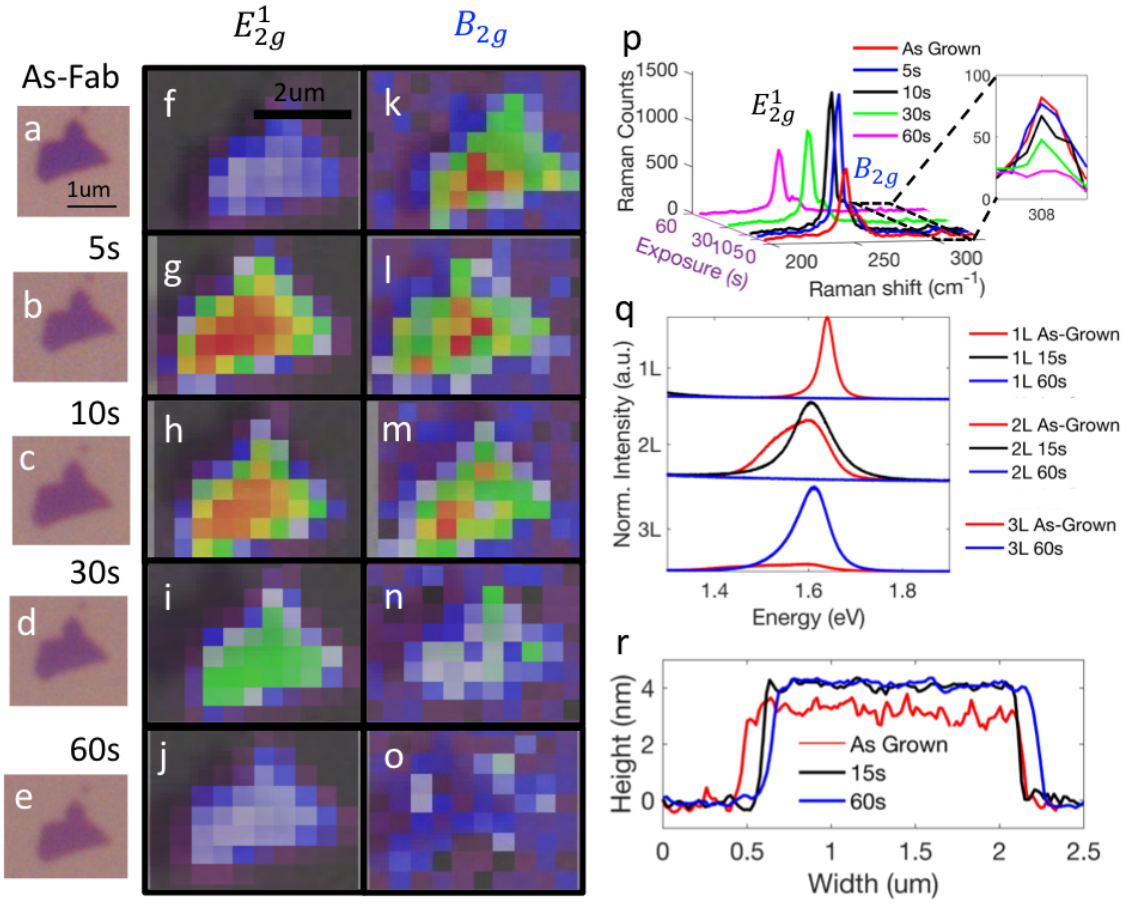

Figure 3.3: Study of WSe_2 flakes as a function of increasing O_2 plasma exposure. Optical 100x objective images of 3 layer flake (a-e), Raman map of $E^{12}{}_g$ peak (f-j) and $B^{12}{}_g$ peak (k-o) as a function of increasing oxygen exposure. Raman spectra of a 3 layer flake at each exposure time (p), PL spectra of a 1 layer, 2 layer, and 3 layer flake as a function of O_2 plasma exposure (q) and AFM scan of 3L flake as a function of O_2 plasma exposure (r).

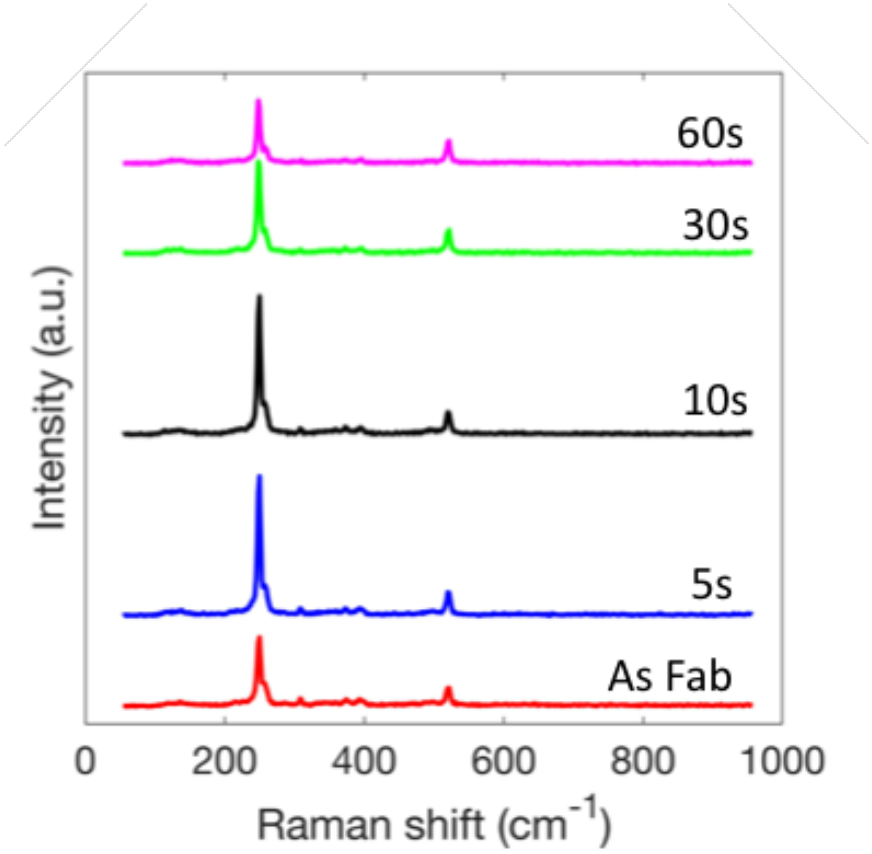

Figure 3.4: Full Raman Spectra of exfoliated WSe_2 2 layer as a function of O2 plasma exposure time.

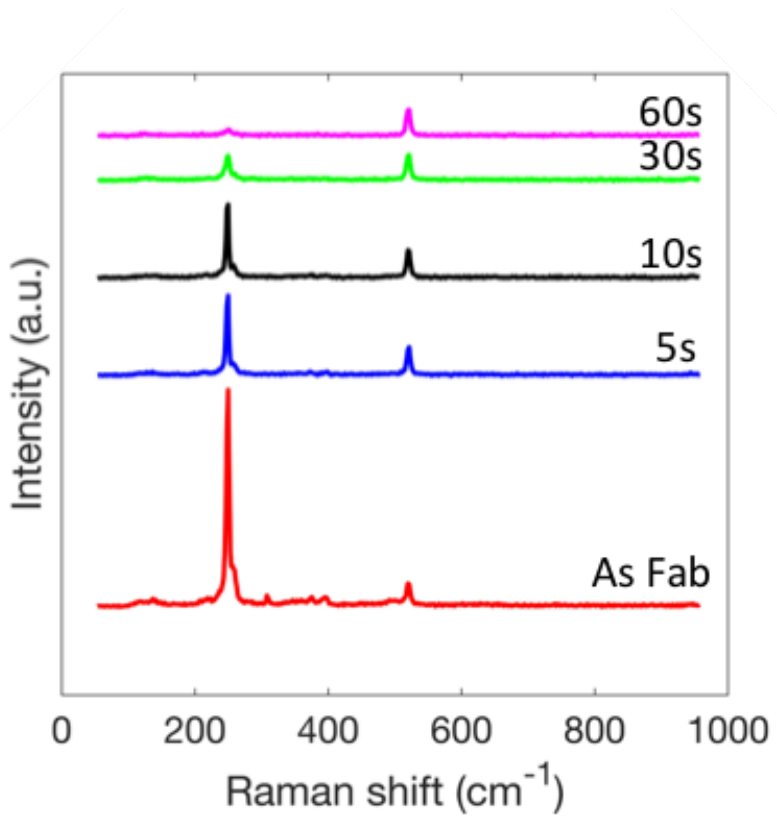

Figure 3.5: Full Raman Spectra of exfoliated WSe_2 3 layer as a function of O2 plasma exposure time.

Previous work reports a redshift occurs with electron doping, however a study on the oxidation of WSe_2 reports a similar redshift resulting from hole doping.[43] The PL spectra of the 2 layer exfoliated flake also confirms the progressive oxidation. Namely, the as-grown 2 layer spectrum has peaks attributable to the direct and indirect band gap at ∼1.5 And 1.62 eV, respectively. After the 15 s O_2 plasma exposure, the spectrum is consistent with the single layer direct band gap position of ∼1.62 eV. After 60 seconds, the PL spectrum disappears as the second layer is oxidized. Finally, for the single layer WSe_2 exfoliated flake, the as-grown peak PL spectrum has a single peak associated with the direct band gap A exciton at 1.65 eV. Subsequent exposure to 15 and 60 seconds results in a total quenching of the WSe_2 as the single layer is oxidized. Complementary oxidation studies illustrating Raman and PL for exfoliated 2 layer and monolayer flakes is shown in Figure 3.6. As described above, the WO_{3-x}formed by the plasma is suspected to be amorphous, and thus we detect no Raman peaks other than from Si and WSe_2. While peaks for hexagonal and monoclinic tungsten oxide have been reported at (712 and 812 cm^{-1}) [17] tungsten oxide formed from XeF_2 etching also exhibits no discernible Raman peaks. [138] AFM scans of an exfoliated 3-layer flake measured before and after a 15 s and an additional 45 s plasma exposure are shown in Figure 3.3r. Consistent with previous results of WSe_2 oxidation studies, the thickness increases,[43] however, we find a height increase of only ∼1 nm after the corresponding single layer oxidation and no further height increase after an additional 45 s exposure i.e. double layer oxidation. This difference in height from previous studies may be due to varying oxidation processes. As demonstrated by the XPS results below, our WO_x layer is has a value $x<3$; thus our sub-stoichiometric is thinner and perhaps our film is more dense relative to the ozone oxidation process.[43]

3.3.3 XPS

To confirm the oxidation kinetics from the Raman study, XPS was performed on a pristine and 5s O_2 plasma exposed samples. While exfoliated flakes were attempted, the flake size and areal density was not adequate. Consequently, MBE grown 3-layer samples were grown on HOPG for the XPS studies in a UHV system described elsewhere.[140]

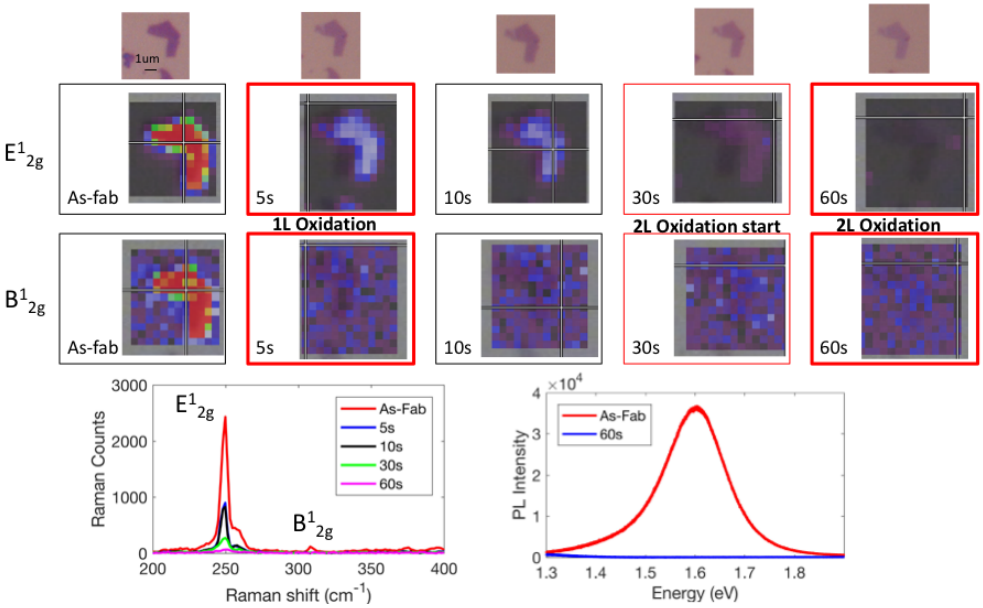

(a) 2 Layer

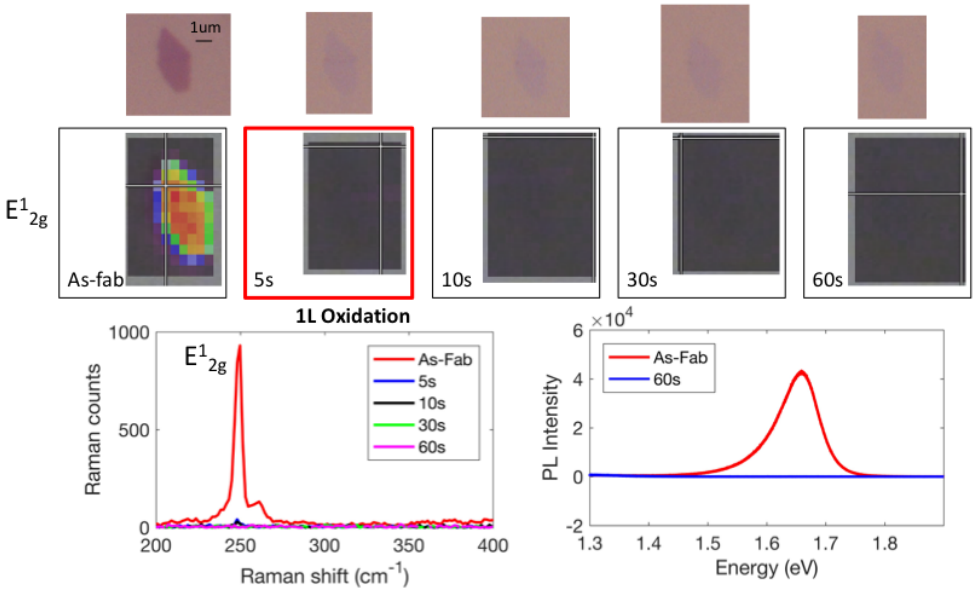

(b) 1 Layer

Figure 3.6: Raman map and PL study of 2L and 1L. Oxidation of the first layer is clear after just 5s of O_2 plasma exposure. Similar to the electrical cyclic results, the second layer begins to oxidize after 30 seconds of O_2 plasma with 2 layers completely oxidized after 60s of exposure.

The oxidation kinetics are much faster in the MBE grown samples compared to exfoliated single crystal flakes; for instance, oxidation of two layers was observed after a 5s O_2 plasma exposure based on the Raman and PL spectrum shown in supporting info Fig 3.7. Consistent with previous literature, [82][43][60][8] Figure 3.8 shows XPS spectra of samples after a) 5 s and b) 15 s plasma exposure as well as c) a sample exposed to atmosphere for a week to emulate the time between the successive XPS measurements. The spectra reveal significant oxidation from plasma treatment not seen in the similar aged, untreated sample. While curve fittings of each spectra, shown in Figure 3.9 show a slight increase in the proportion of $W^{4+}(WO_2)$ oxide bonding compared to W^{6+} (WO_3) with increased plasma exposure, both W-oxide peak fractions increase with increasing plasma exposure.

3.3.4 Exposure Geometry

For some architectures, sequential/interval exposures are not an option, so it was necessary to determine an optimal continuous exposure time to compensate for the brief plasma ignition times that can accumulate for several iterations. Figure 3.10 plots the transfer characteristics of various layered FETs (4a) as-fabricated, and after continuous plasma exposures of (4b) 15 s and (4c) 60s. Based on Raman and PL results, 15 s of continuous exposure oxidizes the top layer of the WSe_2 and oxidation of the second layer is initiated. For 60 seconds of continuous O_2 plasma exposure the second layer is fully oxidized. All as-fabricated devices show the expected n-type behavior with increased on-current in thicker flakes. The n-type suppression by O_2 plasma exposure on the channel is, as expected, layer dependent as shown in Fig 3.10b. After 15 seconds of continuous plasma exposure the 6 layer and 7 layer flakes show total n-type suppression, while the n-type conduction in the 11 layer and 15 layer flakes were minimally suppressed. Figure 3.10d) plots the calculated threshold voltages for the 15 and 60 s exposures and Figure 3.10e) plots the +/- 60V on-currents. All flake thicknesses show a large increase in p-type conduction resulting in thicker devices behaving ambipolar with near equal n- and p-type conduction at the maximum +/- gate voltage, and 9 layer devices and thinner behaving as p-type devices. P-type conduction does not show a significant layer dependence, each flake yielded a normalized p-type conduction maximum of $\sim 10^{-6}$ A/μm after the 15 second O_2 exposure.

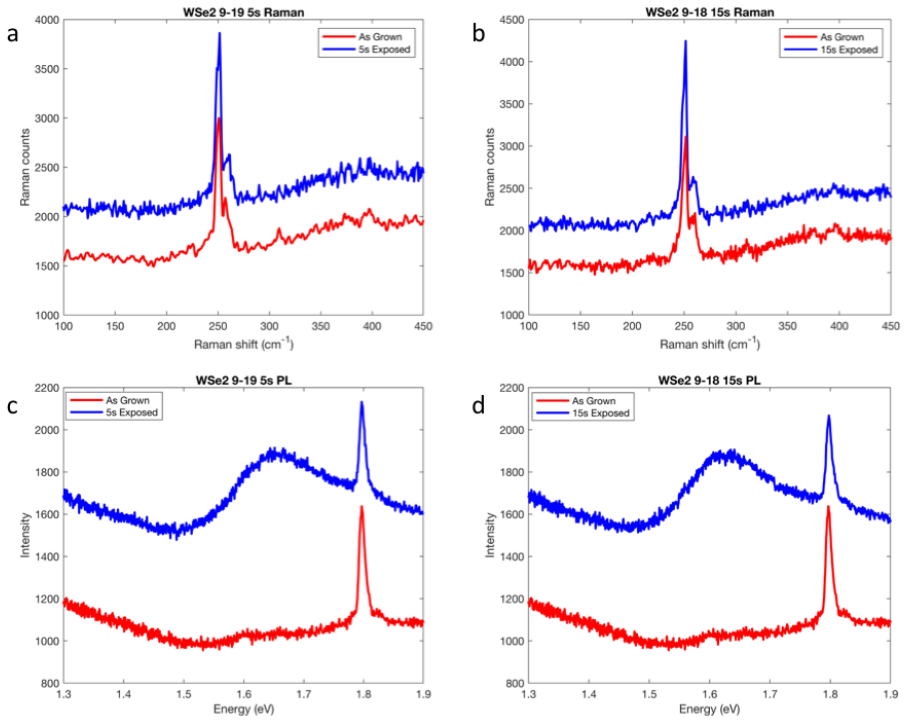

Figure 3.7: Raman (top row) and PL (bottom row) of MBE grown WSe_2 samples. Left column was exposed to 5s of O_2 plasma, right column exposed to 15s of O_2 plasma. Samples as grown were 3 layers. After both 5s and 15s of exposure the $B^{12}{}_g$ peak at 308cm^{-1} disappears indicating only on2 layer of WSe_2 is left and the top two layers had oxidized. PL after oxidation supports raman, a single peak at $\sim$1.62.

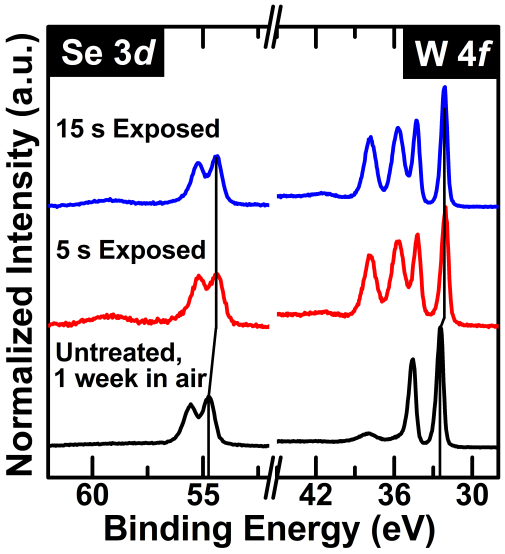

Figure 3.8: X-ray photoelectron spectra of MBE grown WSe_2. The three spectra characterize as grown, 5s, and 15s O_2 plasma treated samples.

W 4*f* region

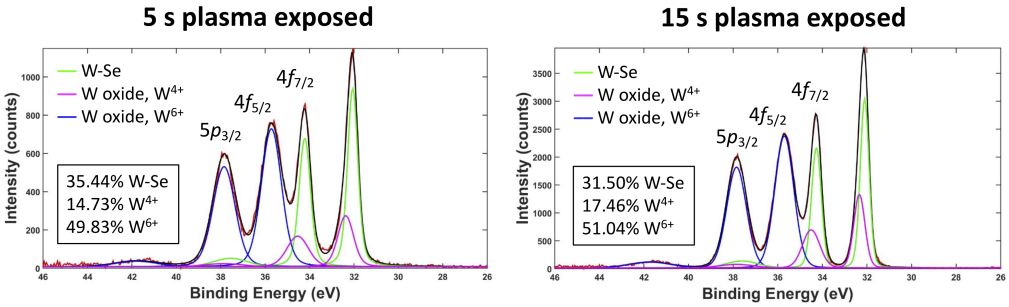

Figure 3.9: Curve fit of XPS data. Both W-O bonding peaks increase from 5s to 15s of exposure indicating a higher amount of oxide compared to WSe_2. Additionally, the ratio of W^{4+} to W^{6+} increases indicating with more exposure the overall stoichiometry of the oxide is shifting from WO_3 toward WO_2

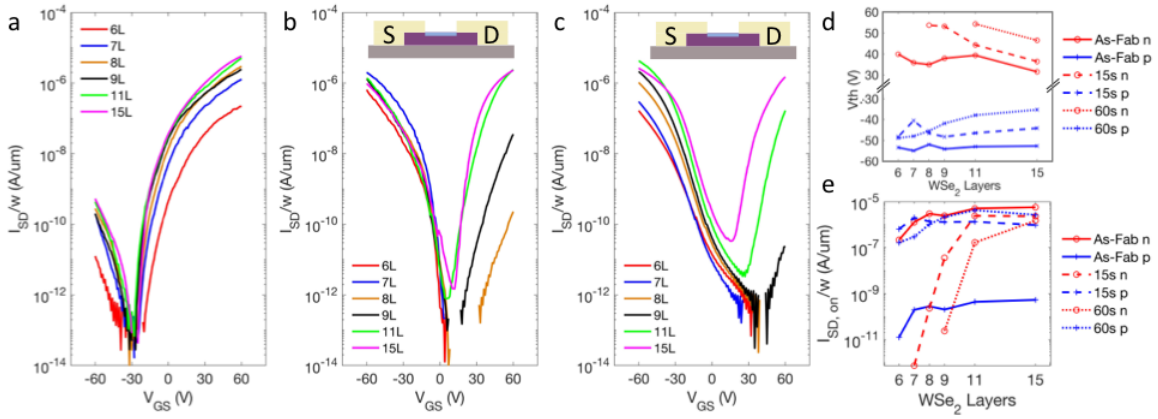

Figure 3.10: WSe_2 Layer-dependent O_2 plasma exposure study. (a) As-fabricated transfer curves for 6 layer, 7 layer, 8 layer, 9 layer, 11 layer, and 15 layer WSe_2 devices (b) transfer curves of same devices after 15s O_2 plasma exposure on the channel (c) and after 60s O_2 plasma exposure.

As mentioned above, the WO_{3-x} layer appears to contain a fixed negative charge density, which shifts the threshold voltage. Calculated threshold voltages for each set of devices and the I_{SD} at +/-V_G=60 V are listed in Figure 3.11. Thus the n-type conduction decreases and the p-type conduction increases. After 60s of exposure, n-type behavior of all devices is further suppressed, the 8 layer device is no longer n-type conducting. Additionally, we see some p-type suppression in the thinner flakes suggesting the exposure has started to cause damage to these flakes reducing overall conduction. Thus, the optimal O_2 exposure time for the thinner exfoliated flakes in particular is 15 s of O_2 plasma.

3.3.5 pn junction

Figure 3.3a illustrates the transfer characteristics for various flake thickness where a plasma exposure was performed in the electrode region to enhance the hole injection properties of a transition oxide contact layer, as WO_{3-x} is reported to have a high electron affinity and ionization potential. [43][95] The contact region was lithographically patterned and prior to metal deposition the sample was exposed to s 15 second O_2 plasma treatment. Comparing an as-fabricated (Figure 3.10a) and contact region exposed sample, there is very little effect on n-type conduction and the threshold voltage remains relatively unchanged as listed in Figure 3.11. As expected, there is an enhancement of p-type conduction by approximately 2 orders of magnitude. Full flake exposure devices were fabricated by oxidizing samples prior to any lithography. Transfer characteristics after a 15s exposure to the entire flake as a function of the layer thickness is illustrated in figure 3.12b. The electrical results of this geometry does not have the expected p-type conduction consistent with the other exposure geometries. We speculate that the continuous WO_{3-x} layer is n-type due to oxygen vacancies and thus in contrast to the channel-only exposures where the WO_{3-x} layer floats and accumulates charge, a continuous path from source-to-drain exists in these devices. The parallel conduction path through the WO_{3-x} layer exists which apparently has a lower threshold voltage; for instance we note that there is an $\sim$ 2-4 order of magnitude increase in the -30 V gate bias conduction compared to the full channel exposure devices.

	P-type				
		elec		full	
	As Fab	15s		15s	
Layer	Vth	Vth	dV	Vth	dV
6	-53.4	-55.1	-1.7		
7	-54.9	-55.1	-0.2		
9	-54.1	-53.0	1.1		
11	-53.0	-55.0	-2.0		
15	-52.7	-53.4	-0.7	-53.9	-1.2

(a) caption

	N-type				
		elec		full	
	As Fab	15s		15s	
Layer	Vth	Vth	dV	Vth	dV
6	39.9	48.3	8.4	34.5	-5.4
7	35.8	46.5	10.7	36.2	0.4
9	37.9	44	6.1	35.5	-2.4
11	39.3	40.8	1.5	36.9	-2.4
15	31.5	36.8	5.3	27.3	-4.2

(b) Caption

Figure 3.11: Threshold voltage of 15s electrode region and full flake exposed devices

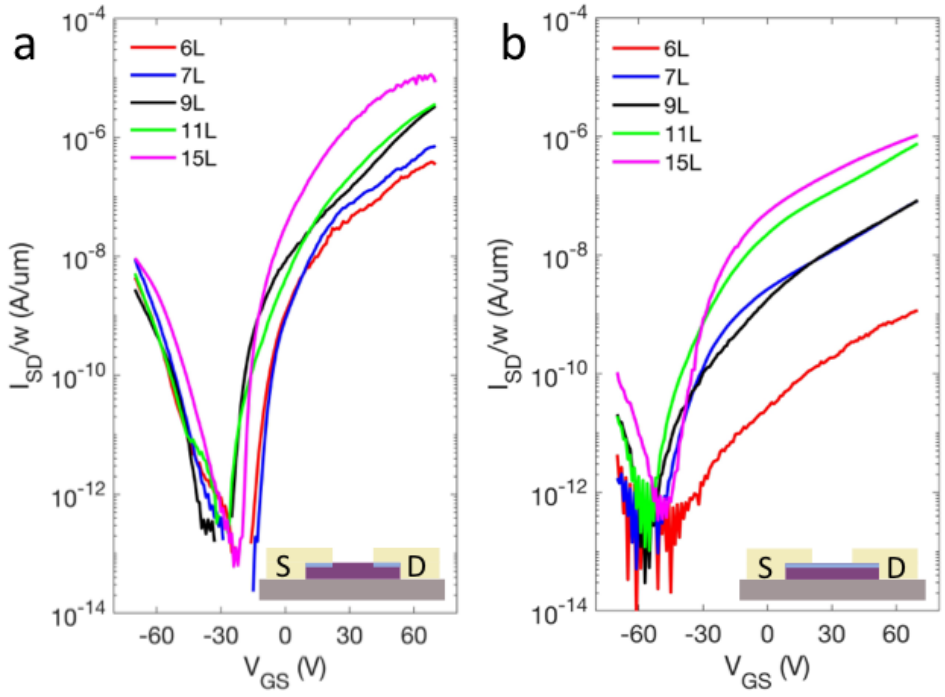

Figure 3.12: Transfer curves of various thickness WSe_2 flakes exposed to 15 s O_2 plasma. (a) Only the contact metalization regions are exposed [channel region masked] and (b) the entire flake is exposed [both channel and contact metalization region are exposed].

The maximum n-type on-current in the n-layer devices is similar to n-1 layer on-currents in figure 3.10a, which suggests at higher positive gate voltage the n-type characteristics follow WSe_2 layer dependence where 1 layer has been converted to the WO_{3-x}. Based on the results, we surmised that p-n junctions could be formed via various plasma exposure geometries. While the optimum geometry was anticipated to be a device where one half of the flake was plasma exposed (electrode and channel region), very little rectification was observed in this device which can be seen in Figure 3.13. Subsequently, we explored a geometry where the plasma was exposed to the entire channel and under one electrode. The fabrication process of this back gated p-n junction is illustrated in Fig 3.14a-h, where the first electrode is patterned and deposited on an exfoliated flake and then device is exposed to oxygen plasma for 15 seconds. The second electrode is then patterned on top of the oxide layer. The electrode on the as-exfoliated WSe_2 serves as the p-type side of the junction as this contact region allows hole injection and the oxidized channel region supports the hole conduction. The oxide layer/contact region blocks hole injection and allows electron injection, however the oxidized channel region depletes electrons, thus the junction forms at the oxide layer contact region noted in Figure 3.14h. This device was fabricated with flakes of various thicknesses from 3 to 20 layers thick. Conduction was suppressed below 8 layers and relatively unaffected above 14 layers. Additional devices from flakes other than the 11 layer can seen in Figure 3.15. All devices showed various levels of rectification in transfer characteristics when source drain voltage was reversed, shown in Figure 3.14i. Figure 3.14j demonstrates the output curve at V_{GS} = -20V for the 11 layer device. In forward bias, when the n-type contact on the oxide layer acts as the source and the p-type contact acts as the drain, conduction reaches an on-current of 10^{-8} A while in reverse bias current is restricted to 7-11 A. This effect is clearly displayed in Figure 3.14j by the output curve of this 11 layer device held at a constant -20V gate bias and swept through source-drain bias from -2V to 2V. The rectifying ratio of this device at this gate voltage is $\sim$330. The ratio of other mid range flake thicknesses at various gate voltages is plotted in Figure 3.14k along with the on-current at that point on the second x-axis. Rectification ratio of all devices fabricated are plotted in Figure 3.16.

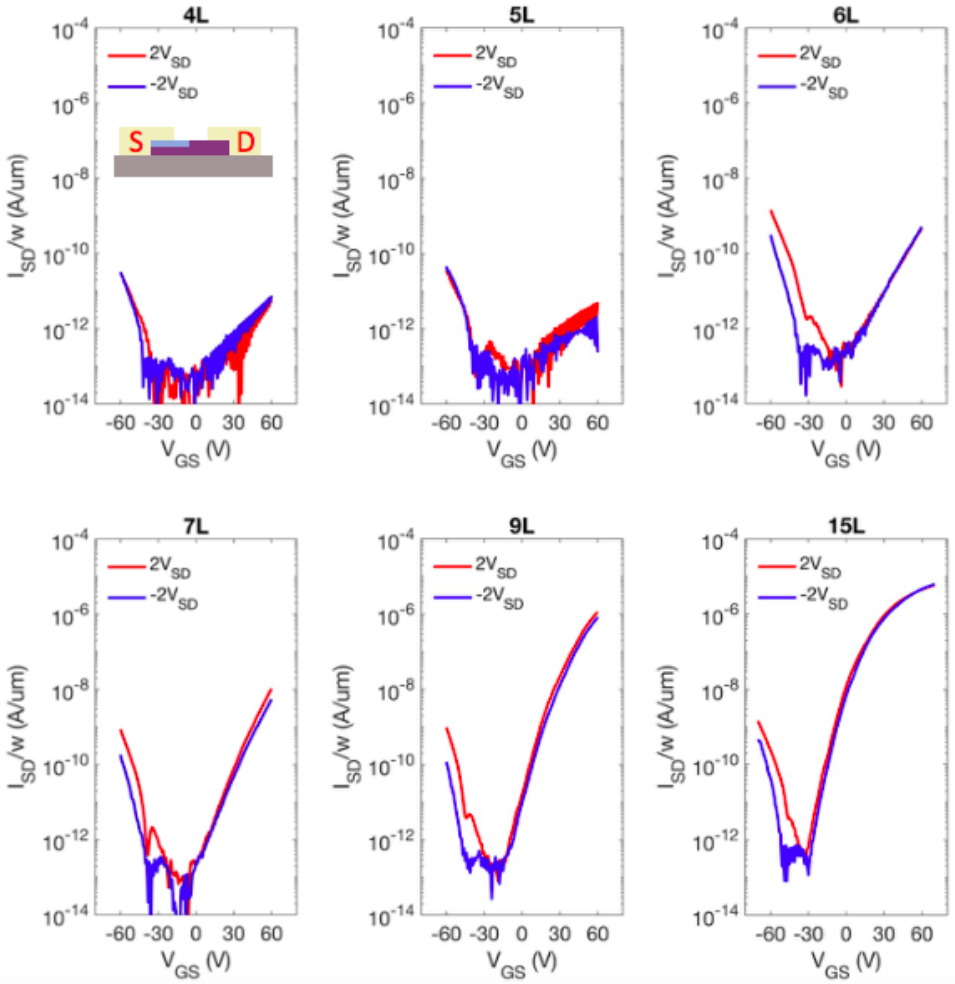

Figure 3.13: Conduction curves of 1/2 flake p-n devices. Slight rectifying behavior evident in hole conduction but electron conduction is unaffected by source drain bias direction.

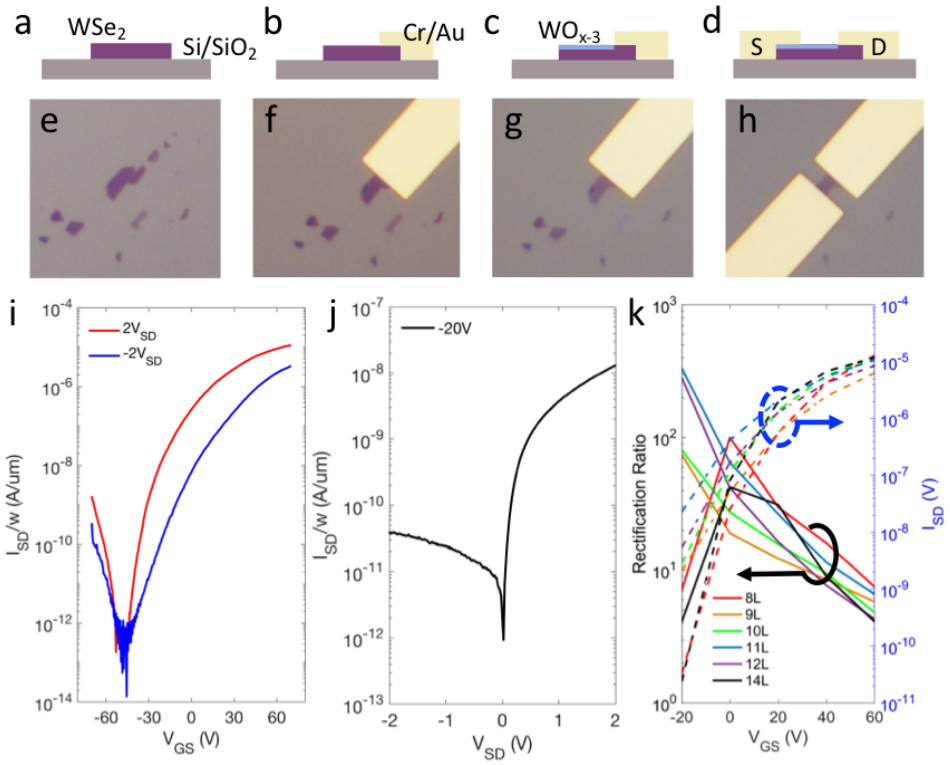

Figure 3.14: Cross-section view schematic (a-d) and optical images (e-h) of p-n homojunction fabrication process. (i) 11 layer p-n junction transfer curves under forward (2V) and reverse (-2V) bias and (j) output curve of 11 layer device at -20 VGS bias. (k) Rectification ratio (left axis) of various layered p-n devices as a function of VGS with associated forward bias (VSD = 2V) source-drain current (right axis) (g).

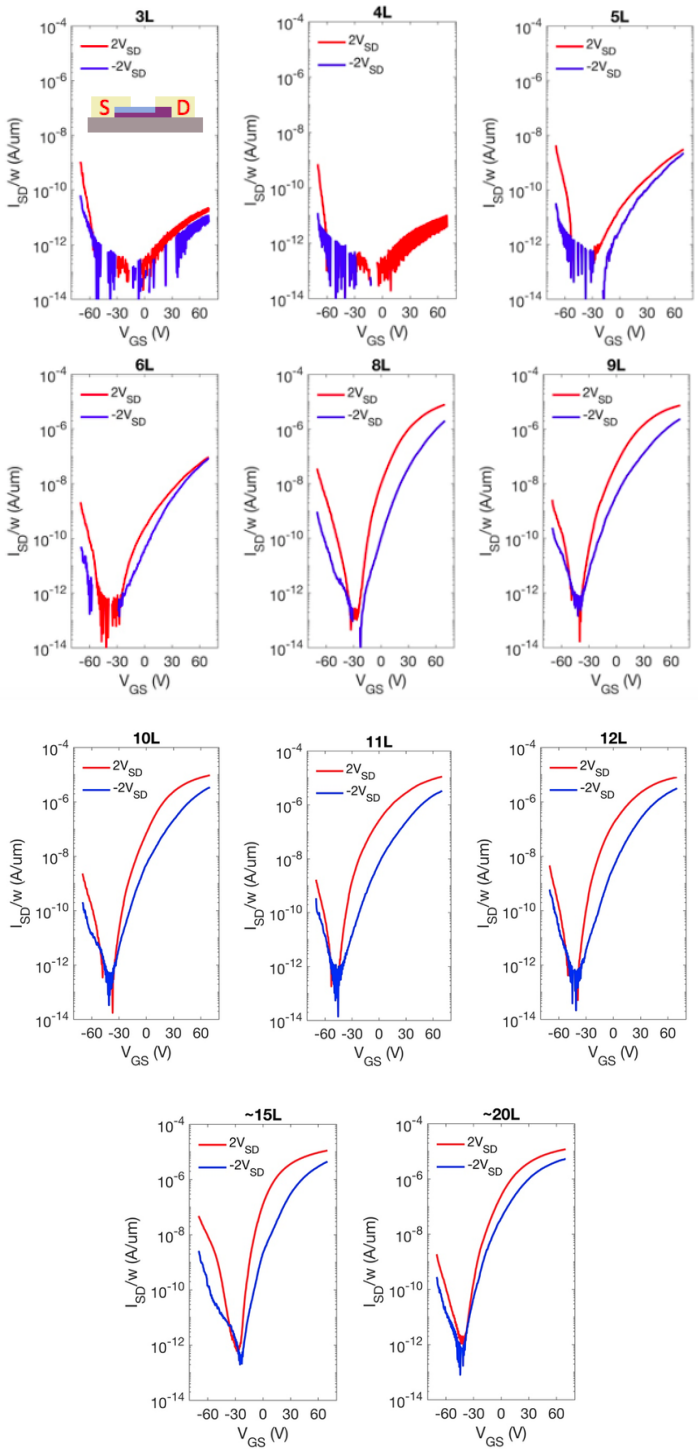

Figure 3.15: Raman map and PL study of 2L and 1L. Oxidation of the first layer is clear after just 5s of O_2 plasma exposure. Similar to the electrical cyclic results, the second layer begins to oxidize after 30 seconds of O_2 plasma with 2 layers completely oxidized after 60s of exposure.

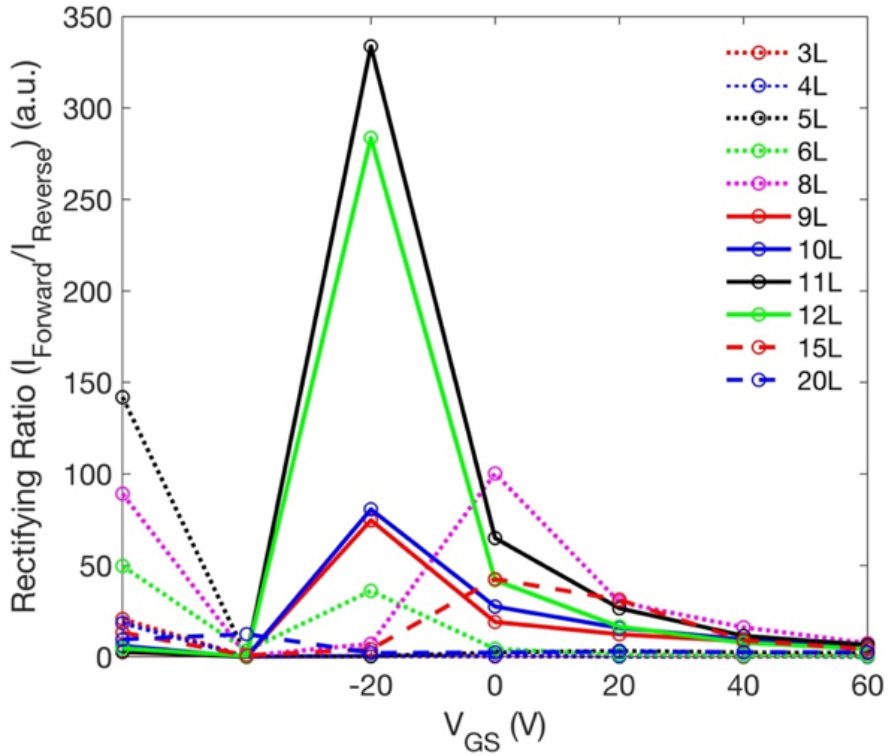

Figure 3.16: Rectification of 3/4 p-n devices. Largest rectifying behavior occurs at low negative gate voltage in 9 to 12 layer flakes. Thinner than this and overall conduction has been reduced due to the oxide, thicker and the oxide does not have significant impact on conduction due to shielding.

3.3.6 Conclusion

In this work we explore the electrical impact of oxygen plasma exposure on WSe_2. The presence of amorphous tungsten oxide is identified through XPS, Raman, PL, and AFM techniques. The rate of layer by layer oxidation is determined through a systematic Raman study. This rate is implemented in various exposure geometries of WSe_2 based FETs. First, a cyclic exposure study on the channel region is performed and found to increase p-type conduction while suppressing n-type conduction especially when the top 2 layers of the flake are oxidized. Second, the region under the electrode is exposed which results in suppressed p-type conduction and an insignificant change in n-type conduction, suggesting the oxide does not act as a hole tunneling layer as previously reported. Next, the entire flake was exposed to O_2 plasma which caused extreme suppression of p-type conduction and layer dependent suppression of n-type conduction. When these three geometries are considered together, the n-type effect of plasma exposure on the whole flake, it correlates with the combination of the channel exposure and electrode exposure effect. However, the p-type effect of plasma does not and highlights an additional term, the effect of the interaction within the WO_{3-x} layer across the FET. Using these results, an optimized pn junction was fabricated by exposing the entire channel and under one electrode. This pn junction displayed a rectifying ratio of 333 at -20V_{GS} which is consistent with other TMD lateral homojunctions.[141]

Chapter 4

PdSe2

A version of this chapter was originally published by Anna N. Hoffman, Yiyi Gu, Justin Tokash, Jonathan Woodward, Kai Xiao, and Philip D. Rack: Hoffman, A. N.; Gu, Y.; Tokash, J.; Woodward, J.; Xiao, K.; Rack, P. D. Exploring the Air Stability of $PdSe_2$ via Electrical Transport Measurements and Defect Calculations. npj 2D Mater. and Applic. 2019 PDR conceived of the experimental plan and managed the project. ANH performed the device fabrication and electrical characterization. YG and KX grew PdSe2 thin film crystals; YG performed AFM measurements; ANH with assistance from Jonathan Woodward and Harry Meyer performed XPS measurements; LL and BGS did the DFT measurements; JF developed residence time plots. The manuscript was written through contributions of all authors. The manuscript has been slightly modified to include the supplemental material.

4.1 Background

The discovery of atomically thin graphene in 2004 by Novoselov et. al. was the catalyst of the 2D materials revolution.[1] In layered materials such as graphene, boron nitride (BN), hexagonal black phosphorous (BP), and certain oxides and transition metal dichalcogenides (TMDs), weak Van der Waals forces uniquely keep layers bound together,[8] thus preparation of atomically thin layers is relatively straight forward via exfoliation from bulk crystals [65][36][66] or thin film growth. [29][52] Due to its chemical structure, each TMD monolayer has an atomically pristine surface free of dangling bonds and interface traps,[12] which pose a significant issue for silicon and other semiconductor based materials.[13] This allows for vertical scaling in advanced device fabrication with straightforward electrostatics. Processing techniques such as defect engineering,[142] laser irradiation,[143] and plasma exposure [144][145] have been utilized to control material properties and engineer devices with finely tuned properties. Most layered 2D materials have a hexagonal coordination, which promotes atomically flat layers. Recently, 2D materials which have atoms protruding out-of-plane in a regular corrugated manner, or interlayer puckering, have become a focus of research due to their interesting properties and added degree of freedom. Puckering has been observed in hexagonal BP among other 2D materials,[146] however air stability has been an ongoing challenge. Palladium diselenide ($PdSe_2$)has recently been identified as a puckered 2D

material, with the additional benefit of a low-symmetry pentagonal structure.[147][148][149] Structurally, each layer is identical, but there are significant changes in electrical and optical behavior as these layers stack due to changes in symmetry and quantum confinement.[14][15] Additionally, $PdSe_2$ is anticipated to be electrically anisotropic; mobility should vary depending on the crystal axis. The most notable and studied layer thickness dependent effect is the transition from an indirect band gap in some bulk TMD materials to a direct band gap in their monolayer counterpart. [14][6] The MoS2 band gap, for instance, varies from ∼1.2 eV in the bulk to ∼1.9 eV at the monolayer, while $PdSe_2$ varies from no gap (metallic) to 1.3 eV allowing for unique band gap control. For example, this offers a promising path to logic junction devices processed in a single material by patterning various regions with thicker (contact and resistors) and thinner (semiconductor) regions. While some report $PdSe_2$ to be intrinsically ambipolar,[148] as will be demonstrated, we tentatively attribute this behavior to adsorption at surface chalcogen vacancies and find $PdSe_2$ to be intrinsically n-type due to selenium vacancies. Due to high surface to volume ratio, optoelectronic properties can be dramatically impacted by atmospheric surface adsorbents in 2d materials with strong layer number dependence.[137][102][101] For this reason it is essential to understand impact that exposure to ambient which is often unavoidable during fabrication and characterization processes have on the electrical properties. Electrical effects of ambient adsorbents and aging have been studied for MoS2 [8][102][110][82][111][112][107] and WSe_2.[137] Studies on MoS2 suggest that ambient molecules preferentially adsorb to chalcogen surface vacancies and act as both electron traps and p-type donors.[114] While there is not a consensus on which specific adsorbents contribute to electron suppression and hole doping, most agree oxygen produces the greatest effect. The effects of water adsorption and long term aging in WSe_2 was recently studied and the enhanced p-type conductivity and n-type suppression was associated with electron transfer to adsorbed water molecules and a reduction of the selenium vacancies, respectively.[137] Furthermore, selenides have been shown to be more affected by adsorbed atmospheric species and oxidation effects than sulfides.[148][113] Previous studies on 2d materials report significant electrical behavior variation after a vacuum or inert atmosphere anneal to drive off adsorbed species such as oxygen and water.[146][148][150] Bartolomeo et al., recently explored the effects of external stimuli such as pressure, and optical and electron

irradiation on the electrical properties of exfoliated thick (∼25 layer) $PdSe_2$ field effect transistors.[151] Notably they observed a transition from strongly p-type at atmospheric pressure to ambipolar behavior when pumped to ∼ 1x10-6 Torr. In this work we explore the effects of short term (90 minutes) ambient exposures and long term (∼1000 hours) ambient aging and compare atmospheric ambient pressure versus vacuum (∼ 1x10-5 Torr) on the electrical properties of chemical vapor deposition (CVD) grown multilayer $PdSe_2$; furthermore, we investigate the potential to reverse aging effects through annealing in an inert environment. To rationalize the observed electrical property changes, density functional theory (DFT) calculations of adsorbed H2O, O_2 and O on pristine and Se vacancies in single and multilayer $PdSe_2$ are also performed.

4.2 Methods

4.2.1 Growth

The $PdSe_2$ flakes were synthesized by chemical vapor deposition (CVD) method in a one inch tube furnace. The reaction was carried out at atmospheric pressure with Ar as carrier gas. 20 mg Pd powder (99.95 %, APS 0.35-0.8 micron, Alfa Aesar) was placed in the heating center of the furnace and 1.5 g Se powder (99.9 %, Alfa Aesar) was spread on a quartz in the tube. The 300 nm SiO_2/Si substrate was located on the downstream side. The furnace was ramped up to 800 °C within 20 min and kept for 10-20 min under an argon gas flow rate of 50-150 sccm (standard cubic centimeter per minute). The heating belt controller was set as 350 °C and turned on when the furnace was ramped to 600 °C. It took approximately 2 min for the heating belt to reach 350 °C. The vapor-phase reactants were transported by the flowing argon gas to the growth region, in which the temperature was around 500 °C to 600°C, thereby feeding the growth of 2D $PdSe_2$ crystals on SiO_2/Si substrate.

4.2.2 Fabrication

Devices were fabricated via electron beam lithography utilizing spin coated Poly(methyl methacrylate) (PMMA) positive resist. Exposure was performed on an FEI 600 Nova

equipped with a Raith lithography package. 5nm Cr/25nm Au electrodes were electron beam evaporated at 3x10-6 Torr with a 0.6 /s deposition rate. The pattern was generated by lift off in an acetone bath.

4.2.3 Characterization

Devices were measured in a cryogenic vacuum probe system with a 4200 Keithley semiconductor device analyzer. To study the effect of low temperature annealing, anneals were performed in a nitrogen glove box on a hot plate pre heated to 177 °C for 12 minutes. Samples were typically measured in air, after $\sim$ 20 minutes and 72 hour in a $\sim$ 1x10-5 Torr vacuum, and then in air after the 72 hour pump down. X-ray photoemission spectroscopy measurements were performed in a Thermo Scientific XPS tool with in-situ annealing capabilities.

4.2.4 Theoretical Calculations

Plane-wave density functional theory (DFT) package VASP[116] was used for first-principles calculations with the projector-augmented-wave (PAW) pseudopotentials and the Perdew-Burke-Ernzerhof (PBE) exchange-correlation functional.[117] In addition, we adopted the van der Waals (vdW) density functional method optPBE-vdW to describe the vdW interactions.[147][152][153] To model the $PdSe_2$ surface, single-layer and six-layer $PdSe_2$ structures were built by a periodic slab geometry, where a vacuum separation of about 21 in the out-of-plane direction was used to avoid spurious interactions with periodic images. The cutoff energy was set at 400 eV, and a 12121 k-point sampling was used. All atoms were relaxed until the residual forces were below 0.02 eV/, and in-plane lattice constants were also optimized using the method of fixing the total volume (i.e., ISIF = 4 in VASP).[147][153] Then 441 supercell structures of single-layer and six-layer $PdSe_2$ were constructed with a single Se vacancy introduced on the surface to study the adsorption of O_2, O and H_2O, where the k-point sampling was reduced to 221. All the atoms were relaxed until the residual forces below 0.02 eV/.

4.3 Results and Discussion

To investigate the short term ambient exposure effects on the electrical behavior of $PdSe_2$ a 7 layer FET device was fabricated. Figure 4.1a shows an atomic force micrograph and Figure 4.1b illustrated a schematic of an as-fabricated device. As has been shown previously, $PdSe_2$ FETs annealed at 177°C in inert gas anneal show a strong decrease in p-type conduction, increased n-type conduction, and a negative threshold voltage shift.[148] To confirm this phenomena and investigate the stability of this treatment, Figure 4.1c shows the transfer characteristics of a $PdSe_2$ device measured in air before a 177°C anneal and the subsequent characteristics measured in air as a function of time after the anneal. We observe the reported strong n-type increase, p-type decrease, and negative threshold voltage shift, however over a short ambient exposure time there is a strong increase in the p-type conduction, a gradual decrease in the n-type conduction, and a strong positive threshold voltage shift toward the pre anneal levels. It should be noted that there is an approximately 5-minute delay between the anneal and the first air measurement reported below; thus, there is likely some atmospheric exposure effects convoluted in the initial measurement. To investigate the effect of ambient pressure on the electrical properties, Figure 4.1c illustrates a series transfer characteristics of another $PdSe_2$ device measured after the 177°C anneal at various times during an $\sim$ 22-hour $\sim$1x10-5 Torr vacuum exposure. Figure 4.1b and c, both show the annealed samples have a dominant n-type conduction. During the vacuum exposure there is a small decrease in the p-type conduction, however at the longer exposure time, p-type conduction approaches the original value. Thus this short term effect (¡20 minutes) could be due to trapped charge injection in the underlying SiO_2 layer caused during the repetitive forward sweep measurement from -60VGS to +60VGS.[151] The n-type conduction increases over the first 20 minutes and remains nearly constant over the next $\sim$22 hours. Overall, comparing Figure 4.1b and c, the aging is arrested in vacuum relative to the more dramatic degradation observed in the atmospheric exposure. Conversely, Bartolomeo et al., report strong pressure-dependent conduction in bulk-like exfoliated crystals where they observed reversible enhanced p-type conduction at atmospheric pressure and enhanced n-type conduction after an extended (10 hour) high-vacuum exposure.[151]

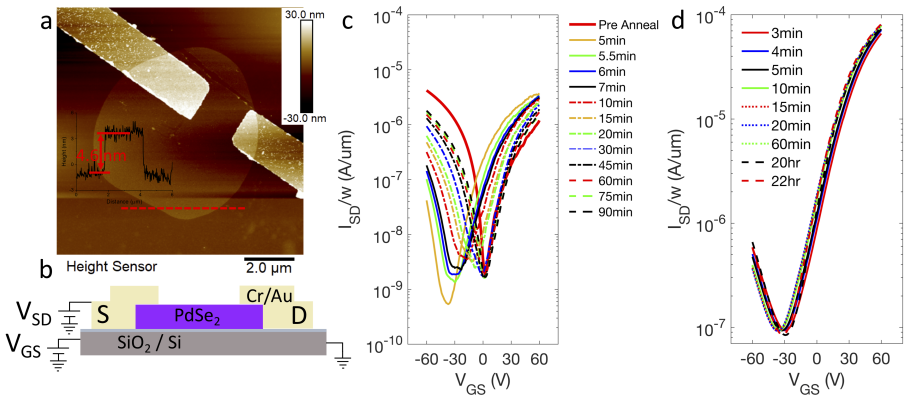

Figure 4.1: (a) atomic force micrograph of 7 layer PdSe2 device (b) schematic of all devices used in this work (c) shows the transfer characteristics of the as-fabricated device and the subsequent characteristics measured as a function of time after a 177oC -12 minute anneal. (d) shows a series transfer characteristics of a PdSe2 FET measured after the 177 oC -12 min anneal and during various times throughout a 22-hour, 1x10-5 Torr vacuum exposure

Thus, the result is a bit surprising as it was recently demonstrated in WSe_2, thinner flakes were more susceptible to pressure effects than bulk-like flakes. Subsequent to the initial short time exposure a 6 layer sample was fabricated, annealed and measured and then placed in air ambient and tested after 6, 60, 160, 430 and 840 hours of ambient aging. At each aging time, the sample was measured in air, and then measured in vacuum after a 72 hour vacuum exposure. Figure 4.2a illustrates the n-type transfer characteristics measured in air immediately after the anneal which we assume to be the pristine (time t=0) characteristics. Figure 4.2a also shows the transfer characteristics of a 6 and 840 hour aged sample measured in air and after the 72 hour vacuum exposure. The 6 hours of ambient aging clearly suppresses the n-type conduction and significantly increases the p-type conduction. After the 72 hour vacuum exposure, the n-type conduction increases by a factor of ∼4, and the change in p-type conduction is negligible. After 840 hours of ambient aging the device is purely p-type as all n-type conduction has been suppressed in our gate voltage range. However, after the 72 hour vacuum exposure some n-type conduction is recovered. Figure 4.2b and c are plots of the n- and p-type current at +/-60V gate bias versus atmospheric aging time, respectively, measured in air and after the 72 hour vacuum exposure (See Figure 4.3 for full transfer characteristics). We observe a very clear increase in the p-type conduction and decrease in the n-type conduction over this ambient aging time. Comparing the air and 72 hour vacuum exposure measurements, we observe that the change in p-type conduction is negligible (decreases by an average factor of 1.3) and the n-type conduction increases more significantly. For instance, the n-type conduction over the first 160 hours increases by on average factor of ∼5; at 430 and 840 hours the device displays only p-type conduction in air; however, as shown in Figure 4.2a, the n-type conduction is recovered after the vacuum exposure. Thus, the atmospheric aging appears to have a component that is reversible via the room temperature vacuum exposure. There was ∼20 minutes of time in air between each air measurement and when the device was pumped down into vacuum. At aging times 6 hours and longer, we deem this time insignificant however, at t=0 this ambient exposure is significant so we have not included the vacuum data point for the pristine state device.

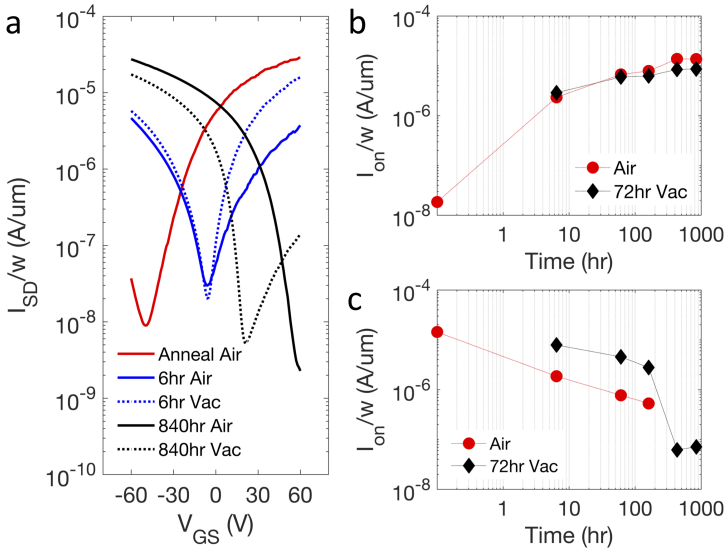

Figure 4.2: (a) illustrates the n-type transfer characteristics measured in air immediately after the anneal which we assume to be the pristine (time t=0) characteristics. (b) and (c) plot the n- and p-type current at +-60V gate voltage, respectively, versus time in air and after the 72 hour vacuum exposure measurements.

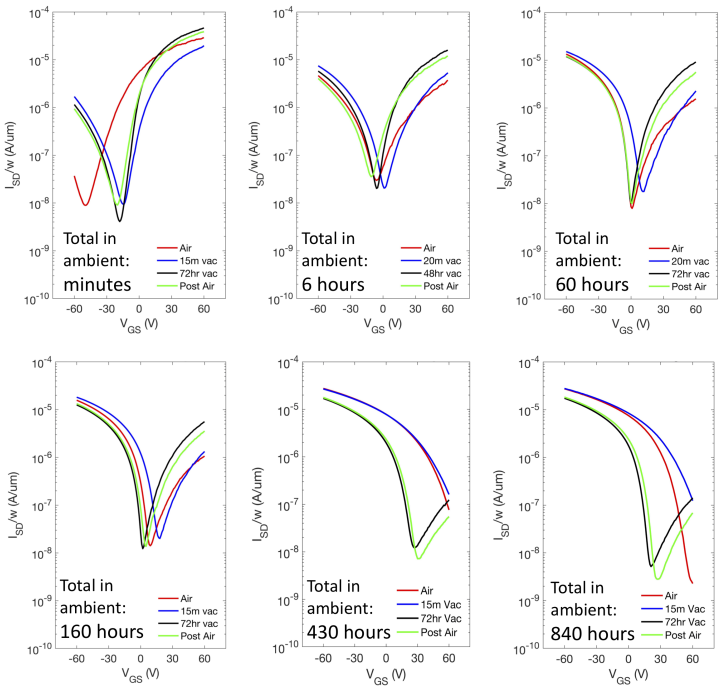

Figure 4.3: No anneal sample full transfer characteristics over time in main environments

A complimentary 6 layer $PdSe_2$ FET was fabricated and aged along with the sample described above, however this sample was re-annealed prior to each measurement. Figure 4.4a shows the transfer characteristics of this sample measured in air immediately after each anneal. Clearly the modest aging experienced up to 160 hours is largely reversible by the anneal, however some residual degradation to the n-type conduction and enhancement in the p-type conduction remains. Beyond the 160 hour measurement, both the n-type and p-type conduction decreases; thus another aging mechanism emerges between the 160 and 430 hour aging, which is consistent with the dramatic change in the n-type conduction at 430 hours in Figure 4.2.

X-ray photoelectron spectroscopy spectra were taken on a pristine $PdSe_2$ sample, samples that were aged in atmosphere for ∼120 and ∼1000 hours, and for reference a $PdSe_2$ sample that was exposed to a 15 s inductively coupled oxygen plasma exposure. Figure 4.5 illustrates the 3d spin orbit split 5/2 and 3/2 peaks for 3a, Se and 3b, Pd. Kibis et al. recently studied the thermal and plasma oxidation of Pd metal and showed that metallic Pd has a 3d 5/2 peak at 335.2 eV, and the typical PdO (Pd^{+2}) peak is at 337 eV. Furthermore, the metastable PdO_2 (Pd^{+4}) exhibit a 3d 5/2 peak at 338.2 eV. The pristine $PdSe_2$ (Pd^{+4}) peak positions of the Pd 3d 5/2 peak is 337.4 eV. The pristine peak is slightly shifted to lower binding energy relative to PdO_2, which is consistent with Se having a lower electronegativity than O and thus forming a less ionic bond. The ∼120 hour aged sample has a small Se-O shoulder emerge at ∼ 59 eV and all the peaks are shifted ∼ 0.2 eV to lower energy. The peak shift is consistent with a Fermi energy shift to toward the valence band and thus consistent with the observed emergence of the p-type conduction. At ∼1000 hours, the S-O peak is still evident, however even more pronounced is the emergence of the Pd-O_2 peak at ∼338 eV. The Pd and Se peaks are shifted ∼0.4 eV to higher energy relative to the pristine sample, which is again consistent with electrical results which show increased p-type behavior at longer ambient aging times. To confirm the peak position of the PdO_2 peak, we exposed a $PdSe_2$ sample to an oxygen plasma under similar conditions that were found to oxidize a single layer of WSe_2. Consistent with Kibis et al, the PdO_2 3d peaks are shifted ∼ 0.2 eV to lower energy compared to the PdO_2 3d peak from the long term ambient aged sample.[154][155]

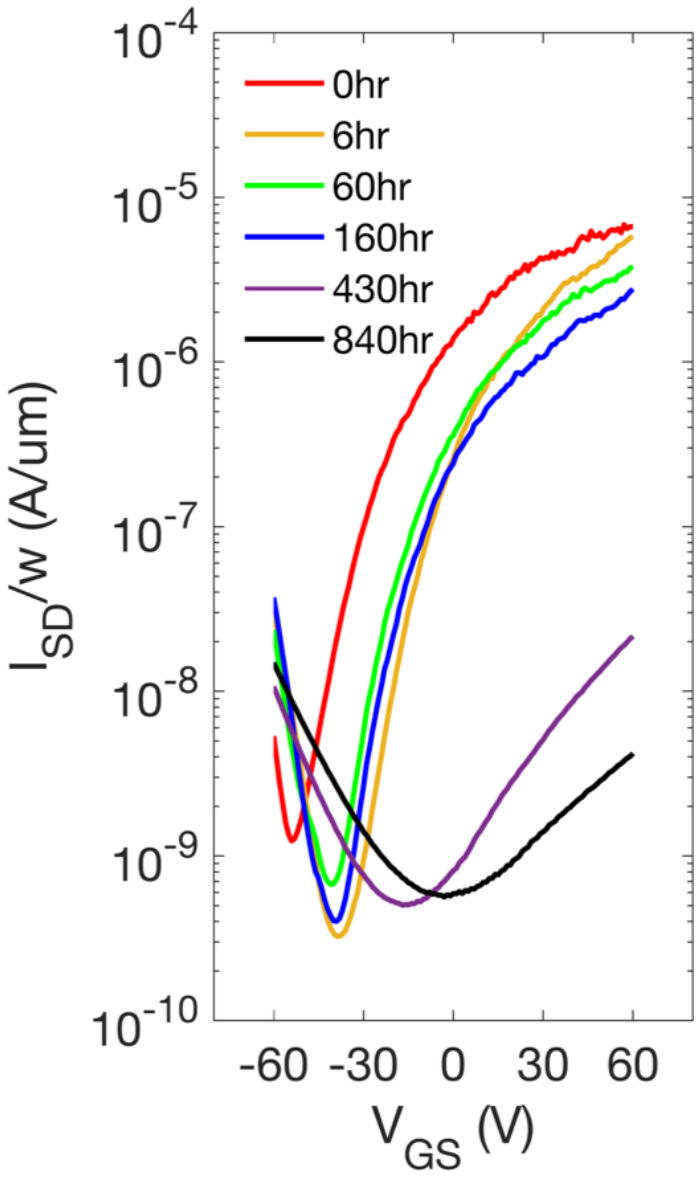

Figure 4.4: Transfer characteristics of a 6 layer PdSe2 FET measured immediately in air after a 177 °C 12 minute anneal after listed total ambient aging times

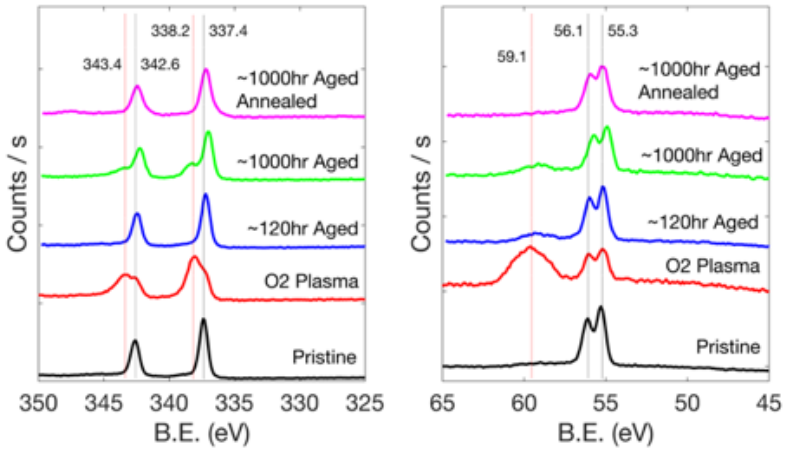

Figure 4.5: 3d spin orbit split 5/2 and 3/2 peaks for a) Pd and b) Se

Kibis et al found the PdO_2 oxide from both oxidation methods had low thermal stability over 127 °C so to support the claim that PdO_2 is forming as $PdSe_2$ samples age in ambient, the ∼1000 hour aged sample was treated with a 177 °C 12 minute anneal in situ and measured again. Figure 4.5 shows after the anneal the oxide peaks are no longer evident. There is a small peak at 347.5 eV which is identified as an energy loss peak.[156] To understand the observed change in the $PdSe_2$ electrical properties in response to the annealing process during the atmospheric aging and vacuum exposures, Table 1 summarizes density functional theory (DFT) calculations for adsorbed H2O and O_2 on pristine single and 6 layer $PdSe_2$ as well as several physi- and chemisorbed species at Se vacancies. Figure 4.6 compares the associated band structure calculations for the various defect complexes in 6 layer $PdSe_2$. Similar calculations for 1 layer $PdSe_2$ can be found in Figure 4.7. Note that the band gap reduction from 1 layer (∼1.35 eV) to 6 layers (∼0.25 eV) is slightly overestimated relative to experimentally determined optical band gaps.[147]

Interestingly, while the O_2 and H2O physisorbed binding energies and electron transfer per adsorbed molecule are higher on pristine $PdSe_2$ than for instance WSe_2, as shown in Figure 4.1c, the electrical characteristics of the annealed device is relatively stable after the short air exposure and subsequent 22-hour vacuum exposure. The change in the $PdSe_2$ electrical properties to ambient air exposure demonstrated in Figure 4.1b is thus not attributed to O_2 or H2O physisorption, which presumably has no energy barrier and would much more rapidly upon exposure to ambient. Furthermore, due to the low physisorption binding energies the electrical behavior would be reversible on a much faster time scale than the experimental room temperature vacuum measurements (see residence time plots for O_2 and H2O physisorption in Figure 4.8). Physisorption of H2O to Se vacancies has a higher binding energy, however, Figure 4.6d shows that for the 6 layer $PdSe_2$, only one of the Se donor levels is degenerate with the conduction band, thus only a modest Fermi energy shift is expected from this defect complex. Furthermore, this binding energy is also low and thus rapidly desorbed in vacuum, so the relative stability in a room temperature vacuum exposure suggests this defect is not responsible for the observed ambient exposure aging (see H2O-Se vacancy residence time plot in Figure 4.8).

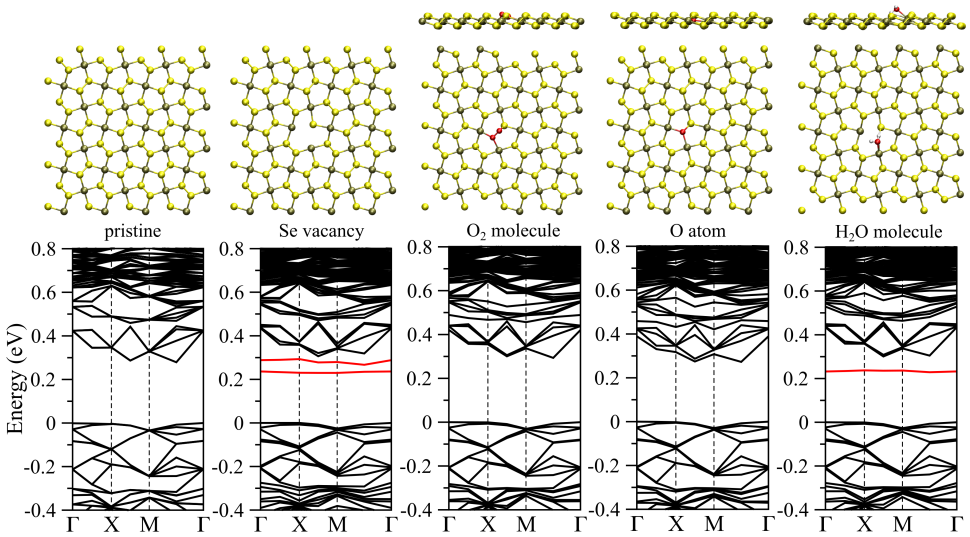

Figure 4.6: DFT-calculated electronic band structures of the 44 supercell of six-layer PdSe2 with (a) no defect, (b) a single selenium vacancy, (c) chemisorption of an O2 molecule at the vacancy site, (d) chemisorption of an O atom at the vacancy site, and (e) physisorption of a H2O molecule at the vacancy site. The Fermi level is set at 0 eV, and the in-gap defect bands are highlighted in red colors. The corresponding atomic structure (top and/or side view) is on top of the band structure. Note that only the topmost surface layer of PdSe2 is illustrated here to highlight the interface between the surface and the adsorbates.

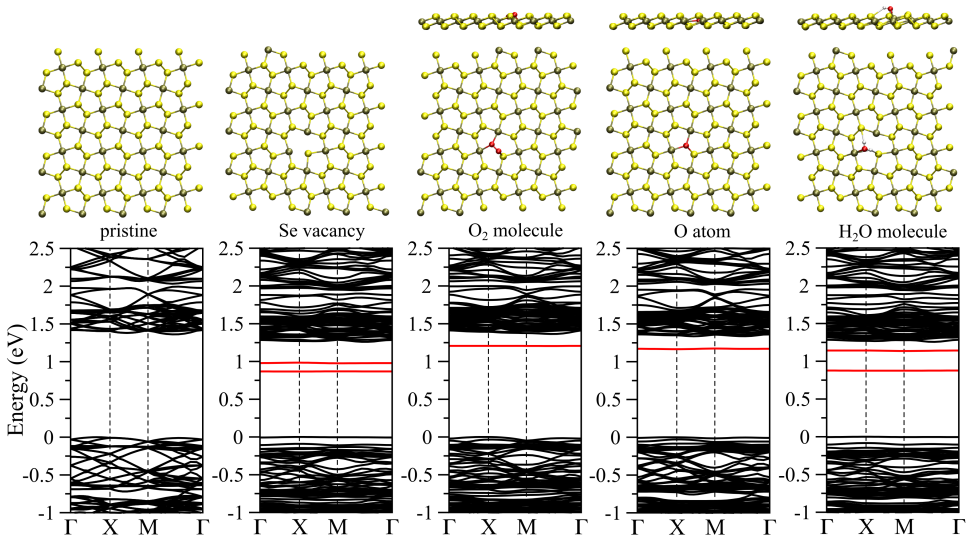

Figure 4.7: DFT-calculated electronic band structures of the 44 supercell of single-layer PdSe2 with (a) no defect, (b) a single selenium vacancy, (c) chemisorption of an O2 molecule at the vacancy site, (d) chemisorption of an O atom at the vacancy site, and (e) physisorption of a H2O molecule at the vacancy site. The Fermi level is set at 0 eV, and the in-gap defect bands are highlighted in red colors. The corresponding atomic structure (top and/or side view) is on top of the band structure.

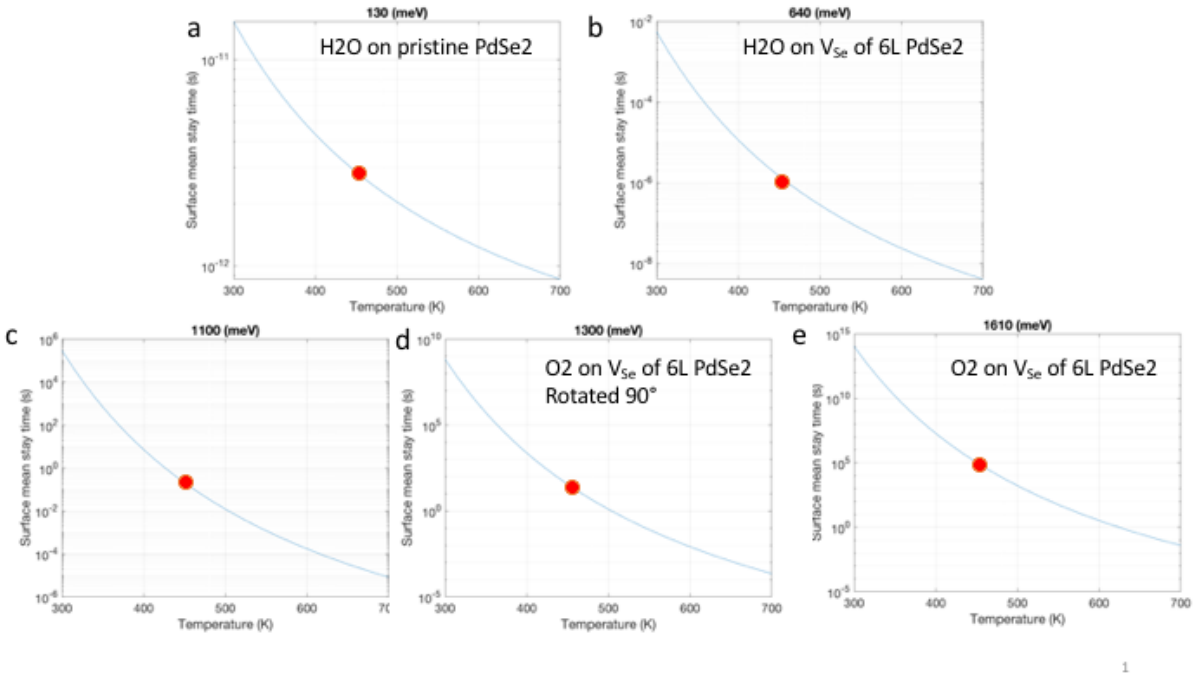

Figure 4.8: Temperature dependent residence time plots for molecules with binding energies of (a) 130meV (b) 640meV (c) 1100meV (d) 1300meV (e) 1610meV

To estimate the activation energies associated with the observed electrical changes, we correlate the short ambient aging time constant to a simple activated chemisorption process. The estimated time (τR) associated with for the n-type conduction to reduce to 1/e (36%) is approximately 10 minutes and thus the activation energy can be estimated by τ_R=τ_o exp(E_a/kT); where τ_o is the vibration frequency of the physisorbed species (1013/s), E_a is activation energy, k is Boltzmanns constant, and T is temperature. From this expression, an activation energy of $\sim$ 0.94 eV can be estimated. Furthermore, one can estimate the binding energy of this chemisorbed state by comparing the change in n-type current after the 72-hour vacuum exposure by simple first order desorption kinetics: $dC/dt = 1/\tau_{des} C_0 exp(t/\tau_{des})$, where C is concentration, t is time, τ_{des} is the desorption residence time, and C_0 is the concentration at t=0. The estimated binding energy associated with the room temperature change in n-type conduction is 1.07 eV. Comparing these values to the calculated DFT results suggests that the electrical property changes in response to short term ambient air exposure can be attributed to an activated chemisorption of O_2 at Se vacancies. As demonstrated in Table 4.1 and Figure 4.6c, molecular O_2 can chemisorb to unsaturated Pd atoms since the O=O double bond can transit to a single bond. While the O_2 molecular chemisorption leaves a defect level near the conduction band edge in single layer $PdSe_2$ as shown in Figure 4.6, both Se vacancy levels are degenerate with the conduction band in the 6 layer material. DFT calculations of the barrier energy associated with the activated chemisorption of physisorbed O_2 to chemisorbed O_2 at the VSe was determined to be about 0.85 eV, which is in good agreement with the estimated value from the time constant of 0.94 eV. The calculated binding energy for the 6 layer chemisorbed O_2 molecule at the Se vacancy is 1.61eV for the most stable adsorption configuration. The observed room temperature vacuum recovery, however, suggests a slightly lower binding energy of $\sim$1.07 eV; DFT calculations of chemisorbed O_2 molecule rotated 90 degrees yields a slightly lower binding energy of 1.30 eV. This suggests that the computed binding energy of chemisorbed O_2 molecule at the VSe can vary from 1.30 to 1.61 eV depending on the initial orientation of O_2 molecule. In the lower energy case, the reversibility of this short term ambient aging when annealed at 177°C for 12 minutes is expected, see 177°C residence times for 1.1, 1.3 and 1.61 eV in Figure 4.8 and is experimentally observed in Figure 4.5.

The long term aging associated with ¿160 hour ambient exposure is attributed to a dissociative adsorption/reaction of the O_2 molecules to atomic O and subsequent PdO_2 formation, as evidenced by the emergence of PdO_2 in the XPS spectra of a $\sim$ 1000 hour aged sample at $\sim$338eV.[154][155] PdO_2 formed by plasma oxidation of Pd was found to have low thermal stability ¿127°C,[155] thus should sublime during the 177°C anneal resulting in damaged surface layer(s) and reduced electron mobility, as seen in the 430 and 840 hour transfer characteristics of Figure 4.4. To test this, the $\sim$ 1000 hour aged sample was annealed in situ to emulate the device anneal and the XPS spectra re-measured; clearly as demonstrated in Figure 4.5, after the anneal the PdO_2 peaks are gone in agreement with PdO_2 sublimation. An alternative pathway for the dissociation of the molecular O_2 chemisorbed at the Se ($PdSeO_2$) vacancy is the formation of atomic oxygen bound to the Se vacancy. The calcualted binding energy of this defect complex in 6L $PdSe_2$ is much higher (1.99 eV), and therefore contrary to experiment, this complex would be stable to the prescribed anneal and thus not believed to be operative. Finally, comparing the ¿ 160 hour aged device in Figure 4.2, the PdO_2 formation continues to enhance the p-type conduction. This behavior is similar to the formation of WO_3 on WSe_2[145], where the WO_3 layer is electrophilic and traps the donor electrons in the near surface layer region.

Table 4.1: Binding energies and charge transfers

Site	**H_2O**		**O_2**		**O**	
	Binding Energy (eV)	Charge Transfer (e^-)	Binding Energy (eV)	Charge Transfer (e^-)	Binding Energy (eV)	Charge Transfer (e^-)
1L	0.13	0.15	0.10	0.06		
1L V_{Se}	0.48	0.51	1.61	1.09	2.10	0.87
6L V_{Se}	0.64	0.46	1.61	1.11	1.99	0.75

The apparent low temperature volatility of the PdO_2 is also consistent with the measurement after the 72 hour vacuum exposure, where the purely p-type air measurement recovers only some residual n-type behavior.

4.4 Acknowledgements

PDR and ANH acknowledge support from the Center for Nanophase Materials Sciences, which is a DOE Office of Science User Facility. ANH acknowledges support from the Center for Materials Processing. Material growth, device synthesis, and characterization measurements were conducted at the Center for Nanophase Materials Sciences, which is a DOE Office of Science User Facility.

Bibliography

[1] Kostya S Novoselov, Andre K Geim, Sergei V Morozov, D Jiang, Y_ Zhang, Sergey V Dubonos, Irina V Grigorieva, and Alexandr A Firsov. Electric field effect in atomically thin carbon films. *science*, 306(5696):666–669, 2004. 3, 18, 34, 61, 88

[2] Sheneve Z Butler, Shawna M Hollen, Linyou Cao, Yi Cui, Jay A Gupta, Humberto R Gutiérrez, Tony F Heinz, Seung Sae Hong, Jiaxing Huang, Ariel F Ismach, et al. Progress, challenges, and opportunities in two-dimensional materials beyond graphene. *ACS nano*, 7(4):2898–2926, 2013. 3

[3] Deep Jariwala, Vinod K Sangwan, Lincoln J Lauhon, Tobin J Marks, and Mark C Hersam. Emerging device applications for semiconducting two-dimensional transition metal dichalcogenides. *ACS nano*, 8(2):1102–1120, 2014. 3, 5, 7, 9, 11, 18, 21, 22, 32, 34

[4] KS Novoselov, D Jiang, F Schedin, TJ Booth, VV Khotkevich, SV Morozov, and AK Geim. Two-dimensional atomic crystals. *Proceedings of the National Academy of Sciences of the United States of America*, 102(30):10451–10453, 2005. 3

[5] Branimir Radisavljevic, Aleksandra Radenovic, Jacopo Brivio, i V Giacometti, and A Kis. Single-layer mos2 transistors. *Nature nanotechnology*, 6(3):147–150, 2011. 3, 5, 32

[6] Weijie Zhao, Zohreh Ghorannevis, Kiran Kumar Amara, Jing Ren Pang, Minglin Toh, Xin Zhang, Christian Kloc, Ping Heng Tan, and Goki Eda. Lattice dynamics in mono- and few-layer sheets of ws 2 and wse 2. *Nanoscale*, 5(20):9677–9683, 2013. 3, 5, 7, 11, 12, 32, 89

[7] NV Podberezskaya, SA Magarill, NV Pervukhina, and SV Borisov. Crystal chemistry of dichalcogenides mx2. *Journal of Structural Chemistry*, 42(4):654–681, 2001. 3

[8] Hui Zhu, Xiaoye Qin, Lanxia Cheng, Angelica Azcatl, Jiyoung Kim, and Robert M Wallace. Remote plasma oxidation and atomic layer etching of mos2. *ACS applied materials & interfaces*, 8(29):19119–19126, 2016. 3, 9, 28, 30, 36, 62, 74, 88, 89

[9] Goki Eda, Hisato Yamaguchi, Damien Voiry, Takeshi Fujita, Mingwei Chen, and Manish Chhowalla. Photoluminescence from chemically exfoliated mos2. *Nano letters*, 11(12):5111–5116, 2011. 3

[10] Manish Chhowalla, Hyeon Suk Shin, Goki Eda, Lain-Jong Li, Kian Ping Loh, and Hua Zhang. The chemistry of two-dimensional layered transition metal dichalcogenide nanosheets. *Nature chemistry*, 5(4):263–275, 2013. viii, 4, 32

[11] Goki Eda, Takeshi Fujita, Hisato Yamaguchi, Damien Voiry, Mingwei Chen, and Manish Chhowalla. Coherent atomic and electronic heterostructures of single-layer mos2. *Acs Nano*, 6(8):7311–7317, 2012. viii, 4, 32

[12] Wei Liu, Jiahao Kang, Deblina Sarkar, Yasin Khatami, Debdeep Jena, and Kaustav Banerjee. Role of metal contacts in designing high-performance monolayer n-type wse2 field effect transistors. *Nano letters*, 13(5):1983–1990, 2013. 5, 11, 15, 18, 32, 34, 65, 88

[13] SK Lai. Interface trap generation in silicon dioxide when electrons are captured by trapped holes. *Journal of Applied Physics*, 54(5):2540–2546, 1983. 5, 88

[14] Kin Fai Mak, Changgu Lee, James Hone, Jie Shan, and Tony F Heinz. Atomically thin mos 2: a new direct-gap semiconductor. *Physical review letters*, 105(13):136805, 2010. 5, 7, 89

[15] Changgu Lee, Hugen Yan, Louis E Brus, Tony F Heinz, James Hone, and Sunmin Ryu. Anomalous lattice vibrations of single-and few-layer mos2. *ACS nano*, 4(5):2695–2700, 2010. 5, 11, 12, 34, 61, 89

[16] Hai Li, Gang Lu, Zongyou Yin, Qiyuan He, Hong Li, Qing Zhang, and Hua Zhang. Optical identification of single-and few-layer mos2 sheets. *Small*, 8(5):682–686, 2012. 5, 21

[17] Hai Li, Gang Lu, Yanlong Wang, Zongyou Yin, Chunxiao Cong, Qiyuan He, Lu Wang, Feng Ding, Ting Yu, and Hua Zhang. Mechanical exfoliation and characterization of

single-and few-layer nanosheets of wse2, tas2, and tase2. *Small*, 9(11):1974–1981, 2013. 5, 62, 68, 72

[18] Nan Ma and Debdeep Jena. Charge scattering and mobility in atomically thin semiconductors. *Physical Review X*, 4(1):011043, 2014. 5, 34, 35, 61

[19] Xiaodong Li, Jeffrey T Mullen, Zhenghe Jin, Kostyantyn M Borysenko, M Buongiorno Nardelli, and Ki Wook Kim. Intrinsic electrical transport properties of monolayer silicene and mos 2 from first principles. *Physical Review B*, 87(11):115418, 2013. 5, 7, 34, 35

[20] Bilu Liu, Yuqiang Ma, Anyi Zhang, Liang Chen, Ahmad N Abbas, Yihang Liu, Chenfei Shen, Haochuan Wan, and Chongwu Zhou. High-performance wse2 field-effect transistors via controlled formation of in-plane heterojunctions. *ACS nano*, 10(5):5153–5160, 2016. 5, 15, 28, 30

[21] Hui Fang, Steven Chuang, Ting Chia Chang, Kuniharu Takei, Toshitake Takahashi, and Ali Javey. High-performance single layered wse2 p-fets with chemically doped contacts. *Nano letters*, 12(7):3788–3792, 2012. 5, 11, 15, 18

[22] Vinod K Sangwan, Heather N Arnold, Deep Jariwala, Tobin J Marks, Lincoln J Lauhon, and Mark C Hersam. Low-frequency electronic noise in single-layer mos2 transistors. *Nano letters*, 13(9):4351–4355, 2013. 5

[23] Pushpa Raj Pudasaini, Michael G Stanford, Akinola Oyedele, Anthony Wong, Anna Hofmann, Dayrl Briggs, Kai Xiao, David G Mandrus, Thomas Z Ward, and Philip D Rack. High performance top-gated multilayer wse2 field effect transistors. *Nanotechnology*, 2017. 5, 68

[24] Deep Jariwala, Vinod K Sangwan, Dattatray J Late, James E Johns, Vinayak P Dravid, Tobin J Marks, Lincoln J Lauhon, and Mark C Hersam. Band-like transport in high mobility unencapsulated single-layer mos2 transistors. *Applied Physics Letters*, 102(17):173107, 2013. 5

[25] Wenjing Zhang, Jing-Kai Huang, Chang-Hsiao Chen, Yung-Huang Chang, Yuh-Jen Cheng, and Lain-Jong Li. High-gain phototransistors based on a cvd mos2 monolayer. *Advanced materials*, 25(25):3456–3461, 2013. 5

[26] Meeghage Madusanka Perera, Ming-Wei Lin, Hsun-Jen Chuang, Bhim Prasad Chamlagain, Chongyu Wang, Xuebin Tan, Mark Ming-Cheng Cheng, David Tománek, and Zhixian Zhou. Improved carrier mobility in few-layer mos2 field-effect transistors with ionic-liquid gating. *Acs Nano*, 7(5):4449–4458, 2013. 5

[27] Ming-Wei Lin, Lezhang Liu, Qing Lan, Xuebin Tan, Kulwinder S Dhindsa, Peng Zeng, Vaman M Naik, Mark Ming-Cheng Cheng, and Zhixian Zhou. Mobility enhancement and highly efficient gating of monolayer mos2 transistors with polymer electrolyte. *Journal of Physics D: Applied Physics*, 45(34):345102, 2012. 5

[28] Pyo Jin Jeon, Sung-Wook Min, Jin Sung Kim, Syed Raza Ali Raza, Kyunghee Choi, Hee Sung Lee, Young Tack Lee, Do Kyung Hwang, Hyoung Joon Choi, and Seongil Im. Enhanced device performances of wse 2–mos 2 van der waals junction p–n diode by fluoropolymer encapsulation. *Journal of Materials Chemistry C*, 3(12):2751–2758, 2015. 5, 26

[29] Hailong Zhou, Chen Wang, Jonathan C Shaw, Rui Cheng, Yu Chen, Xiaoqing Huang, Yuan Liu, Nathan O Weiss, Zhaoyang Lin, Yu Huang, et al. Large area growth and electrical properties of p-type wse2 atomic layers. *Nano letters*, 15(1):709–713, 2014. 7, 11, 12, 15, 18, 35, 88

[30] Weijie Zhao, Zohreh Ghorannevis, Leiqiang Chu, Minglin Toh, Christian Kloc, Ping-Heng Tan, and Goki Eda. Evolution of electronic structure in atomically thin sheets of ws2 and wse2. *ACS nano*, 7(1):791–797, 2012. 7, 11, 12

[31] Jason K Ellis, Melissa J Lucero, and Gustavo E Scuseria. The indirect to direct band gap transition in multilayered mos2 as predicted by screened hybrid density functional theory. *Applied Physics Letters*, 99(26):261908, 2011. 7

[32] Zongyou Yin, Hai Li, Hong Li, Lin Jiang, Yumeng Shi, Yinghui Sun, Gang Lu, Qing Zhang, Xiaodong Chen, and Hua Zhang. Single-layer mos2 phototransistors. *ACS nano*, 6(1):74–80, 2011. 7

[33] AA Al-Hilli and BL Evans. The preparation and properties of transition metal dichalcogenide single crystals. *Journal of Crystal Growth*, 15(2):93–101, 1972. 7, 15

[34] Hai Li, Jumiati Wu, Zongyou Yin, and Hua Zhang. Preparation and applications of mechanically exfoliated single-layer and multilayer mos2 and wse2 nanosheets. *Accounts of chemical research*, 47(4):1067–1075, 2014. 7, 9, 11

[35] Di Xiao, Gui-Bin Liu, Wanxiang Feng, Xiaodong Xu, and Wang Yao. Coupled spin and valley physics in monolayers of mos 2 and other group-vi dichalcogenides. *Physical Review Letters*, 108(19):196802, 2012. 7

[36] Hualing Zeng, Junfeng Dai, Wang Yao, Di Xiao, and Xiaodong Cui. Valley polarization in mos2 monolayers by optical pumping. *Nature nanotechnology*, 7(8):490–493, 2012. 7, 18, 88

[37] Sujay B Desai, Gyungseon Seol, Jeong Seuk Kang, Hui Fang, Corsin Battaglia, Rehan Kapadia, Joel W Ager, Jing Guo, and Ali Javey. Strain-induced indirect to direct bandgap transition in multilayer wse2. *Nano letters*, 14(8):4592–4597, 2014. 7, 12, 32

[38] Kin Fai Mak and Jie Shan. Photonics and optoelectronics of 2d semiconductor transition metal dichalcogenides. *Nature Photonics*, 10(4):216–226, 2016. 7

[39] A Kumar and PK Ahluwalia. Electronic structure of transition metal dichalcogenides monolayers 1h-mx2 (m= mo, w; x= s, se, te) from ab-initio theory: new direct band gap semiconductors. *The European Physical Journal B*, 85(6):186, 2012. viii, 8, 32

[40] Oriol Lopez-Sanchez, Dominik Lembke, Metin Kayci, Aleksandra Radenovic, and Andras Kis. Ultrasensitive photodetectors based on monolayer mos2. *Nature nanotechnology*, 8(7):497–501, 2013. 9

[41] Thanasis Georgiou, Rashid Jalil, Branson D Belle, Liam Britnell, Roman V Gorbachev, Sergey V Morozov, Yong-Jin Kim, Ali Gholinia, Sarah J Haigh, Oleg Makarovsky, et al. Vertical field-effect transistor based on graphene-ws2 heterostructures for flexible and transparent electronics. *Nature nanotechnology*, 8(2):100–103, 2013. 9

[42] Heejun Yang, Jinseong Heo, Seongjun Park, Hyun Jae Song, David H Seo, Kyung-Eun Byun, Philip Kim, InKyeong Yoo, Hyun-Jong Chung, and Kinam Kim. Graphene barristor, a triode device with a gate-controlled schottky barrier. *Science*, 336(6085):1140–1143, 2012. 9

[43] Mahito Yamamoto, Sudipta Dutta, Shinya Aikawa, Shu Nakaharai, Katsunori Wakabayashi, Michael S Fuhrer, Keiji Ueno, and Kazuhito Tsukagoshi. Self-limiting layer-by-layer oxidation of atomically thin wse2. *Nano letters*, 15(3):2067–2073, 2015. 9, 15, 28, 30, 62, 63, 72, 74, 78

[44] Zhen Li, Sisi Yang, Rohan Dhall, Ewa Kosmowska, Haotian Shi, Ioannis Chatzakis, and Stephen B Cronin. Layer control of wse2 via selective surface layer oxidation. *ACS nano*, 10(7):6836–6842, 2016. viii, 9, 15, 28, 29, 30, 32

[45] Sera Kim, Jung Ho Kim, Dohyun Kim, Geunwoo Hwang, Jaeyoon Baik, Heejun Yang, and Suyeon Cho. Post-patterning of an electronic homojunction in atomically thin monoclinic mote2. *2D Materials*, 4(2):024004, 2017. 9

[46] Michael G Stanford, Pushpa R Pudasaini, Nicholas Cross, Kyle Mahady, Anna N Hoffman, David G Mandrus, Gerd Duscher, Matthew F Chisholm, and Philip D Rack. Tungsten diselenide patterning and nanoribbon formation by gas-assisted focused-helium-ion-beam-induced etching. *Small Methods*, 1(4):1600060, 2017. 9, 32

[47] Michael G Stanford, Pushpa R Pudasaini, Elisabeth T Gallmeier, Nicholas Cross, Liangbo Liang, Gerd Duscher, Masoud Mahjouri-Samani, Kai Wang, Kai Xiao, David B Geohegan, et al. High conduction hopping behavior induced in transition metal dichalcogenides by percolating defect networks: toward atomically thin circuits. *arXiv preprint arXiv:1705.05503*, 2017. 9, 24, 26, 32

[48] Hai Li, Zongyou Yin, Qiyuan He, Hong Li, Xiao Huang, Gang Lu, Derrick Wen Hui Fam, Alfred Iing Yoong Tok, Qing Zhang, and Hua Zhang. Fabrication of single-and multilayer mos2 film-based field-effect transistors for sensing no at room temperature. *small*, 8(1):63–67, 2012. 9

[49] Han Wang, Lili Yu, Yi-Hsien Lee, Yumeng Shi, Allen Hsu, Matthew L Chin, Lain-Jong Li, Madan Dubey, Jing Kong, and Tomas Palacios. Integrated circuits based on bilayer mos2 transistors. *Nano letters*, 12(9):4674–4680, 2012. 9

[50] Gwan-Hyoung Lee, Young-Jun Yu, Xu Cui, Nicholas Petrone, Chul-Ho Lee, Min Sup Choi, Dae-Yeong Lee, Changgu Lee, Won Jong Yoo, Kenji Watanabe, et al. Flexible and transparent mos2 field-effect transistors on hexagonal boron nitride-graphene heterostructures. *ACS nano*, 7(9):7931–7936, 2013. 9

[51] Adrian Kitai. *Principles of Solar Cells, LEDs and Diodes: The role of the PN junction*. John Wiley & Sons, 2011. viii, 10, 32

[52] Bilu Liu, Mohammad Fathi, Liang Chen, Ahmad Abbas, Yuqiang Ma, and Chongwu Zhou. Chemical vapor deposition growth of monolayer wse2 with tunable device characteristics and growth mechanism study. *ACS nano*, 9(6):6119–6127, 2015. 11, 15, 88

[53] Pushpa Raj Pudasaini, Akinola Oyedele, Cheng Zhang, Michael G Stanford, Nicholas Cross, Anthony T Wong, Anna N Hoffman, Kai Xiao, Gerd Duscher, David G Mandrus, et al. High-performance multilayer wse2 field-effect transistors with carrier type control. *Nano Research*, pages 1–9, 2017. viii, 11, 15, 16, 30, 32

[54] Genevieve Clark, Sanfeng Wu, Pasqual Rivera, Joseph Finney, Paul Nguyen, David H Cobden, and Xiaodong Xu. Vapor-transport growth of high optical quality wse2 monolayers a. *APL Materials*, 2(10):101101, 2014. 11, 15

[55] Catalin Chiritescu, David G Cahill, Ngoc Nguyen, David Johnson, Arun Bodapati, Pawel Keblinski, and Paul Zschack. Ultralow thermal conductivity in disordered, layered wse2 crystals. *Science*, 315(5810):351–353, 2007. 11, 18

[56] Yuqiang Ma, Bilu Liu, Anyi Zhang, Liang Chen, Mohammad Fathi, Chenfei Shen, Ahmad N Abbas, Mingyuan Ge, Matthew Mecklenburg, and Chongwu Zhou. Reversible semiconducting-to-metallic phase transition in chemical vapor deposition grown monolayer wse2 and applications for devices. *ACS nano*, 9(7):7383–7391, 2015. 11

[57] Jing-Kai Huang, Jiang Pu, Chang-Lung Hsu, Ming-Hui Chiu, Zhen-Yu Juang, Yung-Huang Chang, Wen-Hao Chang, Yoshihiro Iwasa, Taishi Takenobu, and Lain-Jong Li. Large-area synthesis of highly crystalline wse2 monolayers and device applications. *ACS nano*, 8(1):923–930, 2013. 11, 15, 35, 36

[58] H. Sahin, S. Tongay, S. Horzum, W. Fan, J. Zhou, J. Li, J. Wu, and F. M. Peeters. Anomalous raman spectra and thickness-dependent electronic properties of wse_2. *Phys. Rev. B*, 87:165409, Apr 2013. 11

[59] A. Molina-Sánchez and L. Wirtz. Phonons in single-layer and few-layer mos_2 and ws_2. *Phys. Rev. B*, 84:155413, Oct 2011. 12

[60] Mahito Yamamoto, Shu Nakaharai, Keiji Ueno, and Kazuhito Tsukagoshi. Self-limiting oxides on wse2 as controlled surface acceptors and low-resistance hole contacts. *Nano letters*, 16(4):2720–2727, 2016. viii, 15, 28, 29, 30, 32, 62, 68, 74

[61] Joey F Crider. Self-propagating high temperature synthesis. In *Ceramic Engineering and Science Proceedings*, volume 3, pages 519–528, 1982. 15

[62] VA Obolonchik and LM Prokoshina. Synthesis of selenides of the transition metals by the interaction of the oxides with hydrogen selenide. *ZHUR PRIDLAK KHIM*, 44(10):2166–2170, 1971. 15

[63] Jen-Ru Chen, Patrick M Odenthal, Adrian G Swartz, George Charles Floyd, Hua Wen, Kelly Yunqiu Luo, and Roland K Kawakami. Control of schottky barriers in single layer mos2 transistors with ferromagnetic contacts. *Nano letters*, 13(7):3106–3110, 2013. 18

[64] Valeria Nicolosi, Manish Chhowalla, Mercouri G Kanatzidis, Michael S Strano, and Jonathan N Coleman. Liquid exfoliation of layered materials. *Science*, 340(6139):1226419, 2013. 18

[65] Jian Zheng, Han Zhang, Shaohua Dong, Yanpeng Liu, Chang Tai Nai, Hyeon Suk Shin, Hu Young Jeong, Bo Liu, and Kian Ping Loh. High yield exfoliation of two-dimensional chalcogenides using sodium naphthalenide. *Nature communications*, 5:2995, 2014. 18, 88

[66] Dattatray J Late, Bin Liu, HSS Matte, CNR Rao, and Vinayak P Dravid. Rapid characterization of ultrathin layers of chalcogenides on sio2/si substrates. *Advanced Functional Materials*, 22(9):1894–1905, 2012. 18, 62, 88

[67] Eswaraiah Varrla, Claudia Backes, Keith R Paton, Andrew Harvey, Zahra Gholamvand, Joe McCauley, and Jonathan N Coleman. Large-scale production of size-controlled mos2 nanosheets by shear exfoliation. *Chemistry of Materials*, 27(3):1129–1139, 2015. 18

[68] Xianjue Chen, John F Dobson, and Colin L Raston. Vortex fluidic exfoliation of graphite and boron nitride. *Chemical Communications*, 48(31):3703–3705, 2012. 18

[69] Leonard J Brillson and Yicheng Lu. Zno schottky barriers and ohmic contacts. *Journal of Applied Physics*, 109(12):8, 2011. viii, 19

[70] Y Fan, J Han, L He, J Saraie, RL Gunshor, M Hagerott, H Jeon, AV Nurmikko, GC Hua, and N Otsuka. Graded band gap ohmic contact to p-znse. *Applied physics letters*, 61(26):3160–3162, 1992. viii, 19, 32

[71] Zhong Lin, Bruno R Carvalho, Ethan Kahn, Ruitao Lv, Rahul Rao, Humberto Terrones, Marcos A Pimenta, and Mauricio Terrones. Defect engineering of two-dimensional transition metal dichalcogenides. *2D Materials*, 3(2):022002, 2016. viii, 21, 23, 24, 26, 28, 32

[72] Yuda Zhao, Kang Xu, Feng Pan, Changjian Zhou, Feichi Zhou, and Yang Chai. Doping, contact and interface engineering of two-dimensional layered transition metal dichalcogenides transistors. *Advanced Functional Materials*, 27(19), 2017. 21, 22

[73] Feifei Xia, Zhibin Shao, Yuanyuan He, Rongbin Wang, Xiaofeng Wu, Tianhao Jiang, Steffen Duhm, Jianwei Zhao, Shuit-Tong Lee, and Jiansheng Jie. Surface charge transfer doping via transition metal oxides for efficient p-type doping of ii–vi nanostructures. *ACS nano*, 10(11):10283–10293, 2016. 22

[74] JA Pollock, M Weyland, DJ Taplin, LJ Allen, and SD Findlay. Accuracy and precision of thickness determination from position-averaged convergent beam electron diffraction patterns using a single-parameter metric. *Ultramicroscopy*, 181:86–96, 2017. 22

[75] Y Guo, D Liu, and J Robertson. Chalcogen vacancies in monolayer transition metal dichalcogenides and fermi level pinning at contacts. *Applied Physics Letters*, 106(17):173106, 2015. 24

[76] Sefaattin Tongay, Joonki Suh, Can Ataca, Wen Fan, Alexander Luce, Jeong Seuk Kang, Jonathan Liu, Changhyun Ko, Rajamani Raghunathanan, Jian Zhou, et al. Defects activated photoluminescence in two-dimensional semiconductors: interplay between bound, charged, and free excitons. *Scientific reports*, 3:2657, 2013. 24, 26, 28

[77] Stephen McDonnell, Rafik Addou, Creighton Buie, Robert M Wallace, and Christopher L Hinkle. Defect-dominated doping and contact resistance in mos2. *ACS nano*, 8(3):2880–2888, 2014. 24, 30, 35

[78] Hao Qiu, Tao Xu, Zilu Wang, Wei Ren, Haiyan Nan, Zhenhua Ni, Qian Chen, Shijun Yuan, Feng Miao, Fengqi Song, et al. Hopping transport through defect-induced localized states in molybdenum disulfide. *arXiv preprint arXiv:1309.3711*, 2013. 24

[79] Hannu-Pekka Komsa, Simon Kurasch, Ossi Lehtinen, Ute Kaiser, and Arkady V Krasheninnikov. From point to extended defects in two-dimensional mos 2: evolution of atomic structure under electron irradiation. *Physical Review B*, 88(3):035301, 2013. 24

[80] Junhao Lin, Sokrates T Pantelides, and Wu Zhou. Vacancy-induced formation and growth of inversion domains in transition-metal dichalcogenide monolayer. *ACS nano*, 9(5):5189–5197, 2015. 24

[81] Tae-Young Kim, Kyungjune Cho, Woanseo Park, Juhun Park, Younggul Song, Seunghun Hong, Woong-Ki Hong, and Takhee Lee. Irradiation effects of high-energy proton beams on mos2 field effect transistors. *ACS nano*, 8(3):2774–2781, 2014. 26

[82] Haiyan Nan, Zilu Wang, Wenhui Wang, Zheng Liang, Yan Lu, Qian Chen, Daowei He, Pingheng Tan, Feng Miao, Xinran Wang, et al. Strong photoluminescence enhancement of mos2 through defect engineering and oxygen bonding. *ACS nano*, 8(6):5738–5745, 2014. 26, 28, 30, 36, 74, 89

[83] O Ochedowski, K Marinov, G Wilbs, G Keller, N Scheuschner, D Severin, M Bender, J Maultzsch, FJ Tegude, and M Schleberger. Radiation hardness of graphene and mos2 field effect devices against swift heavy ion irradiation. *Journal of Applied Physics*, 113(21):214306, 2013. 26

[84] Daniel S Fox, Yangbo Zhou, Pierce Maguire, Arlene ONeill, Cormac OCoileain, Riley Gatensby, Alexey M Glushenkov, Tao Tao, Georg S Duesberg, Igor V Shvets, et al. Nanopatterning and electrical tuning of mos2 layers with a subnanometer helium ion beam. *Nano letters*, 15(8):5307–5313, 2015. viii, 26, 27, 32

[85] S Mathew, K Gopinadhan, TK Chan, XJ Yu, D Zhan, L Cao, A Rusydi, MBH Breese, S Dhar, ZX Shen, et al. Magnetism in mos2 induced by proton irradiation. *Applied Physics Letters*, 101(10):102103, 2012. 26

[86] Shaoqing Xiao, Peng Xiao, Xuecheng Zhang, Dawei Yan, Xiaofeng Gu, Fang Qin, Zhenhua Ni, Zhao Jun Han, and Kostya Ken Ostrikov. Atomic-layer soft plasma etching of mos2. *Scientific reports*, 6, 2016. 28

[87] Steven Chuang, Corsin Battaglia, Angelica Azcatl, Stephen McDonnell, Jeong Seuk Kang, Xingtian Yin, Mahmut Tosun, Rehan Kapadia, Hui Fang, Robert M Wallace,

et al. Mos2 p-type transistors and diodes enabled by high work function moo x contacts. *Nano letters*, 14(3):1337–1342, 2014. 30

[88] Emanuele Rimini. *Ion implantation: basics to device fabrication*, volume 293. Springer Science & Business Media, 2013. 32

[89] Philipp Tonndorf, Robert Schmidt, Philipp Böttger, Xiao Zhang, Janna Börner, Andreas Liebig, Manfred Albrecht, Christian Kloc, Ovidiu Gordan, Dietrich RT Zahn, et al. Photoluminescence emission and raman response of monolayer mos 2, mose 2, and wse 2. *Optics express*, 21(4):4908–4916, 2013. 32, 62

[90] Ruitao Lv, Joshua A Robinson, Raymond E Schaak, Du Sun, Yifan Sun, Thomas E Mallouk, and Mauricio Terrones. Transition metal dichalcogenides and beyond: synthesis, properties, and applications of single-and few-layer nanosheets. *Accounts of chemical research*, 48(1):56–64, 2014. 32

[91] Antonio Castro Neto, Francisco Guinea, and Nuno Miguel Peres. Drawing conclusions from graphene. *Physics World*, 19(11):33, 2006. 32

[92] Scott E Thompson and Srivatsan Parthasarathy. Moore's law: the future of si microelectronics. *Materials today*, 9(6):20–25, 2006. 32

[93] Pushpa Raj Pudasaini, Akinola Oyedele, Cheng Zhang, Michael G Stanford, Nicholas Cross, Anthony T Wong, Anna N Hoffman, Kai Xiao, Gerd Duscher, David G Mandrus, Thomas Z. Ward, and Philip D. Rack. High-performance Multilayer WSe2 field-effect transistors with carrier type control. *Nano Research*, 11(2):722–730, 2018. 34, 35, 65

[94] Britton W.H. Baugher, Hugh O.H. Churchill, Yafang Yang, and Pablo Jarillo-Herrero. Optoelectronic devices based on electrically tunable p-n diodes in a monolayer dichalcogenide. *Nature Nanotechnology*, 9(4):262–267, 2014. 34

[95] C M Smyth, R Addou, S McDonnell, C L Hinkle, and R M Wallace. WSe2-contact metal interface chemistry and band alignment under high vacuum and ultra high vacuum deposition conditions. *2D Materials*, 4(2):025084, 2017. 35, 63, 78

[96] Hennrik Schmidt, Francesco Giustiniano, and Goki Eda. Electronic transport properties of transition metal dichalcogenide field-effect devices: surface and interface effects. *Chemical Society Reviews*, 44(21):7715–7736, 2015. 35

[97] Jiandong Yao and Guowei Yang. Flexible and High-Performance All-2D Photodetector for Wearable Devices. *Small*, 14(21):1704524, 2018. 35

[98] Jiandong Yao, Zhaoqiang Zheng, and Guowei Yang. Promoting the Performance of Layered-Material Photodetectors by Alloy Engineering. *ACS Applied Materials and Interfaces*, 8(20):12915–12924, 2016. 35

[99] Jiandong Yao, Zhaoqiang Zheng, and Guowei Yang. All-Layered 2D Optoelectronics: A High-Performance UVvisNIR Broadband SnSe Photodetector with Bi2Te3Topological Insulator Electrodes. *Advanced Functional Materials*, 27(33):1701823, 2017. 35

[100] Zhaoqiang Zheng, Jiandong Yao, and Guowei Yang. Centimeter-Scale Deposition of Mo0.5W0.5Se2Alloy Film for High-Performance Photodetectors on Versatile Substrates. *ACS Applied Materials and Interfaces*, 9(17):14920–14928, 2017. 35

[101] Peida Zhao, Daisuke Kiriya, Angelica Azcatl, Chenxi Zhang, Mahmut Tosun, Yi-Sheng Liu, Mark Hettick, Jeong Seuk Kang, Stephen McDonnell, Santosh KC, Jinghua Guo, Kyeongjae Cho, Robert M. Wallace, and Ali Javey. Air Stable p-Doping of WSe2 by Covalent Functionalization. *ACS Nano*, 8(10):10808–10814, 2014. 35, 89

[102] Woanseo Park, Juhun Park, Jingon Jang, Hyungwoo Lee, Hyunhak Jeong, Kyungjune Cho, Seunghun Hong, and Takhee Lee. Oxygen environmental and passivation effects on molybdenum disulfide field effect transistors. *Nanotechnology*, 2013. 35, 36, 89

[103] Jian Gao, Baichang Li, Jiawei Tan, Phil Chow, Toh Ming Lu, and Nikhil Koratkar. Aging of Transition Metal Dichalcogenide Monolayers. *ACS Nano*, 2016. 35

[104] Amritesh Rai, Amithraj Valsaraj, Hema C.P. Movva, Anupam Roy, Rudresh Ghosh, Sushant Sonde, Sangwoo Kang, Jiwon Chang, Tanuj Trivedi, Rik Dey, Samaresh Guchhait, Stefano Larentis, Leonard F. Register, Emanuel Tutuc, and Sanjay K.

Banerjee. Air Stable Doping and Intrinsic Mobility Enhancement in Monolayer Molybdenum Disulfide by Amorphous Titanium Suboxide Encapsulation. *Nano Letters*, 15(7):4329–4336, 2015. 35

[105] Lingming Yang, Kausik Majumdar, Han Liu, Yuchen Du, Heng Wu, Michael Hatzistergos, P. Y. Hung, Robert Tieckelmann, Wilman Tsai, Chris Hobbs, and Peide D. Ye. Chloride molecular doping technique on 2D materials: WS2and MoS2. *Nano Letters*, 14(11):6275–6280, 2014. 36

[106] Rajesh Kappera, Damien Voiry, Sibel Ebru Yalcin, Brittany Branch, Gautam Gupta, Aditya D. Mohite, and Manish Chhowalla. Phase-engineered low-resistance contacts for ultrathin MoS2transistors. *Nature Materials*, 13(12):1128–1134, 2014. 36

[107] Hao Qiu, Lijia Pan, Zongni Yao, Junjie Li, Yi Shi, and Xinran Wang. Electrical characterization of back-gated bi-layer MoS 2 field-effect transistors and the effect of ambient on their performances. *Applied Physics Letters*, 2012. 36, 43, 89

[108] Gwan-hyoung Lee, Xu Cui, Duck Kim, Ghidewon Arefe, Xian Zhang, Chul-ho Lee, Fan Ye, Kenji Wantanabe, Takashi Taniguchi, and James Hone. Highly Stable , Dual-Gated MoS2 Transistors Encapsulated by Hexagonal Boron Nitride with Gate-Controllable Contact, Resistane and Threshold Voltage. *ACS Nano*, 9(7):7019–7026, 2015. 36

[109] Joel I.Jan Wang, Yafang Yang, Yu An Chen, Kenji Watanabe, Takashi Taniguchi, Hugh O.H. Churchill, and Pablo Jarillo-Herrero. Electronic transport of encapsulated graphene and WSe2devices fabricated by pick-up of prepatterned hBN. *Nano Letters*, 15(3):1898–1903, 2015. 36

[110] Filippo Giannazzo, Gabriele Fisichella, Giuseppe Greco, Salvatore Di Franco, Ioannis Deretzis, Antonino La Magna, Corrado Bongiorno, Giuseppe Nicotra, Corrado Spinella, Michelangelo Scopelliti, Bruno Pignataro, Simonpietro Agnello, and Fabrizio Roccaforte. Ambipolar MoS2 Transistors by Nanoscale Tailoring of Schottky Barrier Using Oxygen Plasma Functionalization. *ACS Applied Materials & Interfaces*, 9(27):23164–23174, 2017. 36, 62, 63, 89

[111] Timothy N. Walter, Frances Kwok, Hamed Simchi, Haila M. Aldosari, and Suzanne E. Mohney. Oxidation and oxidative vapor-phase etching of few-layer MoS2. *Journal of Vacuum Science & Technology B, Nanotechnology and Microelectronics: Materials, Processing, Measurement, and Phenomena*, 35(2):021203, 2017. 36, 62, 89

[112] Si Young Lee, Un Jeong Kim, Jaegwan Chung, Honggi Nam, Hye Yun Jeong, Gang Hee Han, Hyun Kim, Hye Min Oh, Hyangsook Lee, Hyochul Kim, Young Geun Roh, Jineun Kim, Sung Woo Hwang, Yeonsang Park, and Young Hee Lee. Large Work Function Modulation of Monolayer MoS2 by Ambient Gases. *ACS Nano*, 10(6):6100–6107, 2016. 36, 89

[113] W. Jaegermann and D. Schmeisser. Reactivity of layer type transition metal chalcogenides towards oxidation. *Surface Science*, 165(1):143–160, 1986. 36, 89

[114] Dongwei Ma, Tingxian Li, Di Yuan, Chaozheng He, Zhiwen Lu, Zhansheng Lu, Zongxian Yang, and Yuanxu Wang. The role of the intrinsic Se and In vacancies in the interaction of O2 and H2O molecules with the InSe monolayer. *Applied Surface Science*, 434:215–227, 2018. 36, 89

[115] develompent of electronics and s.r.o. Custom software Kolibrik.net. Custom develompent of electronics and software, 2017. 37, 48, 64

[116] G. Kresse and J. Furthmüller. Efficiency of ab initio total energy calculations for metals and semiconductors using a plane wave basis set. *Comput. Mat. Sci.*, 6(1):15, 1996. 37, 91

[117] John P. Perdew, Kieron Burke, and Matthias Ernzerhof. Generalized gradient approximation made simple. *Physical Review Letters*, 77(18):3865–3868, 1996. 37, 91

[118] Michal Moraw. Analysis of outgassing characteristics of metals. *Vacuum*, 36(7-9):523–525, 1986. 43

[119] Yoshihiro Shimazu, Mitsuki Tashiro, Satoshi Sonobe, and Masaki Takahashi. Environmental Effects on Hysteresis of Transfer Characteristics in Molybdenum Disulfide Field-Effect Transistors. *Scientific Reports*, 6:30084, 2016. 43

[120] Sefaattin Tongay, Jian Zhou, Can Ataca, Jonathan Liu, Jeong Seuk Kang, Tyler S. Matthews, Long You, Jingbo Li, Jeffrey C. Grossman, and Junqiao Wu. Broad-range modulation of light emission in two-dimensional semiconductors by molecular physisorption gating. *Nano Letters*, 13(6):2831–2836, 2013. 43, 45

[121] S Mignuzzi, A J Pollard, N Bonini, B Brennan, I S Gilmore, M A Pimenta, D Richards, and D Roy. Effect of disorder on Raman scattering of single-layer MoS2. *Physical Review B*, 91(19):7, 2015. 43

[122] Hongsheng Liu, Nannan Han, and Jijun Zhao. Atomistic insight into the oxidation of monolayer transition metal dichalcogenides: from structures to electronic properties. *RSC Adv.*, 5(23):17572–17581, 2015. 45, 62

[123] Sefaattin Tongay, Jian Zhou, Can Ataca, Kelvin Lo, Tyler S. Matthews, Jingbo Li, Jeffrey C. Grossman, and Junqiao Wu. Thermally driven crossover from indirect toward direct bandgap in 2D Semiconductors: MoSe2 versus MoS2. *Nano Letters*, 12(11):5576–5580, 2012. 45

[124] Dongwei Ma, Benyuan Ma, Zhiwen Lu, Chaozheng He, Yanan Tang, Zhansheng Lu, and Zongxian Yang. Interaction between H ₂ O, N ₂ , CO, NO, NO ₂ and N ₂ O molecules and a defective WSe ₂ monolayer. *Phys. Chem. Chem. Phys.*, 19(38):26022–26033, 2017. 45

[125] César González, Blanca Biel, and Yannick J. Dappe. Adsorption of small inorganic molecules on a defective MoS ₂ monolayer. *Phys. Chem. Chem. Phys.*, 19(14):9485–9499, 2017. 45, 51

[126] Song-Lin Li, Emanuele Orgiu, Paolo Samorì, Kazuhito Tsukagoshi, and Paolo Samor. Chem Soc Rev Charge transport and mobility engineering in two-dimensional

transition metal chalcogenide semiconductors. *Chem. Soc. Rev.*, 45(45):1–226, 2016. 48, 63

[127] O. Lang, Y. Tomm, R. Schlaf, C. Pettenkofer, and W. Jaegermann. Single crystalline GaSe/WSe2 heterointerfaces grown by van der Waals epitaxy. II. Junction characterization. *Journal of Applied Physics*, 75(12):7814–7820, 1994. 48

[128] Yuanyue Liu, Pauls Stradins, and Su Huai Wei. Air passivation of chalcogen vacancies in two-dimensional semiconductors. *Angewandte Chemie - International Edition*, 55(3):965–968, 2016. 48

[129] A. Klein, P. Dolatzoglou, M. Lux-Steiner, and E. Bucher. Influence of material synthesis and doping on the transport properties of WSe2 single crystals grown by selenium transport. *Solar Energy Materials and Solar Cells*, 46:175–186, 1997. 48

[130] Rafik Addou, Christopher M Smyth, Ji-Young Noh, Yu-Chuan Lin, Yi Pan, Sarah M Eichfeld, Stefan Fölsch, Joshua A Robinson, Kyeongjae Cho, Randall M Feenstra, and Robert M Wallace. One dimensional metallic edges in atomically thin WSe2 induced by air exposure. *2D Materials*, 5(2):025017, 2018. 48

[131] Rafik Addou and Robert M. Wallace. Surface Analysis of WSe 2 Crystals: Spatial and Electronic Variability. *ACS Applied Materials & Interfaces*, 8(39):26400–26406, 2016. 48

[132] Xiaodong Li, Jeffrey T Mullen, Zhenghe Jin, Kostyantyn M Borysenko, M Buongiorno Nardelli, and Ki Wook Kim. Intrinsic electrical transport properties of monolayer silicene and MoS 2 from first principles. *Physical Review B*, 87(11):115418, 2013. 61, 62

[133] Hualing Zeng, Gui-Bin Liu, Junfeng Dai, Yajun Yan, Bairen Zhu, Ruicong He, Lu Xie, Shijie Xu, Xianhui Chen, Wang Yao, and Xiaodong Cui. Optical signature of symmetry variations and spin-valley coupling in atomically thin tungsten dichalcogenides. *Scientific reports*, 2013. 62

[134] Haiyan Nan, Zilu Wang, Wenhui Wang, Zheng Liang, Yan Lu, Qian Chen, Daowei He, Pingheng Tan, Feng Miao, Xinran Wang, and Others. Strong photoluminescence enhancement of MoS2 through defect engineering and oxygen bonding. *ACS nano*, 8(6):5738–5745, 2014. 62

[135] Guru P. Neupane, Krishna P. Dhakal, Hyun Kim, Jubok Lee, Min Su Kim, Ganghee Han, Young Hee Lee, and Jeongyong Kim. Formation of nanosized monolayer MoS2by oxygen-assisted thinning of multilayer MoS2. *Journal of Applied Physics*, 120(5), 2016. 62

[136] Saiful I. Khondaker and Muhammad R. Islam. Bandgap Engineering of MoS2 Flakes via Oxygen Plasma: A Layer Dependent Study. *Journal of Physical Chemistry C*, 120(25):13801–13806, 2016. 62

[137] Anna N. Hoffman, Michael G. Stanford, Cheng Zhang, Ilia N. Ivanov, Akinola D. Oyedele, Maria Gabriela Sales, Stephen J. McDonnell, Michael R. Koehler, David G. Mandrus, Liangbo Liang, Bobby G. Sumpter, Kai Xiao, and Philip D. Rack. Atmospheric and Long-term Aging Effects on the Electrical Properties of Variable Thickness WSe2 Transistors. *ACS Applied Materials & Interfaces*, page acsami.8b12545, 2018. 64, 65, 89

[138] Rui Zhang, Daniel Drysdale, Vasileios Koutsos, and Rebecca Cheung. Controlled Layer Thinning and p-Type Doping of WSe2 by Vapor XeF2. *Advanced Functional Materials*, 2017. 68, 72

[139] C. Tan, Y. Liu, H. Chou, J. S. Kim, D. Wu, D. Akinwande, and K. Lai. Laser-assisted oxidation of multi-layer tungsten diselenide nanosheets. *Applied Physics Letters*, 2016. 68

[140] Keren M Freedy, Peter M Litwin, and Stephen John McDonnell. (Invited) In-Vacuo Studies of Transition Metal Dichalcogenide Synthesis and Layered Material Integration. *ECS Transactions*, 2017. 72

[141] Zai Quan Xu, Yupeng Zhang, Ziyu Wang, Yuting Shen, Wenchao Huang, Xue Xia, Wenzhi Yu, Yunzhou Xue, Litao Sun, Changxi Zheng, Yuerui Lu, Lei Liao, and Qiaoliang Bao. Atomically thin lateral p-n junction photodetector with large effective detection area. *2D Materials*, 3(4), 2016. 86

[142] Michael G. Stanford, Pushpa Raj Pudasaini, Alex Belianinov, Nicholas Cross, Joo Hyon Noh, Michael R. Koehler, David G. Mandrus, Gerd Duscher, Adam J. Rondinone, Ilia N. Ivanov, T. Zac Ward, and Philip D. Rack. Focused helium-ion beam irradiation effects on electrical transport properties of few-layer WSe2: Enabling nanoscale direct write homo-junctions. *Scientific Reports*, 6, 2016. 88

[143] Michael G. Stanford, Brett B. Lewis, Joo Hyon Noh, Jason D. Fowlkes, Nicholas A. Roberts, Harald Plank, and Philip D. Rack. Purification of nanoscale electron-beam-induced platinum deposits via a pulsed laser-induced oxidation reaction. *ACS Applied Materials and Interfaces*, 6(23):21256–21263, 2014. 88

[144] Michael G. Stanford, Yu-Chuan Lin, Maria Gabriela Sales, Anna N. Hoffman, Christopher T. Nelson, Kai Xiao, Stephen McDonnell, and Philip D. Rack. Lithographically patterned metallic conduction in single-layer MoS2 via plasma processing. *npj 2D Materials and Applications*, 2019. 88

[145] Anna N Hoffman, Michael G Stanford, Maria Gabriela Sales, Cheng Zhang, Ilia N Ivanov, Stephen J McDonnell, David G Mandrus, and Philip D Rack. Tuning the electrical properties of wse2 via o2 plasma oxidation: towards lateral homojunctions. *2D Materials*, 6(4):045024, 2019. 88, 104

[146] Likai Li, Yijun Yu, Guo Jun Ye, Qingqin Ge, Xuedong Ou, Hua Wu, Donglai Feng, Xian Hui Chen, and Yuanbo Zhang. Black phosphorus field-effect transistors. *Nature Nanotechnology*, 9(5):372–377, 2014. 88, 89

[147] Akinola D. Oyedele, Shize Yang, Liangbo Liang, Alexander A. Puretzky, Kai Wang, Jingjie Zhang, Peng Yu, Pushpa R. Pudasaini, Avik W. Ghosh, Zheng Liu, Christopher M. Rouleau, Bobby G. Sumpter, Matthew F. Chisholm, Wu Zhou,

Philip D. Rack, David B. Geohegan, and Kai Xiao. PdSe2: Pentagonal Two-Dimensional Layers with High Air Stability for Electronics. *Journal of the American Chemical Society*, 139(40):14090–14097, 2017. 89, 91, 100

[148] Wai Leong Chow, Peng Yu, Fucai Liu, Jinhua Hong, Xingli Wang, Qingsheng Zeng, Chuang Han Hsu, Chao Zhu, Jiadong Zhou, Xiaowei Wang, Juan Xia, Jiaxu Yan, Yu Chen, Di Wu, Ting Yu, Zexiang Shen, Hsin Lin, Chuanhong Jin, Beng Kang Tay, and Zheng Liu. High Mobility 2D Palladium Diselenide Field-Effect Transistors with Tunable Ambipolar Characteristics. *Advanced Materials*, 2017. 89, 92

[149] Alexander A Puretzky, Akinola D Oyedele, Kai Xiao, Amanda V Haglund, Bobby G Sumpter, David Mandrus, David B Geohegan, and Liangbo Liang. Anomalous interlayer vibrations in strongly coupled layered pdse2. *2D Materials*, 5(3):035016, 2018. 89

[150] Dmitry Ovchinnikov, Adrien Allain, Ying Sheng Huang, Dumitru Dumcenco, and Andras Kis. Electrical transport properties of single-layer WS2. *ACS Nano*, 2014. 89

[151] Antonio Di Bartolomeo, Aniello Pelella, Xiaowei Liu, Feng Miao, Maurizio Passacantando, Filippo Giubileo, Alessandro Grillo, Laura Iemmo, Francesca Urban, and Shi-Jun Liang. Pressure-Tunable Ambipolar Conduction and Hysteresis in Thin Palladium Diselenide Field Effect Transistors. *Advances Functional Materials*, page 1902483, 2019. 90, 92

[152] M. Dion, H. Rydberg, E. Schröder, D. C. Langreth, and B. I. Lundqvist. Erratum: Van der Waals density functional for general geometries (Physical Review Letters (2004) 92 (246401)), 2005. 91

[153] Giang D. Nguyen, Liangbo Liang, Qiang Zou, Mingming Fu, Akinola D. Oyedele, Bobby G. Sumpter, Zheng Liu, Zheng Gai, Kai Xiao, and An Ping Li. 3D Imaging and Manipulation of Subsurface Selenium Vacancies in PdSe2. *Physical Review Letters*, 2018. 91

[154] Oleg Lupan, Vasile Postica, Mathias Hoppe, Niklas Wolff, Oleksandr Polonskyi, Thierry Pauporté, Bruno Viana, Odile Majérus, Lorenz Kienle, Franz Faupel, and Rainer Adelung. PdO/PdO2 functionalized ZnO:::Pd films for lower operating temperature H2 gas sensing. *Nanoscale*, 2018. 97, 104

[155] L. S. Kibis, A. I. Titkov, A. I. Stadnichenko, S. V. Koscheev, and A. I. Boronin. X-ray photoelectron spectroscopy study of Pd oxidation by RF discharge in oxygen. *Applied Surface Science*, 2009. 97, 104

[156] J.F. Moulder, W.F. Stickle, and P.E. Sobol. Handbook of X-ray Photoelectron Spectroscopy, 1992nd ed. 1992. 100

Vita

Anna Hoffman was born in Morristown, N.J. and spent later childhood in the metro Atlanta, GA area with her parents and two brothers.She received her undergraduate degree in Materials Science and Engineering in 2015 at The Georgia Institute of Technology in Atlanta. She completed her graduate reserach work in Dr. Philip D. Racks group at the University of Tennessee with most lab work performed at the Center for Nanophase Material Science at Oak Ridge National Lab in Oak Ridge, Tennessee. Her research interests include optoelectronic properties of 2D materials, nanofabrication, and thin film processing methods. She enjoyed volunteering in the City of Knoxville Special Events department as a break from graduate work.